

2002

# Three-dimensional micromachined on-chip inductors for high frequency applications

Nimit Chomnawang

*Louisiana State University and Agricultural and Mechanical College, [nimitch@ccs.sut.ac.th](mailto:nimitch@ccs.sut.ac.th)*

Follow this and additional works at: [https://digitalcommons.lsu.edu/gradschool\\_dissertations](https://digitalcommons.lsu.edu/gradschool_dissertations)



Part of the [Electrical and Computer Engineering Commons](#)

---

## Recommended Citation

Chomnawang, Nimit, "Three-dimensional micromachined on-chip inductors for high frequency applications" (2002). *LSU Doctoral Dissertations*. 2572.

[https://digitalcommons.lsu.edu/gradschool\\_dissertations/2572](https://digitalcommons.lsu.edu/gradschool_dissertations/2572)

This Dissertation is brought to you for free and open access by the Graduate School at LSU Digital Commons. It has been accepted for inclusion in LSU Doctoral Dissertations by an authorized graduate school editor of LSU Digital Commons. For more information, please contact [gradetd@lsu.edu](mailto:gradetd@lsu.edu).

# THREE-DIMENSIONAL MICROMACHINED ON-CHIP INDUCTORS FOR HIGH FREQUENCY APPLICATIONS

A Dissertation

Submitted to the Graduate Faculty of the  
Louisiana State University and  
Agricultural and Mechanical College  
in partial fulfillment of the  
requirements for the degree of  
Doctor of Philosophy

in

The Department of Electrical and Computer Engineering

by

Nimit Chomnawang

B.Eng., King Mongkut's Institute of Technology Ladkrabang, 1993

M.S., Virginia Commonwealth University, 1999

M.S.E.E., Louisiana State University, 2001

December 2002

To Amm....

You are the wind beneath my wings.

## ACKNOWLEDGMENTS

I would like to express my deepest gratitude and appreciation to my advisor Dr. Jeong-Bong Lee, without whose faith in MEMS, continued interest, dedication, and support, this work would not be possible. Additionally, he deserves my great respects for his patient and fairness as problems occurred occasionally in the work place.

Special thanks goes to Dr. Pratul K. Ajmera who is my acting major professor and the chairman of my advisory committee for his help throughout graduate program procedures and revision of this dissertation. I would like to thank Dr. Martin Feldman, Dr. Jagannathan Ramanujam, Dr. John M. Tyler for serving as my advisory committee and my graduate advisor Dr. Jorge Aravena for his help on graduate school regulations.

I would like to express my appreciation to Dr. W. Alan Davis of the University of Texas at Arlington for his advises on high frequency measurements. Permissions to use the Agilent 8510C network analyzer by the UTA Center for Electronic Materials, Devices and Systems are greatly appreciated.

I specially thank my colleagues, K. S. Kim, S. W. Park, A. Nallani, K. S. Colinjivadi and Hong Lu for their helps and discussions, which were essential to accomplish my study. A special thanks goes to Dr. B.G. Kim for his suggestions in curve fitting.

There are people whom I would like to express my special thanks including LSU staffs, Golden Hwaung, Rhett Smith, Angela Fleming, Sandra Haynes, James Breedlove and Tonya Rushing, and UTD staffs Keith Bradshaw, John Goodnight and Nancy Brumley for their generous help. Research facilities provided by the LSU department of Electrical and Computer Engineering, the LSU Center for Advanced Microstructures and Devices and the UTD clean room are appreciated.

I am in debt to my parents for their loves, good wills and sacrificing supports throughout my life. I would like to express my deepest appreciation for all things taught by my previous teachers, without whose efforts I would be lost forever in my life long journey.

Finally, I am grateful to the Government of Thailand, the Suranaree University of Technology, and the Office of Educational Affairs of the Royal Thai Embassy at Washington, D.C. for providing opportunities, financial supports and all kinds of help throughout my studies.

# TABLE OF CONTENTS

ACKNOWLEDGMENTS.....	iii
LIST OF TABLES.....	vii
LIST OF FIGURES.....	viii
ABSTRACT.....	xiii
CHAPTER	
1 INTRODUCTION.....	1
1.1 Motivation.....	2
1.2 Review of Previous Work.....	6
1.2.1 Integrated Active Inductors.....	7
1.2.2 Planar On-chip Passive Inductors.....	9
1.2.3 Three-dimensional On-chip Passive Inductors.....	11
1.3 Research Objectives.....	14
1.4 Outline.....	15
2 DEVELOPMENT OF MICROMACHINING PROCESSES FOR THE THREE-DIMENSIONAL ON-CHIP MICROINDUCTORS.....	16
2.1 Metallic Microstructures Electroplating Using Thick Photoresist Molding.....	16
2.2 Patterning and Deformation of Polymeric Mesa.....	20
2.3 Conformal Electrodeposition and Patterning of Photoresists.....	24
2.4 Removal of Sacrificial Polymeric Layers.....	33
3 HIGH FREQUENCY MEASUREMENT AND MODELING METHODS.....	38
3.1 High Frequency On-wafer Measurement Methods.....	38
3.2 Equivalent Circuit Modeling Methods of On-chip Inductors.....	45
4 ON-CHIP ARCH-LIKE SOLENOID INDUCTORS.....	57
4.1 Design.....	58
4.2 Fabrication.....	64
4.3 Measurements, Modeling Results and Discussions.....	71
4.4 Conclusions.....	92
5 ON-CHIP DOME-SHAPED SPIRAL INDUCTORS.....	94
5.1 Design.....	94
5.2 Fabrication.....	102
5.3 Measurements, Modeling Results and Discussions.....	108
5.4 Conclusions.....	116
6 CONCLUSIONS.....	121
6.1 Summary.....	121

6.2 Suggestions for Future Work.....	123
REFERENCES.....	126
APPENDIX	
A PROCESS SEQUENCES OF SUSPENDED ON-CHIP ARCH-LIKE SOLENOID INDUCTOR.....	131
B PROCESS SEQUENCES OF SUSPENDED ON-CHIP DOME-SHAPED SPIRAL INDUCTOR.....	134
C MODELING MATLAB SOURCE CODES.....	138
VITA.....	181

## LIST OF TABLES

Table 2.1: Compositions of nickel and copper electroplating bath solutions.....	19
Table 2.2: Process parameters for SJR5740 photoresist mesa deformation.....	25
Table 2.3: Summary of UV exposure dose and developing time for EAGLE2100.....	34
Table 4.1: Model parameters of 2-turn solenoid inductors simulated by Sonnet EM.....	63
Table 4.2: Parameters of 2-turn, 3-turn, and 5-turn arch-like solenoid inductors for the traditional $\pi$ -models.....	79
Table 4.3: Physical model parameters of arch-like suspended solenoid inductors obtained from a curve-fitting modeling method.....	80
Table 4.4: Parameters of 2-turn, 3-turn, and 5-turn arch-like solenoid inductors with simplified physical $\pi$ -models.....	89
Table 5.1: Model parameters of 2-turn flat spiral inductors simulated by Sonnet EM.....	98
Table 5.2: Parameters of a 3-turn dome-shaped spiral inductor with simplified physical $\pi$ -models.....	120



# LIST OF FIGURES

Figure 1.1: Network topologies of active inductor-simulating circuits by Hara et al. (a), R. Kaunisto <i>et al.</i> (b), and H. Hayashi <i>et al.</i> (c).....	8
Figure 2.1: SEM photomicrograph of a 4:1 aspect ratio SU-8 test structure used as an electroplating mold.....	19
Figure 2.2: SEM photomicrograph of non-uniform deformation at upper corners of rectangular photoresist mounds resulted from thermal reflow without exposure to acetone vapor.....	22
Figure 2.3: Acetone exposure apparatus for the photoresist mesa reflow.....	22
Figure 2.4: SEM photomicrograph of cross-sectional views of rectangular photoresist mesa: before (top) and after (bottom) thermal reflow.....	23
Figure 2.5: SEM photomicrograph of cylindrical photoresist mesa: before (top) and after (bottom) thermal reflow.....	23
Figure 2.6: Deformed photoresist mesas: low aspect ratio (top), and high aspect ratio (bottom).....	25
Figure 2.7: Burst in a photoresist mound in a RIE chamber due to insufficient drying.....	26
Figure 2.8: A non-planar silicon well test structure 700x700 $\mu\text{m}$ and 175 $\mu\text{m}$ deep.....	28
Figure 2.9: Plasma etch rates for PI2611 at various $\text{CF}_4$ concentrations in oxygen.....	29
Figure 2.10: A non-planar PI2611 polymer channels test structure 70 $\mu\text{m}$ deep.....	29
Figure 2.11: 70 $\mu\text{m}$ wide electroplated nickel lines patterned on a 175 $\mu\text{m}$ deep silicon well. The sacrificial PEPR2400 photoresist mold has been removed.....	30
Figure 2.12: 70 $\mu\text{m}$ wide electroplated nickel lines on a 25 $\mu\text{m}$ deep polyimide channels. The sacrificial PEPR2400 photoresist mold has been removed.....	31
Figure 2.13: Deposition time for Eagle2100 photoresist at various bias voltages.....	32
Figure 2.14: Plating current for Eagle2100 photoresist as a function of time.....	33
Figure 2.15: Thickness of Eagle2100 photoresist deposited at various bias voltages.....	34

Figure 2.16: SEM photomicrograph of an Eagle2100 photoresist mold deposited on a dome structure (top), and a copper spiral track electroplated into the photoresist mold (bottom).....	35
Figure 2.17: SEM photomicrograph of an electroplated copper track on a dome structure after removal of an Eagle2100 photoresist mold.....	36
Figure 2.18: SEM photomicrograph of electroplated copper transmission line structures after two layers of SU-8 mold of 30 $\mu\text{m}$ each were removed by reactive ion etching.....	36
Figure 3.1: Diagrams of two-port networks (a) for Y, Z and ABCD-parameters, and (b) for S-parameters.....	40
Figure 3.2: Device under test (DUT) and dummy probe pads (PAD) for de-embedding parasitic effects.....	41
Figure 3.3: Measurement setup consisting of an Agilent 8510C vector network analyzer, HP8340B synthesized sweeper, HP8515A S-parameter test setup and high frequency probes for on-wafer testing.....	42
Figure 3.4: Open-short-load-thru calibration procedures of the on-wafer probes (a) open, (b) short, (c) 50 $\Omega$ load (paralleled 100 $\Omega$ ), and (d) thru.....	43
Figure 3.5: Traditional model of a two-port on-chip inductor.....	46
Figure 3.6: Comparison of the measured A and D parameters of (a) an arch-like solenoid inductor, and (b) a dome-shaped spiral inductor.....	47
Figure 3.7: Physical model of a two-port on-chip inductor.....	50
Figure 3.8: Simplified physical model of a two-port on-chip inductor.....	54
Figure 3.9: Equivalent one-port model of the simplified two-port physical model of on-chip inductor used in Q-factor analysis.....	55
Figure 4.1: Three-dimensional on-chip air-core solenoid inductors. (a) Conventional three-dimensional inductor design. (b) Non-suspended arch-like solenoid inductor. (c) Suspended arch-like solenoid inductor.....	59
Figure 4.2: Suspended solenoid inductor used in Sonnet EM simulation.....	61
Figure 4.3: Sonnet EM simulated Q-factors of a 2-turn copper inductor with various air-gap heights.....	62

Figure 4.4: Sonnet EM simulated equivalent circuit models of 2-turn solenoid inductors with no air-gap and 30 $\mu\text{m}$ high air-gap at their peak-Q frequencies.....	63
Figure 4.5: A drawing of a suspended 2-turn air-core arch-like solenoid on-chip inductor.....	64
Figure 4.6: Fabrication sequence of a three-dimensional suspended air-core arch-like solenoid on-chip inductor.....	66
Figure 4.7: Photomicrographs of a 5-turn arch-like solenoid on-chip inductor under fabrication: (a) after copper spacer electroplating and bottom conductor photo resist mold development, (b) after bottom conductor electroplating and photo resist mesa development.....	67
Figure 4.8: Photomicrographs of a 5-turn arch-like solenoid on-chip inductor under fabrication: after deformation of photoresist mesa, (b) after development of top conductor EAGLE2100 mold.....	68
Figure 4.9: Photomicrographs of a 5-turn arch-like solenoid on-chip inductor under fabrication: (a) after copper electroplating of top conductors and (b) Eagle2100 mold removal.....	69
Figure 4.10: Photomicrographs of a 5-turn arch-like solenoid on-chip inductor under fabrication: (a) after removal of sacrificial SJR5740 core, (b) after removal of bottom conductor SU-8 mold.....	70
Figure 4.11: SEM photomicrographs of copper arch-like inductors suspended in air 30 $\mu\text{m}$ above the substrate: (a) 2-turn, (b) 2-turn , (c) 3-turn, and (d) close view of an inductor with over-electroplated top conductors.....	71
Figure 4.12: Measured S-parameters of a 2-turn arch-like solenoid inductor: (a) DUT, (b) PAD, and (c) parasitic de-embedded.....	73
Figure 4.13: Measured S-parameters of a 3-turn arch-like solenoid inductor: (a) DUT, (b) PAD, and (c) parasitic de-embedded.....	74
Figure 4.14: Measured S-parameters of a 5-turn arch-like solenoid inductor: (a) DUT, (b) PAD, and (c) parasitic de-embedded.....	75
Figure 4.15: Measured Q-factors of arch-like solenoid inductors and Q-factors obtained from the traditional $\pi$ -network models.....	77
Figure 4.16: Traditional $\pi$ -network model parameters of arch-like solenoid inductors: (a) $L_S$ and $R_S$ , and (b) $C_P$ and $R_P$ .....	78
Figure 4.17: Simple $\pi$ -models of 2-turn, 3-turn, and 5-turn arch-like solenoid inductors at their peak-Q frequencies.....	79

Figure 4.18: $S_{21}$ parameter of a 2-turn arch-like solenoid inductor obtained from measurements and from curve-fitting modeling.....	81
Figure 4.19: S-parameters of (a) 2-turn, (b) 3-turn, and (c) 5-turn arch-like suspended inductors obtained from measurements and from curve-fitting modeling.....	82
Figure 4.20: Q-factors of arch-like suspended solenoid inductors from measurements and from curve-fitting modeling.....	83
Figure 4.21: Physical $\pi$ -models of (a) 2-turn, (b) 3-turn, and (c) 5-turn arch-like inductors from curve-fitting.....	84
Figure 4.22: Simplified physical $\pi$ -model parameters of arch-like solenoid inductors: (a) $L_S$ and $R_S$ , and (b) $C_P$ and $R_P$ .....	86
Figure 4.23: Modeled Q-factors of a 2-turn arch-like solenoid inductor resulting from different guess values of the simplified physical $\pi$ -model parameter $C_S$ .....	87
Figure 4.24: Measured and simplified physical model Q-factor values of arch-like solenoid inductors.....	87
Figure 4.25: Substrate loss and self-resonance factors of arch-like solenoid inductors obtained from a simplified physical model.....	88
Figure 4.26: Simplified physical modeled Q-factors of arch-like solenoid inductors with and without taking the substrate loss and resonance factors into account.....	88
Figure 4.27: Q-factor comparison of a 2-turn arch-like solenoid inductor resulting from Sonnet simulation, from measurements, and from the simplified physical model.....	89
Figure 4.28: Simplified physical $\pi$ -models of 2-turn, 3-turn, and 5turn arch-like solenoid inductors at their peak-Q frequencies.....	90
Figure 5.1: Schematic diagram of a suspended dome-shape spiral inductor.....	95
Figure 5.2: Drawing of a suspended flat spiral inductor used in Sonnet simulations.....	97
Figure 5.3: Q-factors of 2-turns flat spiral inductors with various air-gap heights obtained from Sonnet simulation.....	98
Figure 5.4: Equivalent circuit models for a 2-turn flat spiral inductor with no air-gap and 30 $\mu\text{m}$ high air-gap at their peak-Q frequencies from Sonnet EM simulation.....	99
Figure 5.5: Drawing of a 3-turn spiral conductor.....	101

Figure 5.6: Photomask layout of a 3-turn dome-shaped suspended spiral inductor.....	102
Figure 5.7: Fabrication sequences for a suspended dome-shaped spiral inductor.....	105
Figure 5.8: Photomicrographs of a dome-shaped spiral inductor under fabrication: (a) a cylindrical photoresist mesa, (b) a photoresist dome converted from a photoresist mesa after reflow process.....	109
Figure 5.9: Photomicrographs of a dome-shape spiral inductor under fabrication: (a) electrodeposited spiral conductor on the photoresist dome and electroplated long via, (b) fabricated short via, long via, and air-bridge.....	110
Figure 5.10: SEM photomicrograph of a 3-turn dome-shaped spiral inductor.....	111
Figure 5.11: SEM photomicrographs of a 3-turn dome-shape spiral inductor: (a) Probe pad with a long via and an air-bridge, (b) Probe pad with a spiral conductor....	112
Figure 5.12: Measured S-parameters of a 3-turn dome-shape spiral inductor: (a) DUT, (b) PAD, and (c) parasitic de-embedded.....	114
Figure 5.13: Simplified physical $\pi$ -model parameters of a 3-turn dome-shape spiral inductor: (a) $L_S$ and $R_S$ , and (b) $C_P$ and $R_P$ .....	117
Figure 5.14: Q-factor values of a 3-turn dome-shaped spiral inductor resulting from three different guess values used in the simplified physical $\pi$ -model parameter $C_S$ .....	118
Figure 5.15: Measured and simplified physical model Q-factor values of a 3-turn dome-shaped spiral inductor.....	118
Figure 5.16: Substrate loss and self-resonance factors of a 3-turn spiral inductor obtained from a simplified physical model.....	119
Figure 5.17: Q-factor values of a 3-turn dome-shaped spiral inductor obtained from simplified physical model, with and without substrate loss and self-resonance factors.....	119
Figure 5.18: Simplified physical $\pi$ -model of a 3-turn inductor at peak-Q frequency.....	120
Figure 6.1: A schematic diagram of high aspect ratio suspended solenoid inductor.....	124
Figure 6.2: Simulation results of high aspect ratio suspended LIGA-like solenoid inductors with air core heights from 100 $\mu\text{m}$ to 400 $\mu\text{m}$ : (a) Q-factors and (b) inductances.....	125

## ABSTRACT

Demands for wireless communication are ever-escalating for consumer and military communication applications. The requirements of portability, more functionality and lower cost have been driving forces toward smaller, more sophisticated and flexible wireless devices with lower power consumption. To meet these requirements, monolithically integrated passive inductors with high Q-factors and high self-resonant frequencies are desirable. Q-factor and self-resonant frequency of an inductor are significantly degraded at high frequencies due to conductor ohmic loss, magnetically induced eddy current in the conductive substrate, and lower self-resonant frequency from capacitance between conductive substrate and conductors.

In this dissertation, novel three-dimensional arch-like solenoid and dome-shaped spiral inductors are designed, fabricated, and characterized. MEMS-based fabrication techniques such as copper electroplating through voids in thick SU-8 photoresist molds and EAGLE2100 conformal photoresist molds on sacrificial arch-like or dome-shape SJR5740 photoresist mounds are utilized. An air gap between the inductor and the silicon substrate is used to reduce the degradations of inductor performance. According to the Sonnet electromagnetic simulations, 30  $\mu\text{m}$  air-gap suspension over the substrate is an adequate choice for these inductors. Suspended arch-like solenoid copper inductor has flat bottom conductor connected to arch-like top conductor with an air core in between. This design has only 2 contact points per inductor turn to minimize series resistance. Suspended dome-shaped spiral copper inductor is fabricated on a sacrificial photoresist dome with the outer end connected to one probe pad, and the inner end connected to the other probe pad through vias and an air-bridge. The sidewalls of spiral turns in this design overlap less with each other thereby reducing inter-turn capacitances.

Fabricated inductors are characterized and modeled at high frequencies from S-parameter measurements. ABCD-parameters, derived from the S-parameters are translated into a simplified physical  $\pi$ -model. The resulting arch-like suspended inductors with 2-5 turns have inductances between 0.62 to 0.79 nH, peak Q-factor values between 15.42 to 17 at peak-Q frequencies between 4.7 GHz to 7.0 GHz, and self-resonant frequencies between 47.6 GHz to 88.6 GHz. The 3-turn dome-shaped spiral inductor has inductance of 3.37 nH, peak Q-factor of 35.9 at 1.65 GHz, and self-resonant frequency at 18.74 GHz.

# CHAPTER 1

## INTRODUCTION

Marked by his famous 1959 observation: There's Plenty of Room at The Bottom, Richard P. Feynman envisioned opportunities of manipulation and control of things on a small scale [1]. Based on scaling approach, a new field of scientific inquiry namely miniaturization of systems has evolved into a field of Microelectromechanical Systems (MEMS) in which electronics, mechanics, chemistry, biology and optics are miniaturized and integrated. Scaling approach has exceptionally well worked in Integrated Circuit (IC) technology in which the number of electronic devices integrated and miniaturized on a semiconductor chip has grown from less than 10 in the 1960's to over a billion in the 1990's.

This success motivated the extension of two-dimensional IC manufacturing techniques to three-dimensional domain in the MEMS field. MEMS technologies utilize several fabrication techniques including bulk micromachining, surface micro-machining, wafer bonding, LIGA (German acronym: RoentgenLithographie Galvanik Abformung, in other words X-ray lithography, electrodeposition, and molding) [2] and LIGA-like techniques using conventional ultraviolet (UV) lithography to realize three-dimensional structures and devices. MEMS technologies enable miniaturization of microstructures, devices and systems through batch fabrications and demonstrate many advantages of the state-of-the-art integrated circuit (IC) fabrication technology. Some of these advantages can be stated in terms of cost reduction through batch fabrication, significant size reduction through dimension downscaling, and more complex structures through sophisticated three-dimensional fabrication techniques. Utilizing materials and fabrication techniques compatible with conventional IC technologies, electrical,



mechanical or optical structures can be monolithically integrated with electronic circuitry providing complete systems with more functions and intelligence. These MEMS technologies have been used to enhance performance over their conventional counterparts in many devices such as pressure sensors [3], accelerometers [4], micro-optics [5], and radio frequency (RF) devices [6].

## **1.1 Motivation**

In communication applications, military and consumer demands for wireless communication products such as military communications, aviation, navigations, data links, global positioning systems (GPS) as well as other personal communications (cellular phones, pagers, wireless computing), are ever-escalating.

Increasing the operating frequencies of wireless communication devices is one of many solutions to expand the number of communication channels to meet increasing demands for higher capacity. Other solutions may utilize high-speed modulation techniques or improve efficiency of RF devices at higher frequencies. Developments of high efficiency wireless communication devices operating at higher frequencies are, hence, are essential.

Increasing high-capacity demands also impose higher requirements on electronics circuits and systems design for wireless communication devices. In today's society, there is a high possibility that multiple communication transmitters and receivers exist near each other. Sophisticated anti-jam and identification functions are required in these communication systems in utilizing multiple devices. These requirements have been a continuous driving force for technological movement toward smaller and more secure communication systems that have better portability, more functionality, lower cost and lower power consumption. Major hurdles that need to be crossed to meet these goals include circuit power dissipation, electromagnetic

compatibility and system complexity. In order to be attractive to the consumers, these wireless communication devices must satisfy both high-speed requirement and low system cost.

Operating simultaneous multiple transmitters and receivers at the same site requires highly frequency selective transmission, high dynamic range reception (ability of the receiver to handle weak and strong signals over a frequency range) and exceptional filtering at both transmitter and receiver ends to ensure non-interference with each other. Anti-jam operations require highly selective filters [6].

Currently, combinations of monolithic microwave circuits made of GaAs field effect transistors (FET), p-i-n (PIN) diodes and varactor diodes are used to achieve filtering, switching and tuning functions. Unfortunately, these configurations have many disadvantages such as high power consumption, low reliability and high manufacturing cost (use of GaAs technology). RF performance of these monolithic microwave integrated circuits (MMICs) is low as additional gain enhancement circuits are needed to be integrated into the system which increases power consumption.

High-frequency wireless communication devices are also fabricated by a hybrid combination of GaAs MMIC on-chip circuitry with off-chip passive components such as ceramic and surface acoustic wave (SAW) filters, to achieve low power consumption and high performance. Unfortunately, this configuration is facing more challenging problems in packaging, system size reduction and manufacturing costs due to complex functional requirements.

Due to advances of high-speed complementary metal-oxide-semiconductor (CMOS) IC technology, many researchers are investigating the migration from the expensive GaAs MMIC technology to the cheaper silicon IC technology. According to the 2001 International Technology

Roadmap for Semiconductors issued by the Semiconductor Industry Association (SIA), the 0.13  $\mu\text{m}$  CMOS IC technology can provide speed that is high enough to handle current wireless communications devices (unity gain cut-off frequency ( $f_T$ ) and maximum oscillation frequency ( $f_{\text{max}}$ ) above 40 GHz). Higher  $f_T$  and  $f_{\text{max}}$  up to the range above 100 GHz are expected from the CMOS generation of the year 2012. CMOS microprocessors operating at 28.751 GHz are expected by 2016 [7]. To this end, integration of wireless circuits and components on a silicon chip is promising as it has sufficient circuit speed from CMOS transistors and low system fabrication cost associated with CMOS fabrication process.

Several wireless circuit building blocks such as mixers and low-noise amplifiers have been integrated monolithically on a single CMOS chip while others have yet not been monolithically integrated due to their poor post-integration performance. Frequency selective circuits such as frequency synthesizers and high quality filters are among the most difficult modules to integrate. The toughest problem in integration of these modules on a CMOS chip is the phase noise [8]. Noise at high frequencies can be represented by a noise-vector made of two orthogonal vectors of amplitude noise and phase noise. The amplitude noise vector points in the same direction as the signal vector and represents the familiar noise in signal amplitude. The phase noise vector points in the direction of angle rotation and represents noise in signal phase.

In order to ensure a large number of communication channels, very narrow channel spacing has been used in consumer telecommunication networks such as the Global System for Mobile communications (GSM). In this standard, the generated signal must be near pure sinusoidal, with extremely low single side-band phase noise level at or below  $-100$  dBc/Hz at frequency of 10 kHz away from the carrier [9]. In order to meet this requirement, building low

power-consumption and low phase-noise integrated oscillator is extremely desirable. This can be achieved by selective response frequency of an LC-tank circuit [10].

In order to build low-power frequency-selective circuits such as filters and LC-tank oscillators, high quality passive inductors are needed. The quality of inductor performance could be evaluated in terms of quality factor (Q-factor) and self-resonant frequency. Q-factor indicates energy losses in the inductor and is defined as the ratio of the electrical energy stored in the inductor to the energy dissipated per cycle, the ratio of real to imaginary parts of the complex impedance. The ratio of reactance to equivalent series resistance of the inductor demonstrates how well the energy can be stored in reactive part and how easily energy can be dissipated in the resistive part. An ideal passive inductor has zero equivalent series resistance rendering infinite Q-factor. Self-resonant frequency is the frequency at which high frequency behavior of the inductor turns from inductive to capacitive. This frequency is the indicator of the upper frequency limit at which the inductor can be used. In practice, self-resonant frequency should be much higher than the operating frequency of the inductor.

Since current CMOS IC technologies do not offer high-performance RF elements necessary for high frequency circuits, introduction of monolithically integrated RF MEMS technology to enhance RF functions of high-speed IC chips has enormous potential to improve performance of wireless communication systems. Applications of MEMS technologies for both passive and active RF devices have been vigorously investigated. These devices include MEMS switches [11], mechanical resonators and filters [12], frequency synthesizers using MEMS-based passive elements such as tunable capacitors and high quality-factor (high-Q) inductors [13, 14].

For many cases, a single MEMS element can be used as an entire solid-state circuit with better performance. In contrast, discrete passive components suffer largely from high frequency

losses due to parasitic capacitances of the bond pads, bond wires, packaging leads and the circuit board traces. These losses make off-chip circuit configurations less desirable at high frequencies, and generated the demand for monolithic integration solutions. Because of several advantages, monolithic integration of MEMS-based high frequency passive components with high-speed CMOS chip is very desirable.

In applying MEMS technologies to wireless communication systems, an important issue arises as to how these MEMS-based components are integrated onto a semiconductor chip with performance at high frequencies comparable to that of off-chip counterparts. It has been known that electrical performances of integrated passive elements degrade considerably due to parasitic effects such as stray capacitance and substrate losses [15-18].

Due to these problems, achieving better performance of passive on-chip components at high frequencies is technically challenging. This study will focus on fabrication and high frequency characterization of high quality on-chip solenoid and spiral RF inductors fabricated with MEMS approach using CMOS compatible post-IC micromachining technologies.

## **1.2 Review of Previous Work**

A survey of previous efforts in developments and implementations of integrated inductors in both planar IC and MEMS approaches is carried out. Organized by electrical and physical characteristics, integrated micro-inductors can be divided into three major categories: integrated active inductors; planar on-chip passive inductors; and three-dimensional on-chip passive inductors. The planar IC approach includes integrated active inductors and VLSI-based passive spiral inductors. The active inductors result from transistors operating under certain circuit configurations. The VLSI-based passive spiral inductors are simply metal tracks built from metal interconnects such as aluminum or copper. The three-dimensional approach includes solenoid

inductors with and without cores, and micromachined spiral inductors. The following subsections review these inductors in detail.

### 1.2.1 Integrated Active Inductors

Simulated inductance using microwave active elements was investigated as early as late 1960s [8]. The idea started from using a single transistor and feedback techniques to generate an inductive output. High frequency active inductors have been implemented with advanced high-speed active elements such as metal semiconductor field effect transistors (MESFET), heterojunction bipolar transistors (HBT), and high electron mobility transistors (HEMT), high frequency active inductors had been implemented.

Hera *et al.* proposed active inductor circuit with MESFET topology [19] as shown in Figure 1.1 (a). This active inductor utilizes two GaAs-based MESFETs and a feedback resistor. The dimension of the inductor circuit is only  $0.15 \mu\text{m}^2$  and is independent of the inductance value, which is determined by the value of the feedback resistor. The two-port floating active inductors of 3-7 nH and equivalent series resistance of 20-30 Ohms were fabricated on a GaAs substrate as a part of miniaturized wide-band amplifiers using MESFETs that have a typical cut-off frequency of 21 GHz. The fabricated two-port active inductors exhibit inductive behavior up to 5 GHz only at one of two ports due to severe asymmetry between the two ports. Therefore active inductors of this type must be used as one-port devices by connecting the non-inductive port to ground. Hara *et al.* did not report characterization of Q-factors of these inductors.

Kaunisto *et al.* proposed active inductors resulting from circuit topology as shown in Figure 1.1 (b) based on GaAs and bipolar technologies [22]. The best simulations resulted in maximum Q-factors of one-port active inductors near 500 at frequency near 2 GHz and inductance values in the range of 2-3 nH.

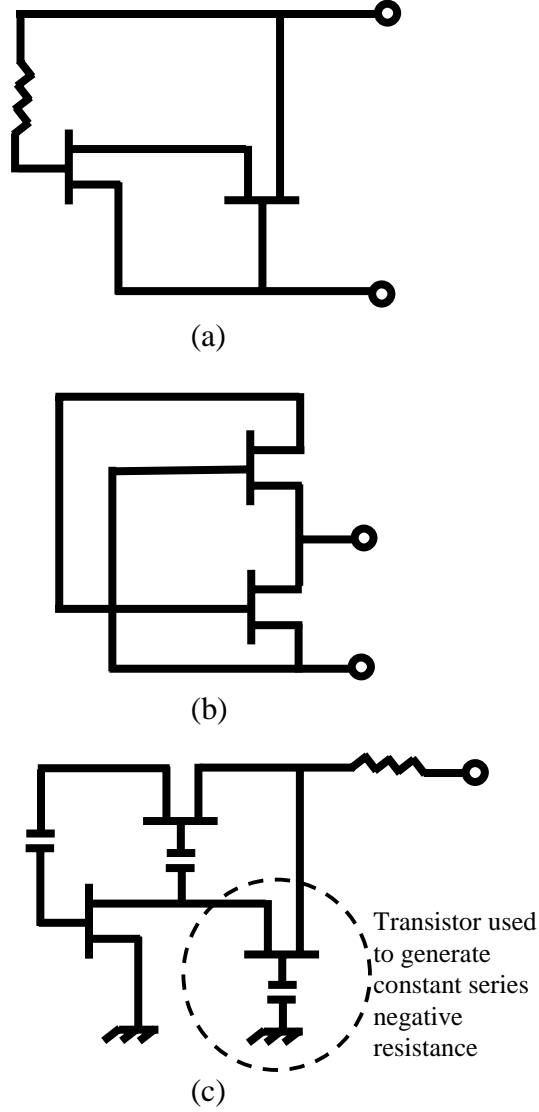


**Figure 1.1: Network topologies of active inductor-simulating circuits by Hara *et al.* (a), R. Kaunisto *et al.* (b), and H. Hayashi *et al.* (c).**

The use of bipolar active elements was suggested to reduce operating current and power consumption compared to MESFET active inductors. The active inductors proposed by Hayashi *et al.* [23] with network topology as shown in Figure 1.1 (c) were constructed from three InAlAs/InGaAs/InP high electron mobility transistors of  $f_T$  and  $f_{max}$  values of 140 and 180 GHz, respectively. These active inductors use frequency insensitive negative resistance provided by

one of three HEMTs to compensate for the internal losses in the transistors and their DC bias circuits. The Q-factors of these one-port HEMT active inductors are at least 100 at frequencies between 6 to 20 GHz, and are greater than 1000 at frequencies between 7 to 15 GHz. Power consumption of these active inductors is at least 54 mW.

Although active inductors yield very high Q-factor, they suffer from problems that finally degrade their high frequency performances. The biggest problem associated integrated active inductors is contribution of noise to other circuits on the same chip. It has been shown that an active inductor affects poorly on the phase noise level of an LC-tuned oscillator, both in terms of equivalent current and voltage noise [9].

Another disadvantage of active inductors is the severe asymmetry if they are arranged in floating two-port configuration. This allows only one-port operation in which the less inductive port is grounded. In addition, active inductors have a high value of power consumption. Therefore, they are not suitable for portable wireless communication transceiver applications.

### **1.2.2 Planar On-chip Passive Inductors**

Due to several disadvantages of active inductor described in subsection 1.2.1, integration of passive inductors onto the wireless circuitry chip is necessary in order to achieve reasonably high-Q inductors with low power consumption and low noise. Planar spiral has been earliest configuration of integrated passive inductors studied and implemented. Being fabricated from traces of metal, spiral inductors have been widely used in GaAs MMICs. Similarly, they have been extensively used as printed inductors on printed circuit boards (PCB) for RF consumer applications [24]. The popular spiral geometries include square, hexagonal, octagonal or circular shapes. The most popular shape has been the square spiral due to the ease of layout drawing by all layout software tools as well as e-beam patterning tools.



Due to lower cost of silicon high-speed integrated circuits, there have been endeavors to migrate planar spiral inductors from more expensive GaAs to silicon ICs. Nguyen *et al.* [25] fabricated planar spiral inductors onto standard silicon IC chip along with conventional integrated capacitors to build LC passive filters. The nine- and four- turns aluminum inductors occupying 230 and 150 square microns have inductance of 9.7 nH and 1.9 nH with peak Q-factors of 3 at 0.9 GHz and 8 at 4.1 GHz, respectively. Their self-resonant frequencies were 2.47 GHz for the 9-turn inductor and 9.7 GHz for the 4-turn inductors.

Since copper has low resistivity, Burghartz *et al.* used Cu-damascene technology, utilized in modern interconnect technology as the conductor material for spiral inductors [26]. Furthermore, three groups of inductors were fabricated on 10  $\Omega$ -cm silicon, high resistivity silicon, and sapphire substrates separately. It was found that Q-factors of spiral inductors fabricated on lower resistivity substrates such as 10  $\Omega$ -cm silicon, were lower than those fabricated on higher resistivity silicon substrates and sapphire. The value of Q-factor of a 1.4 nH inductor fabricated on sapphire substrate was approximately 40 at 5.8 GHz.

Based on the same principle, Choong-Mo *et al.* fabricated planar spiral inductors made of gold on a high resistivity substrate of thick oxidized porous silicon in order to increase resistivity of the substrate underlying the inductors [27]. In this work, a 6.29 nH 4.5–turns inductor with peak Q-factor of 13.3 at 4.6 GHz and self-resonant frequency of 13.8 GHz was achieved.

Another way of Q-factor improvements is to reduce the series resistance of the spiral conductors, which can be done by increasing the thickness of spiral conductors. Burghartz *et al.* utilized structural design of a 5-level metal interconnect option provided by VLSI design technology [28]. In order to increase the thickness of conductors, three layer spiral traces were designed and fabricated on top of each other. These layers of spiral traces were combined

together by several vias throughout the conductor area, resulting in a composite conductor with high conductance. The inductors were fabricated on top of a silicon chip containing bipolar complementary metal oxide semiconductor (BiCMOS) circuitry. The inductors of 1.45-5.1 nH with peak Q-factor ranging from 8-24 were obtained.

Besides utilizing the above mentioned planar IC technologies for improved Q-factor values, several efforts are being made to fabricate structures using MEMS-based technologies. Next subsection discusses applications of these technologies to three-dimensional on-chip inductors, both of spiral and solenoid variety.

### **1.2.3 Three-dimensional On-chip Passive Inductors**

In this subsection, improvements of spiral inductors and implementations of solenoid three-dimensional inductors using micromachining techniques are discussed. Two widely used micromachining approaches include partial removal of lossy substrate material from underneath the inductor and raising of the inductor from the substrate surface.

In the former approach, Chang *et al.* fabricated a spiral inductor on a silicon substrate containing a 2- $\mu\text{m}$  linewidth CMOS RF amplifier [29]. Aiming to reduce the substrate parasitic effects, a partial portion of substrate bulk material is anisotropically removed by silicon wet etching to create a 200-500  $\mu\text{m}$  deep air-gap underneath the spiral inductor. Two identical suspended spiral inductors of 100 nH each were used as the load of a balanced amplifier that was tuned to a 800 MHz center frequency. The CMOS amplifier demonstrated considerably high gain of 14 dB at 770 MHz after partial substrate removal with power consumption of only 7 mW. With improvements of substrate etching processes, Rofougaran *et al.* integrated a better version of suspended spiral inductors with a 1  $\mu\text{m}$  linewidth CMOS low-noise amplifier and a down-conversion mixer circuit operating at 1 GHz [30].

Ribas *et al.* applied partial substrate removal to a planar spiral inductor on GaAs HEMT MMIC [31]. Although GaAs substrates are already semi-insulating, this effort was aimed to reduce the parasitic capacitances of the spiral traces and the backside ground plane. Bulk GaAs substrate was selectively removed by a maskless wet etching process in a citric acid solution. Measurement results showed that the coupling capacitance between the metal traces and the GaAs substrate were considerably reduced but the fringing capacitance between spiral metal turns was not lower. The inductor has a Q-factor of 16 and self-resonant frequency up to 16 GHz. It was suggested that removal of bulk substrate changes relative permittivity of GaAs underneath the inductor from 12.9 to that of air or unity resulting in exponential decrease of the effective permittivity. By removing the substrate material underneath the inductor, the coupling capacitors between spiral traces, and the substrate should decrease by half.

Another approach to reduce substrate parasitic effects is to raise the inductor body so that it is suspended in air above the substrate by inserting metallic spacers. Yoon *et al.* fabricated one-port suspended spiral inductor using electroplated nickel as a metallic sacrificial mold and copper as a structural material [32]. Two copper posts, one at the core center, another at the output port, were fabricated before the spiral tracks. When the metallic sacrificial nickel mold was selectively etched away, the copper posts become the support of the suspended inductors. From the experimental results, it was speculated that if the spiral traces were raised up at least 30  $\mu\text{m}$  from the standard silicon substrate, the substrate parasitic effects could be eliminated almost completely. The fabricated suspended inductor of 1.8 nH had a Q-factor of 50 at 7 GHz.

Since a planar spiral inductor has a large area of metal traces in close proximity to the substrate, eddy current losses become a dominant factor limiting its Q-factor value. In contrast, the geometry of a three-dimensional on-chip solenoid inductor minimizes coil area that is close

to the substrate. This suggests that solenoid inductors should achieve maximized Q-factor and self-resonant frequency values.

Young *et al.* implemented copper solenoid inductors with conductors wrapping around an alumina core 500  $\mu\text{m}$  wide and 650  $\mu\text{m}$  high [13]. The 5  $\mu\text{m}$  thick bottom conductors were formed by copper electroplating and the alumina core was glued onto the bottom conductors. The vertical sidewall conductors were formed by electrodepositing conformal photoresist along the core profile. A maskless direct-write laser lithography tool was used to draw top conductor traces on the alumina core and copper was electroplated into the patterned traces. The fabricated one-turn inductor of 4.8 nH had Q-factor of 30 at 1 GHz which is comparable to values obtained for off-chip discrete multi-layer chip inductors [33].

Kim *et al.* further improved the solenoid inductors by replacing alumina core with air core [34]. Using surface micromachining techniques, the solenoid bottom conductors are separated from the substrate by two 20  $\mu\text{m}$  high copper posts electroplated via utilizing a polyimide sacrificial layer. Multiple steps of polyimide patterning and copper electroplating were used to realize via conductors and the sacrificial polyimide core as well as the top conductors. Suspended free-standing copper air core inductor that was obtained after all sacrificial layers were removed had inductance varying from 1 to 20 nH with peak Q-factor from 7 to 60.

Yoon *et al.* also utilized surface micromachining techniques to fabricate non-suspended solenoid inductors on silicon substrate of 10  $\Omega\text{-cm}$  resistivity [35]. Copper bottom conductors were electroplated through the first photoresist molds. For vias and top conductors, a two-step UV exposure was done to define the via-holes first, followed by a shallow exposure to define the top conductors. The molds for both vias and top conductors were developed and filled with

copper by electroplating. Inductors of 2.67 nH were obtained with peak Q-factor value of 16.7 and the self-resonant frequency of 2.4 GHz.

Taking advantage of a programmable wire-bonding machine, Lee *et al.* used gold bond-wires to construct top conductors of an arch-like solenoid inductors [36]. Inductors of this type were fabricated on GaAs MMIC substrates. The bottom conductors of the solenoid inductors were parallel metal strips, patterned on a 2  $\mu\text{m}$  thick gold layer. A wire-bonding machine was then programmed to connect contact points of each turn together forming vertical bond-wire loop with arch-like profile.

These arch-like bond-wire solenoid inductors between 2.2 - 6 nH exhibited high peak Q-factor values ranging from 38 to 63 for 2 to 4-turn inductors, with self-resonant frequency of 17 and 9.4 GHz, respectively. Although arch-like bond-wire solenoid inductors yield high Q-factors, several disadvantages have been found. First, the bonding machine must connect the top conductors together one at a time. Therefore, it loses advantages of parallel batch fabrication inherent in IC technologies. Second, the bond-wire top conductors are not mechanically reliable and they are subject to position displacements resulting in changes in inductor characteristics.

### **1.3 Research Objectives**

The objective of this research is to develop core technologies essential to the realization of three-dimensional on-chip solenoid and spiral inductors using MEMS approach. Core technologies for realization of these MEMS-based on-chip inductors include the development of micromachining processes for three-dimensional suspended inductors, on-wafer high frequency measurement method and on-chip inductor modeling. Once these core technologies are developed, examples of suspended arch-like solenoid inductors and dome-shaped spiral inductors will be designed, fabricated and modeled to demonstrate usefulness of these core technologies.

To achieve the objectives of this research, the following steps are taken: (1) develop micromachining processes that are essential for the realization of MEMS-based three-dimensional on-chip solenoid and spiral inductors such as fabrication of metallic microstructures using electroplating in thick photoresist molds, fabrication of deformed sacrificial polymeric mesa structures, conformal deposition and patterning of photoresists and the removal of polymeric sacrificial materials; (2) develop high frequency on-wafer measurement method; (3) develop inductor modeling; (4) design and fabricate the suspended three-dimensional on-chip arch-like solenoid inductors and dome-shaped spiral inductors using the above developed micromachining processes; (5) perform high frequency measurements and modeling on both types of on-chip inductors using the developed measurement and modeling methods.

## **1.4 Outline**

Chapter 2 of this dissertation will discuss the development of basic micromachining processes for suspended three-dimensional on-chip arch-like solenoid and dome-shaped spiral inductors. It includes electroplating of nickel and copper microstructures through thick photoresist molds, formation of arch-like and dome-shape polymeric mounds as sacrificial support materials for suspended inductors, conformal electrodepositions of photoresists and their patterning and the removal of sacrificial photoresists by plasma etching. Chapter 3 will discuss on-wafer measurement methods, parasitic components de-embedding and modeling methods of on-chip inductors. Design and fabrication of suspended arch-like solenoid inductors, their high frequency measurement and modeling results will be discussed in chapter 4. In chapter 5, design, fabrication, high frequency measurement and modeling of suspended dome-shaped inductors will be discussed. Finally, the summary and conclusions of this dissertation will be presented in chapter 6.

## **CHAPTER 2**

### **DEVELOPMENT OF MICROMACHINING PROCESSES FOR THE THREE-DIMENSIONAL ON-CHIP MICROINDUCTORS**

In order to realize three-dimensional on-chip microinductors, specialized micromachining fabrication processes must be developed. Development of such micromachining processes for the realization of three-dimensional on-chip micro inductors is discussed in this chapter. The first section describes electroplating of metallic microstructures using thick photoresist molds. This process will be used in many fabrication steps in this research. Section 2.1 describes the formation of photoresist mesa structures and deformation of such photoresist mesa. This process will be used to fabricate hemi-cylindrical and hemi-spherical three-dimensional polymeric sacrificial layers for the realization of arch-like solenoid inductors (chapter 4) and dome-shaped spiral inductors (chapter 5). Section 2.2 describes the electrodeposition of photoresist onto non-planar surfaces and formation of metallic traces on non-planar surfaces using subsequent electrodeposition of metals. This process will be used to fabricate conformal metallic traces on non-planar three-dimensional polymeric layers.

#### **2.1 Metallic Microstructure Electroplating Using Thick Photoresist Molding**

There has been significant interest for the realization of relatively thick and high aspect ratio microstructures in MEMS using thick photoresists. Several thick photoresists such as AZ 4562 (Clariant), ma-P 100 (Micro Resist Technology) and the negative tone SU-8 (Microchem) have been extensively used in MEMS devices fabrications [37-39]. Particularly, SU-8 has been widely investigated since it can be used to create very thick structures, typically in a range of 10 - 500  $\mu\text{m}$ , with nearly vertical sidewall profile using standard UV lithography. In this work,

metallic microstructures were fabricated by electroplating through relatively thick SU-8 sacrificial polymeric molds.

It has been found that, SU-8 thick film adheres to a bare silicon substrate better than the substrates coated with metallic thin film. However, formation of metallic microstructures by electroplating requires a thin film conductive plating base as a seed layer for the plating metal. The most commonly used plating base metallic thin film is copper. Since the surface of copper can be easily oxidized in open air, it has been found that this oxidized copper layer weakens adhesion strength of the polymeric (e.g., SU-8) thick film to the copper plating-base. This problem was addressed by removing the native copper oxide in 5%  $\text{H}_2\text{SO}_4$  (sulfuric acid) solution and baking at 95 °C, prior to spin-on coating of SU-8.

Since SU-8 is typically used in the formation of relatively thick microstructures, residual stress in the SU-8 film can be very high. Residual stress within SU-8 thick film can cause cracks, adhesion loss or breakage of the thick film. In order to avoid destructive residual stress in SU-8 thick films, thermal processes must be designed to minimize thermal shock in handling of SU-8 films. In this work, a two-step baking process is used. Here, the film is first soft baked at 65°C and consequently baked at 95°C to prevent sudden changes in the temperature. Cooling down the wafer after the baking at 95°C has been done in two ways: slow cooling in a turned-off baking oven; or natural cooling on a thermal insulator outside the oven. In the former method, the oven can be turned off, after the wafer has been in the oven for a certain predetermined time. This method requires baking time adjustment to take into account additional baking time during the slow cooling down stage after the oven had been turned off. Another method is taking the wafer out of the oven right after baking and placing it on a thermal insulator in open air. In this work,



the wafer taken out from the oven and placed on a cloth, which is suspended on the top of a petri dish. In this way, the wafer is suspended in the air above the petri dish and naturally cooled.

Since the soft-baked SU-8 film is sensitive to near UV light with 350-400 nm wavelength, the film patterning was done by standard UV photolithography. Different UV exposure doses for different thicknesses of SU-8 film were used. After the UV exposure, SU-8 film was post-exposure baked in an oven at 65 °C and 95 °C in order to allow the UV exposed polymer chains to perform cross-linking and better delineate the exposed and unexposed areas. Development of the post-exposure baked SU-8 film was done in the NANO SU-8 developer (Microchem) and briefly rinsed in isopropanol and de-ionized (DI) water. Figure 2.1 shows a scanning electron microscope (SEM) photomicrograph of a SU-8 mold test structure 80  $\mu\text{m}$  thick with 20  $\mu\text{m}$  wide fingers and spacings.

Electroplating can be carried out through this mold to create a metallic microstructure. A copper-containing plating base of a composite metal sandwich of Cr/Cu/Cr or Ti/Cu/Ti thin films with copper thickness of 25 nm to 100 nm and chrome or titanium thickness of 5 nm to 10 nm can be used to supply electroplating current as well as to serve as an adhesive intermediate layer for the top and the bottom surfaces. The topmost Ti or Cr thin film also works as a protecting layer of copper plating base from oxidation by the ambient air. The compositions of electroplating bath solutions for nickel and copper depositions are summarized in Table 2.1.

Prior to electroplating, the topmost Cr or Ti protecting layer in the area not covered by SU-8 was removed by a wet etchant. Then, the sample is placed in an electroplating bath approximately 10 cm apart from a sheet of the metal source.

A constant current is applied from a power supply with the anode connected to the metal source and the cathode connected to the sample. Electroplating current is monitored with a digital

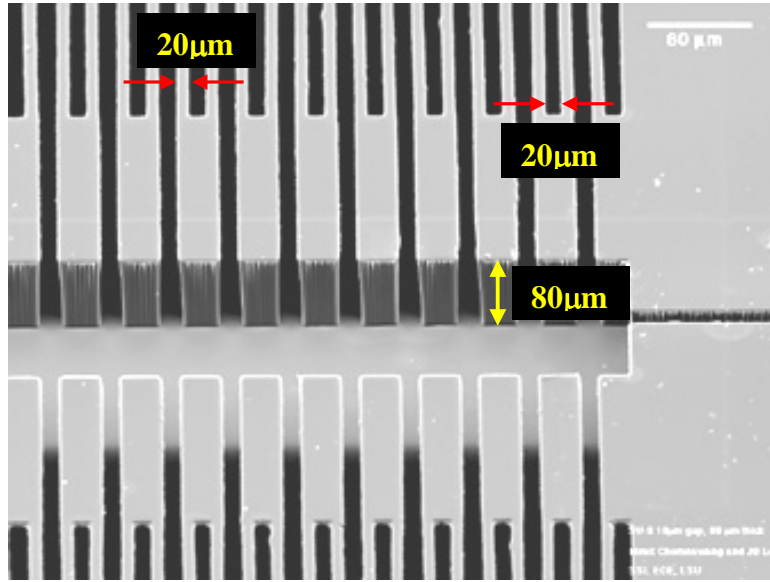


**Figure 2.1: SEM photomicrograph of a 4:1 aspect ratio SU-8 test structure used as an electroplating mold.**

**Table 2.1: Compositions of nickel and copper electroplating bath solutions.**

Ni electroplating Bath	Nickel sulfate ( $\text{NiSO}_4 \cdot 6\text{H}_2\text{O}$ )	360 g
	Nickelous chloride ( $\text{NiCl}_2 \cdot 6\text{H}_2\text{O}$ )	9 g
	Boric acid ( $\text{H}_3\text{BO}_3$ )	45 g
	DI water	1800 ml
Cu electroplating Bath	Cupric sulfate ( $\text{CuSO}_4 \cdot 5\text{H}_2\text{O}$ )	450 g
	Sulfuric acid ( $\text{H}_2\text{SO}_4$ )	90 ml
	DI water	1800 ml
Copper plating base cleaner	5 % sulfuric acid ( $\text{H}_2\text{SO}_4$ )	
Cr etchant for protecting layer	50 % hydrochloric acid (HCl), sample excited by Al bar (magic touch)	
	Sodium hydroxide (NaOH)	20 g
	Potassium hexa-cyanoferate ( $\text{K}_3\text{Fe}(\text{CN})_6$ )	20 g
	DI water	100 g
Ti etchant for protecting layer	5 % hydrofluoric acid (HF)	

multi-meter and is kept constant at a current density of approximately  $10 \text{ mA/cm}^2$ . The current density can be changed to adjust electroplating rate and electroplating time. Electroplating with a lower current density yields smoother metal structures but requires longer plating time.

In this work, SU-8 molds will be used to form copper spacer posts that raise the inductor's body away from the substrate. Fabrication procedures of the copper spacer posts will be discussed in detail in chapters 4 and 5.

## **2.2 Patterning and Deformation of Polymeric Mesa**

In previous section, the use of SU-8 electroplating molds for the formation of copper spacer posts was discussed. This section discusses formations of polymeric mesas that will be used as sacrificial support structures for dome-shaped spiral inductors and as sacrificial cores for arch-like solenoid inductors.

The method of creating a smooth profile hemi-spherical polymeric mound has been used in applications such as microlenses for microscopy [40] and fiber optics devices [41] and for microfluidic applications [42]. In this work the same method is utilized in the fabrication of three-dimensional inductors.

Depending on final thickness desired, single or multiple layers of SJR5740 photoresist (Shipley) were spin-on coated with different spinning speeds on 3-inch diameter silicon wafers. In order to avoid bubble formation and unnecessary shrinkage of bulk photoresist layer, the sample was initially placed in a  $65^\circ\text{C}$  convection oven. Then the oven temperature was ramped from  $65^\circ\text{C}$  to  $95^\circ\text{C}$  in approximately five minutes and the sample was soft baked at  $95^\circ\text{C}$  for one hour or longer depending on final thickness of the photoresist layer.

After the soft curing, the sample was taken out of the oven and naturally cooled down to room temperature. Prior to UV exposure, the sample was dipped in DI water to let the photoresist

absorb moisture. Conventional UV lithography was carried out to create patterned rectangular or circular SJR5740 mesas and the sample was developed in MF354 developer (Shipley). Next, photoresist layer in the sample was thermally reflowed on a hot plate in order to convert photoresist mesa structures into the deformed photoresist mounds. Since a single step thermal reflow process caused bubble formation on the patterned photoresist layer, the sample was subjected to multiple steps of thermal reflow processes on a hot plate: initially placed at 95°C; then at 120 °C; and finally at 150 °C. Initial results of thermal reflow process showed non-uniform deformation of photoresist at upper corners of the photoresist mound structures (Figure 2.2).

In order to create uniformly deformed photoresist mound, the sample was exposed to acetone vapor before the thermal reflow process as suggested by Fletcher *et al.* [40]. The hot plate was preheated to 50 °C before acetone exposure was started. Using the apparatus as shown in Figure 2.3, the sample was placed on a 4-inch petri dish, which is placed in an acetone contained 6-inch petri dish with a spacer. Another 6-inch petri dish was placed on top of the bottom 6-inch petri dish right after the acetone was poured in so that the evaporated acetone vapor was kept inside the petri dishes and the photoresist mesa was exposed to the evaporated acetone vapor. The wafer was immediately placed on another hot plate with temperature of 50 °C. The temperature was ramped up to 95 °C and was kept at that temperature for 5 minutes. At this point, the polymeric mesa was uniformly deformed. Acetone vapor and moisture absorbed inside the polymeric mesa were removed by ramping the hot plate temperature up to 120 °C and the sample was kept at this temperature for 4 hours. The final hard curing of the mesa at 150 °C on the hot plate stabilized the mesa from further reflow in subsequent fabrication processes. Figure 2.4 shows the cross sectional view of a rectangular photoresist mesa before (top) and after

(bottom) the reflow. Note that the mesa before the reflow was slightly deformed due to heat during metal coating for SEM sample preparation. Figure 2.5 shows side view of cylindrical shape photoresist mesa before (top) and after (bottom) the reflow into a dome-shape mesa.

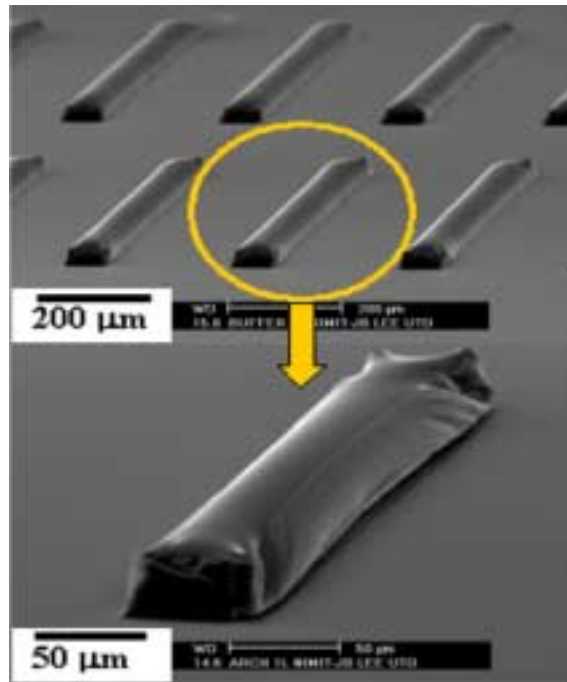


**Figure 2.2: SEM photomicrograph of non-uniform deformation at upper corners of rectangular photoresist mounds resulted from thermal reflow without exposure to acetone vapor.**

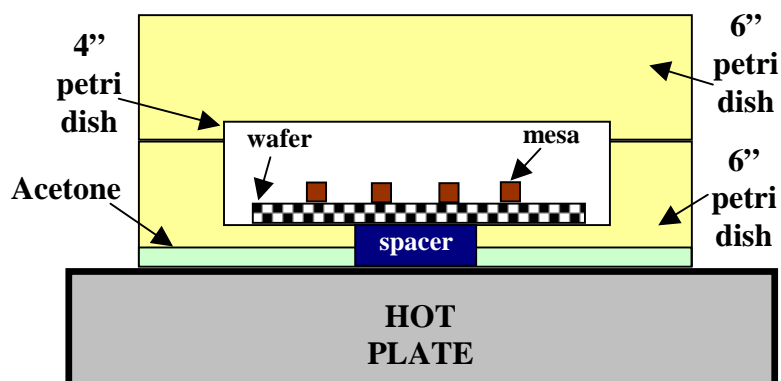


**Figure 2.3: Acetone exposure apparatus for the photoresist mesa reflow.**

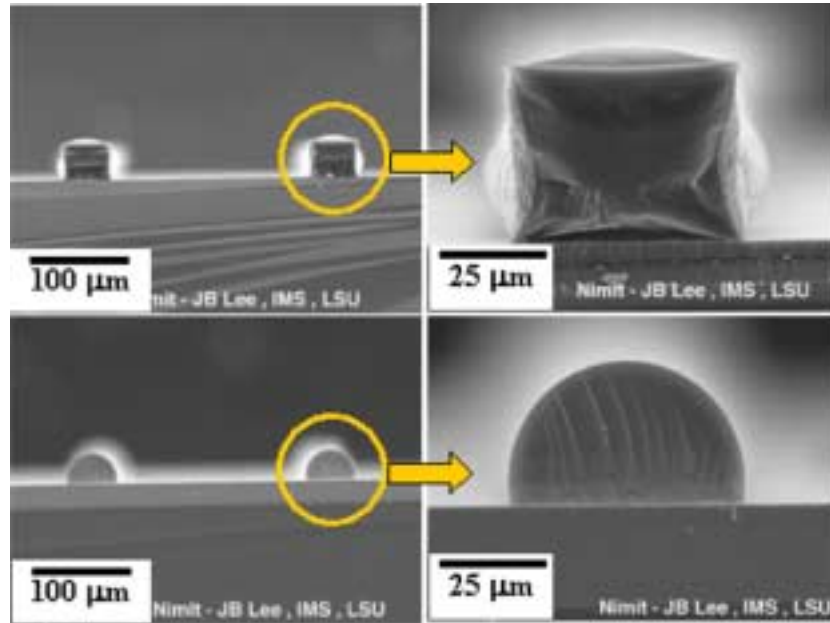


**Figure 2.4: SEM photomicrograph of cross-sectional views of rectangular photoresist mesas: before (top) and after (bottom) thermal reflow.**

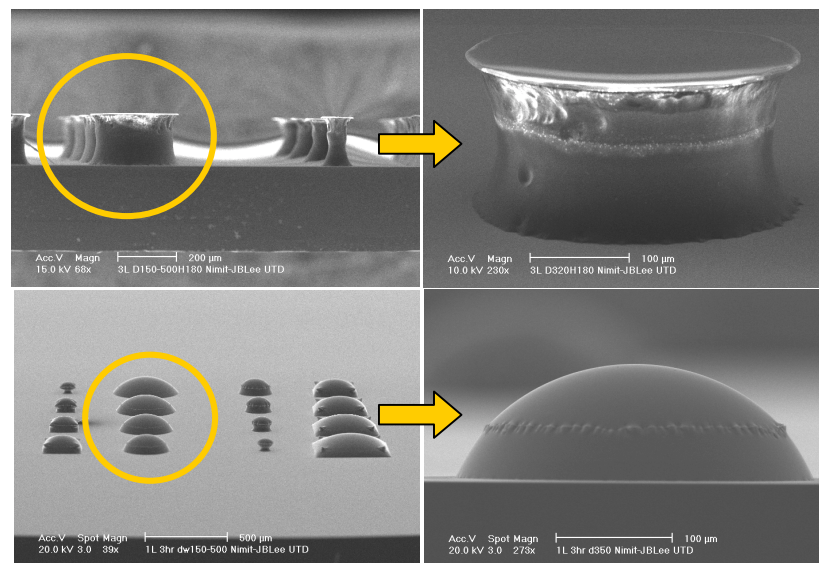


**Figure 2.5: SEM photomicrograph of cylindrical photoresist mesa: before (top) and after (bottom) thermal reflow.**

In order to investigate the limitation of this fabrication approach, the base-width of the rectangular photoresist mesa is fixed at 70  $\mu\text{m}$  and the single and double layer photoresist mesas were used as the test structures. It was found that thicker photoresist mesa (double layer) tends to reflow toward its center and move outside its original base as shown in Figure 2.6 (bottom). Table 2.2 summarizes the process parameters for SJR5740 photoresist mesa patterning and deformation. Apparently, such photoresist mesa could not be used as a sacrificial core for an arch-like 3D solenoid inductor. Based on several experiments, it was found that the aspect ratio of the rectangular mesa should not be over 1:1. Figure 2.6 (top) shows the well reflowed photoresist mesa of a single layer with approximately 1:2 aspect ratio.

Another issue in deformation of photoresist mesa is drying duration at 120 °C. It should be long enough so that further heat reflow does not occur when the hot plate temperature is ramped up to 150 °C otherwise bubbles will be generated in the photoresist and can severely damage the mesa. During long removal of sacrificial photoresist by reactive ion etching (RIE), the temperature in the RIE chamber can be high enough to cause additional reflow if the photoresist mound is not sufficiently dried. If further reflow occurs in a low pressure RIE chamber, bubble pressure inside the melting photoresist mound can burst out and damage the fabricated structures as shown in Figure 2.7. An optimized fabrication recipe is developed and utilized to fabricate three-dimensional on-chip arch-like solenoid inductors and on-chip dome-shaped spiral inductors. Fabrication procedures of such inductors will be discussed in detail in chapters 4 and 5.

## **2.3 Conformal Electrodeposition and Patterning of Photoresists**

In this section, development of a method of transferring a desired pattern of metal onto non-planar surfaces is discussed. Spin casting of photoresist onto non-planar surfaces tends to

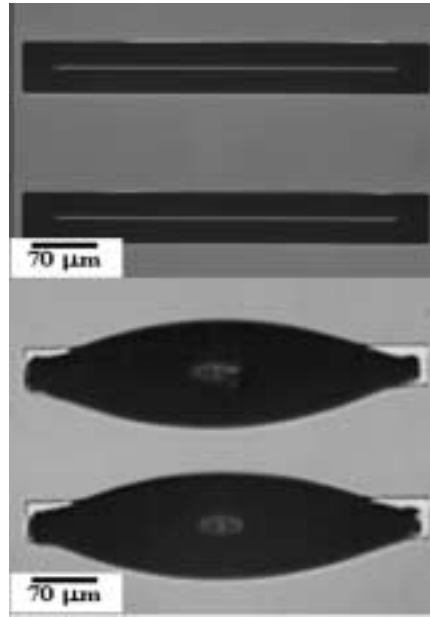


**Figure 2.6: Deformed photoresist mesas: low aspect ratio (top), and high aspect ratio (bottom)**

**Table 2.2: Process parameters for SJR5740 photoresist mesa deformation.**

Processes	Single layer	Single layer	Double layer
Spin-coating speed (rpm)	750	500	500
Film thickness after soft	30	36	96
Baking ( $\mu\text{m}$ )			
Soft bake time (at 95°C)	1 hr	1 hr	10 min + 1 hr 30 min
Moisturized by dipping in DI water	1 hr	1 hr	2 hr
UV dose ( $\text{mJ}/\text{cm}^2$ )	322	498	996
Development time (min.)	28	32	45
Acetone volume ( $\mu\text{L}$ per 1 $\text{cm}^3$ of air)	1.43	1.43	2.85
Acetone vapor exposure time (min.)	1	1	2
Reflow on hot plate at 95 °C	5 min.	5 min.	5 min.
Reflow on hot plate at 120 °C	4 hrs.	4 hrs.	4 hrs.
Reflow on hot plate at 150 °C	15 min.	15 min.	15 min.



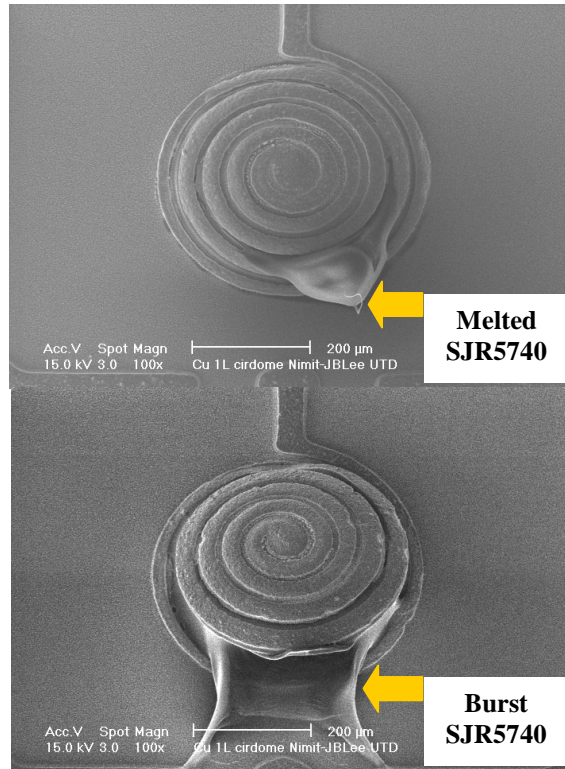


**Figure 2.7: Burst in a photoresist mound in a RIE chamber due to insufficient drying.**

have a thinner resist at the protruding top area and a thicker resist at the bottom area. This makes the UV exposure and development process difficult due to significant variation in resist thickness between the top and the bottom areas of non-planar structures. To reduce this problem, a method that can conformally deposit photoresist must be devised. In this work, electrodeposition of photoresist was utilized and optimized for the conformal deposition of photoresist on non-planar reflowed sacrificial polymeric mounds.

Prior to working on the reflowed sacrificial polymeric mounds, three-dimensional test structures are utilized to develop conformal photoresist deposition and subsequent patterning of metallic traces on non-planar surfaces. Two aqueous-based photoresists namely positive tone PEPR2400 (Shipley) and negative tone Eagle2100 (Shipley) were used for electrodeposition on

three-dimensional non-planar test structures such as bulk-micromachined silicon wells and polymer channels.

The first test structure, a square silicon well (700  $\mu\text{m}$  by 700  $\mu\text{m}$  and 175  $\mu\text{m}$  deep) was fabricated by crystallographic selective bulk micromachining using thermally grown silicon dioxide ( $\text{SiO}_2$ ) as an etch mask. The process has been done by forming a 0.4  $\mu\text{m}$  thick thermal oxide on silicon wafer with (100) crystal orientation, followed by UV lithography and silicon dioxide etching in order to define a rectangular open area. The native thin silicon dioxide inside the open area was removed by briefly rinsing the sample in a 5% hydrofluoric acid (HF) solution. The bulk silicon inside the opening area was removed by wet etching in a 25 % by weight potassium hydroxide (KOH) solution at 70  $^{\circ}\text{C}$  for 5 hours. The etching rate of 0.6  $\mu\text{m}/\text{min}$  of silicon bulk in (100) plane was observed while the etching rate of silicon in (111) plane is negligible. Figure 2.8 shows a 175  $\mu\text{m}$ -deep silicon well fabricated by this method.

Another non-planar test structure is a polymer channel. The channel was fabricated by spin-coating of PI2611 polyimide (HD Microsystems) onto a silicon or glass substrate. Three layer coating scheme yields a polymer composite layer with approximate thickness of 75  $\mu\text{m}$ . After the spin-coating and hard baking steps, the polymer layer was etched by dry etching in oxygen ( $\text{O}_2$ ) plasma using thick aluminum layer as an etch mask. By mixing carbon tetrafluoride ( $\text{CF}_4$ ) with oxygen in different ratios, the etching rate of the polymer can be varied. The study of PI2611 polyimide in  $\text{O}_2$  and  $\text{CF}_4$  plasma etching in a PlasmaTherm 70 Series plasma etcher showed that adding about 3%  $\text{CF}_4$  into  $\text{O}_2$  can yield the maximum etch rate with a gas pressure of 300 mTorr and RF power of 300 W. Figure 2.9 shows the etch rates in both vertical and horizontal directions. Dry etching of these test structures in PI2611 resist to form channels was performed by sputter-coating 1.3  $\mu\text{m}$  thick aluminum film on PI2611 composite layer, followed

by UV lithography to open etching windows in aluminum mask layer. With a pattern of long lines (5 mm in length and 25  $\mu\text{m}$  in width), the U-shape polymer channels were obtained as shown in Figure 2.10.

The detail investigation of electrodeposition of PEPR2400 has been carried out by Linder [43] for chip stack memory packaging applications. The development given here is based on Linder's investigation. In this work, the photoresist was diluted with DI water at volume ratio of 1:7 to be used as an electroplating bath. Since PEPR2400 micelles have negative charges, a sheet of stainless steel was used as a cathode and the sample was used as an anode so that the resist micelles can be deposited onto the sample.

Before performing electrodeposition, the surface of plating base was cleaned in a 5% sulfuric acid solution to remove native copper oxide. Electrodeposition was carried out in constant voltage mode at 250 VDC for approximately 7 minutes to obtain a 5  $\mu\text{m}$ -thick conformal photoresist layer. The sample was briefly rinsed in DI water and soft baked in an oven at 105  $^{\circ}\text{C}$  for 30 minutes.

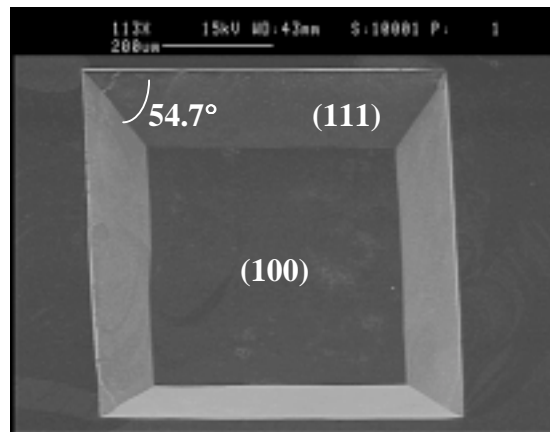


**Figure 2.8: A non-planar silicon well test structure 700x700  $\mu\text{m}$  and 175  $\mu\text{m}$  deep.**

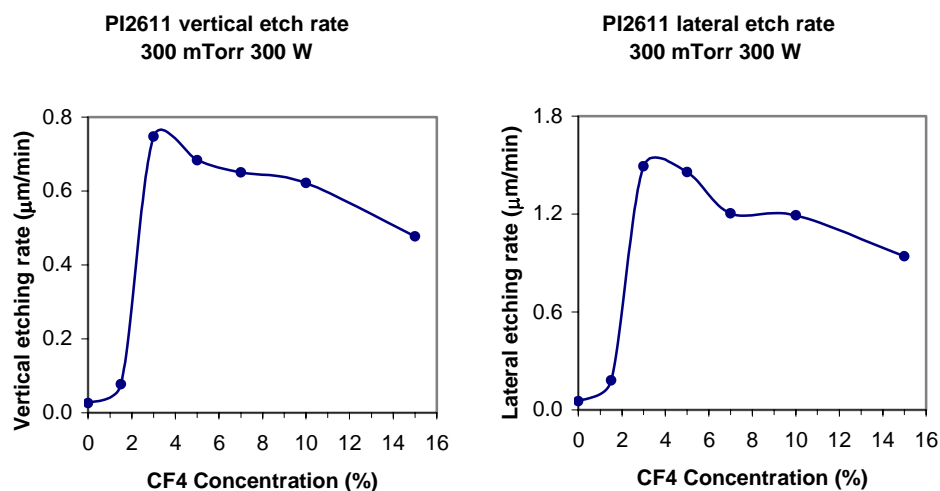


**Figure 2.9: Plasma etch rates for PI2611 resist at various  $\text{CF}_4$  concentrations in oxygen.**

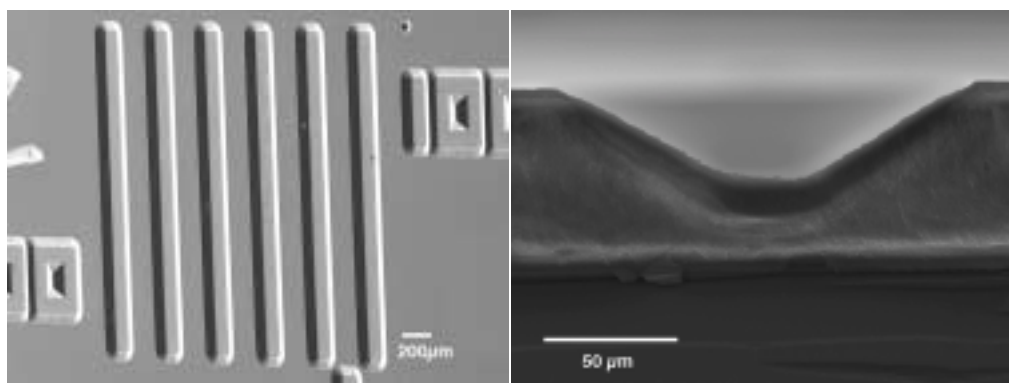


**Figure 2.10: A non-planar PI2611 polymer channels test structure 70  $\mu\text{m}$  deep.**

The soft baked layer of PEPR2400 photoresist was patterned with standard contact UV mask aligner. The pattern development was carried out in a 1% by weight sodium carbonate ( $\text{Na}_2\text{CO}_3$ ) solution at 35  $^{\circ}\text{C}$ . The patterned PEPR2400 photoresist was used as an electroplating mold of nickel. Figure 2.11 shows the 70  $\mu\text{m}$  wide electroplated nickel lines formed along the

surface profile of the 175  $\mu\text{m}$  deep silicon well with PEPR2400 conformal electroplating mold. In this figure, PEPR2400 photoresist mold was removed in acetone for clarity.

It can be seen that the widths of nickel lines at the top and the bottom of silicon well are different. At the top of the well, the line width is close to that of the photomask. Due to the use of contact mask aligner, the distance between the bottom of the silicon well and the photomask is large and it allows more diffracted UV light to pass through and widen the line pattern. This effect limits the resolution of the pattern on non-planar structures when a contact mask aligner is used. Figure 2.12 shows a 70  $\mu\text{m}$  wide electroplated nickel lines deposited along the surface profile of a 25  $\mu\text{m}$  deep polyimide channels with a PEPR2400 conformal electroplating mold.

Conformal electrodeposition and subsequent patterning of negative tone Eagle2100 photoresist onto non-planar three-dimensional structures has been investigated in detail by Kersten *et al.* [44]. This process has been modified and optimized for fabrication of three-dimensional on-chip inductors in this work. The photoresist was diluted with DI water at volume ratio of 2:1 and used as an electroplating bath. Since Eagle2100 micelles have positive charges, a sheet of stainless steel was used as an anode and the sample was used as a cathode so that the resist micelles can be deposited onto the sample. Deposited photoresist thickness depends

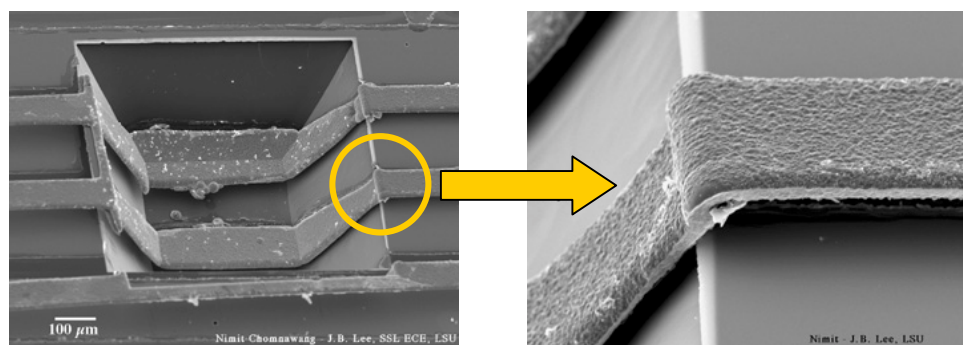


**Figure 2.11: 70  $\mu\text{m}$  wide electroplated nickel lines patterned on a 175  $\mu\text{m}$  deep silicon well. The sacrificial PEPR2400 photoresist mold has been removed.**

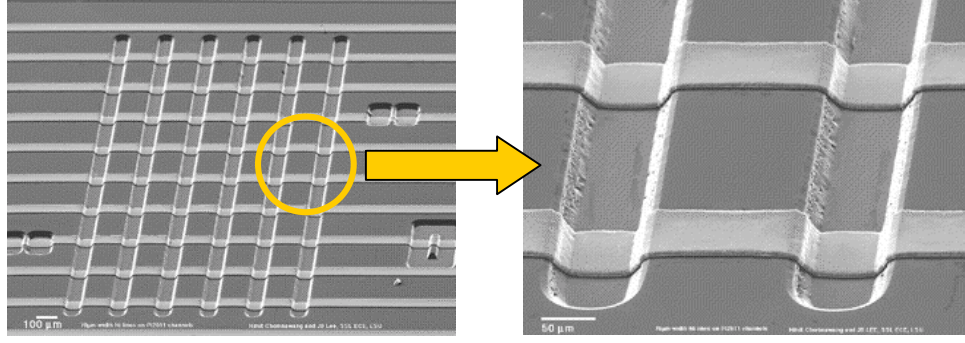


**Figure 2.12: The 70  $\mu\text{m}$  wide electroplated nickel lines on 25  $\mu\text{m}$  deep polyimide channels. The sacrificial PEPR2400 photoresist mold has been removed.**

on the electroplating condition such as temperature and bias voltage. A test was carried out to find relation between the bias voltage and the resulting photoresist thickness while keeping deposition temperature constant at room temperature. Before electrodeposition, the plating-base surface was cleaned in a 5% sulfuric acid solution to remove native copper oxide. The sample was rinsed in DI water and dipped into the plating bath. Plating current was monitored and recorded by a multi-meter for a given electrode bias voltage. Since the photoresist film deposited on the sample is an insulator, electroplating automatically stops (a so-called self-termination process) after a certain time and resist thickness. Figure 2.13 shows self-termination deposition time at various bias voltages. At bias voltage at or above 40 V, the total deposition time is approximately 20 seconds. The recorded plating current, as a function of time, is shown in Figure 2.14. The sample was gently rinsed in DI water to remove excess photoresist that was not electrically deposited. The sample was then dried naturally in the air. As suggested by Kersten *et al.* [45], pre-exposure drying of the photoresist was done in vacuum below 100 mTorr for 4 hours instead of soft baking to avoid photoresist reflow. After drying, UV exposure was done using the data summarized in Table 2.3. Development was carried out, with no post-exposure baking, by

gently dipping the sample in a 1:24 diluted solution of Eagle2005 developer and DI water at 38 °C. The sample was gently rinsed in DI water and dried naturally in the air. Film thickness was then measured with a stylus profiler. Figure 2.15 shows the electrodeposited photoresist thickness for various bias voltages.

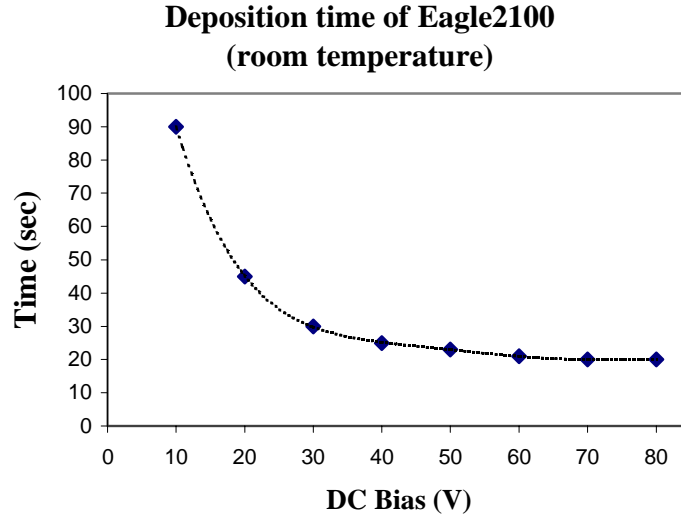


**Figure 2.13: Deposition time for Eagle2100 photoresist at various bias voltages.**

In order to use the patterned Eagle2100 layer as an electroplating mold, the sample was cleaned by oxygen reactive ion etching for at least 20 minutes at 200 W RF power and 200 mTorr pressure. Figure 2.16 shows the patterned electrodeposited Eagle2100 photoresist mold on a dome structure with 70  $\mu\text{m}$  tall and 800  $\mu\text{m}$  in base diameter and a copper track electroplated into the mold. Patterning of Eagle2100 photoresist on non-planar surfaces has the same problems to that of PEPR2400 resist in which the widths of the patterns of the top and the bottom of the structures are different. At the top areas of the structures, the size of opening windows is close to that of the photomask. The long distances from the lower parts of the structures to the photomask

allow more diffracted UV light to pass through and hence narrows the developed window openings. This effect limits the resolution of the pattern on non-planar structures.

## 2.4 Removal of Sacrificial Polymeric Layers

Since multi-layers of polymeric and metallic layers are used for the fabrication of three-dimensional on-chip inductors, etch/release processes are needed to obtain free-standing inductors. Materials that need to be removed include Cr/Cu/Cr or Ti/Cu/Ti plating base, electrodeposited photoresists, sacrificial photoresist core or support, and photoresist molds. Removal of Cr and Ti layer can be done in wet etchants as shown in Table 2.1.

The PEPR2400 photoresist mold can be primarily removed by acetone and the residue can be removed by 1% sodium hydroxide (NaOH) solution at temperature above 55 °C. Similarly, the Eagle2100 photoresist mold and SJR5740 photoresist can be initially removed by acetone, followed by reactive ion etching in a gas mixture of 10% CF<sub>4</sub> in O<sub>2</sub> at a gas pressure of 200 mTorr and RF power of 345 Watts. The RIE conditions above give etch rate of Eagle2100 and SJR5740 of approximately 0.25 and 2 μm/min, respectively. Figure 2.17 shows copper spiral track on a dome structure after the Eagle2100 photoresist mold was removed.

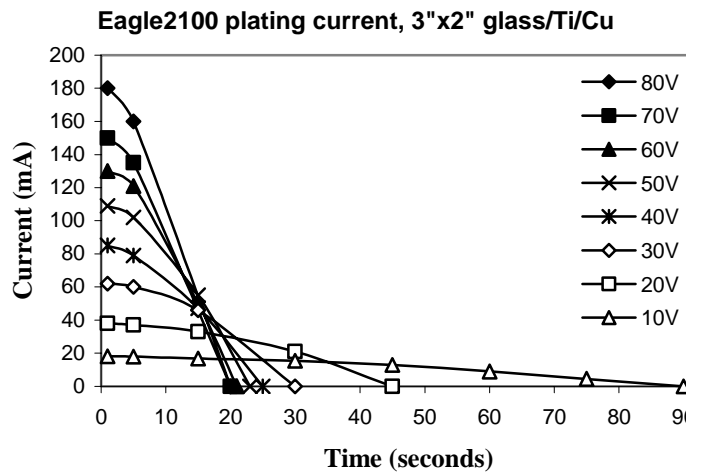


**Figure 2.14: Plating current for Eagle2100 photoresist as a function of time.**



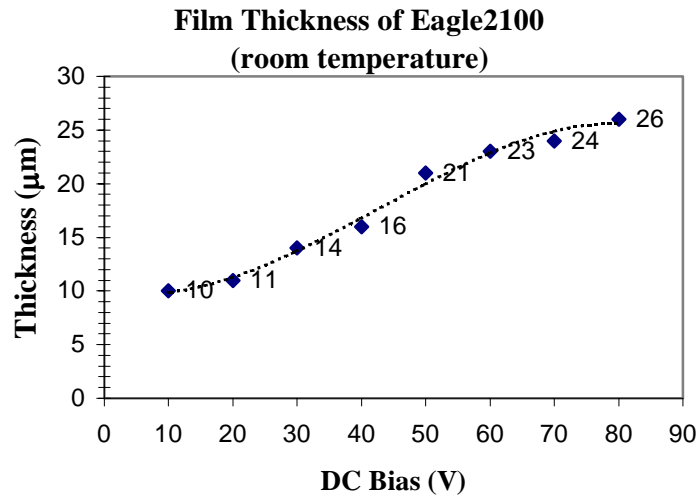


**Figure 2.15: Thickness of Eagle2100 photoresist deposited at various bias voltages.**

**Table 2.3: Summary of UV exposure dose and developing time for EAGLE2100.**

DC bias (V)	Thickness (μm)	UV dose (mJ/cm <sup>2</sup> )	Developing time (min)	Film condition
10	10	150	1.0	Not uniform
20	11	165	1.5	Uniform
30	14	180	2.0	Uniform
40	16	208	2.5	Uniform
50	21	208	3.0	Uniform
60	23	220	3.5	Uniform
70	24	274	4.0	Uniform
80	26	300	4.5	Uniform

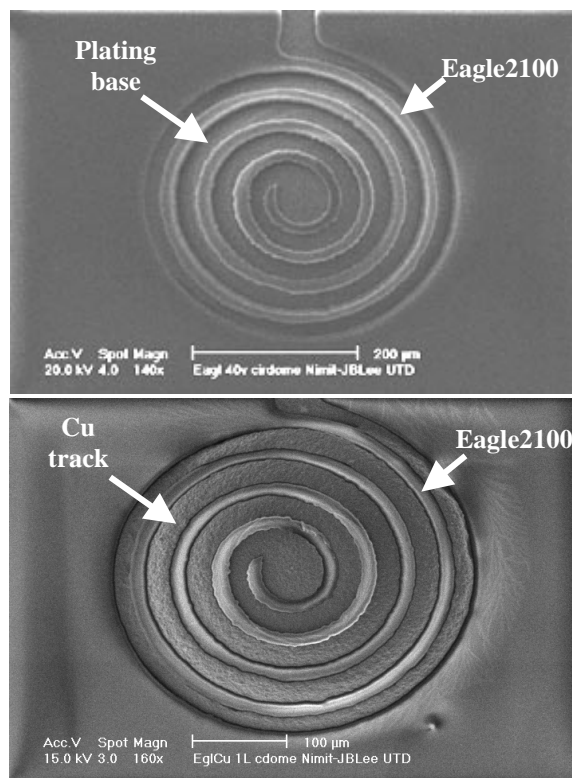


**Figure 2.16: SEM photomicrograph of an Eagle2100 photoresist mold deposited on a dome structure (top), and a copper spiral track electroplated into the photoresist mold (bottom).**

Although wet etch using liquid phase etchants such as 1-methyl-2-pyrrolidinone (NMP) is used to remove SU-8 film at temperatures above 70 °C, it cannot be used to remove SU-8 photoresist mold with fine metallic structures. It is because SU-8 is not dissolved in this etchant, but chunks of SU-8 directly are displaced from the sample into the solution and they are very slowly dissolved outside of the sample. Such bulk SU-8 chunks displacement from the sample damages metallic fine structures. Therefore, removal of SU-8 photoresist mold is done using dry etch method in either RIE or a barrel plasma etcher. In RIE, a gas mixture of 10%  $\text{CF}_4$  in  $\text{O}_2$  at gas pressure of 200 mTorr, and RF power of 345 Watts are used. These conditions give SU-8

etch rate of 10  $\mu\text{m}/\text{min}$ . Figure 2.18 shows an example of electroplated copper transmission line in which SU-8 was completely removed by dry etch using RIE.

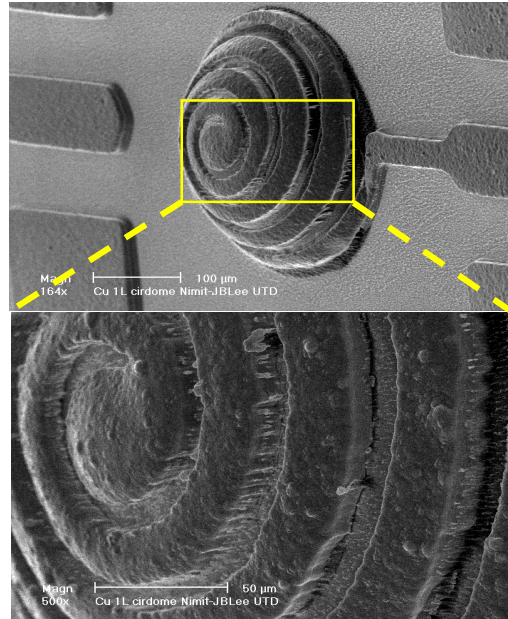


**Figure 2.17: SEM photomicrograph of an electroplated copper track on a dome structure after the removal of Eagle2100 photoresist mold.**

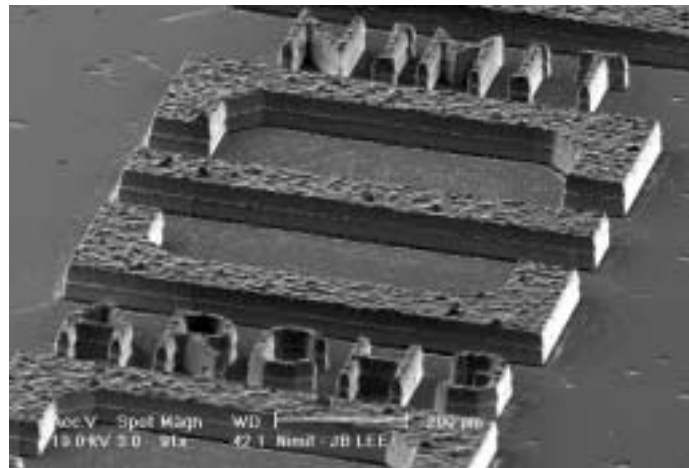


**Figure 2.18: SEM photomicrograph of electroplated copper transmission line structures after two layers of SU-8 mold of 30  $\mu\text{m}$  each were removed by reactive ion etching.**

Typically RIE gives relatively anisotropic etch (faster etch in vertical direction than in lateral directions) profile while barrel plasma etch gives isotropic etch (comparable etch rates in both vertical and lateral directions) profile. The barrel plasma etch is suitable for the release of polymers deep underneath metallic structures, which is not accessible for RIE systems. A disadvantage of barrel plasma etcher is that copper microstructures can be severely oxidized during etching. The oxidized copper structures are etched quickly during removal of plating base layers. This creates unnecessary thickness loss of copper structures. This oxidation of copper structures does not occur in reactive ion etching. A combination of RIE/barrel plasma etching scheme can be used to maximize vertical etching of SU-8 by RIE followed by lateral etching by barrel plasma etching. In order to avoid thickness loss of copper structures, only reactive ion etching is used in fabrication of three-dimensional inductors in this work. This results in remaining negligible SU-8 residues underneath some parts of the inductors.

## CHAPTER 3

### HIGH FREQUENCY MEASUREMENT AND MODELING METHODS

Electrical characteristics and small signal performances of low-frequency electronic devices are typically done by measurement of voltage, current and their related quantities such as impedances and admittances. Unlike low frequency characterizations, at high frequencies, voltage and current are difficult to measure since the signals must be treated as traveling electromagnetic waves. Therefore, characterizations of passive components at high frequencies need a dedicated high frequency measurement setup and need special attention to minimize measurement errors. This chapter describes high frequency on-wafer measurement methods and equivalent circuit modeling methods for on-chip microinductors to be fabricated. First section describes high frequency on-wafer measurement methods and the second section describes equivalent circuit modeling methods in detail.

#### 3.1 High Frequency On-wafer Measurement Methods

In order to explain and predict their behavior, electronic devices can be represented by a network of circuit model parameters. The models are usually in forms of two-port network as shown in Figure 3.1 (a). Impedance (Z-parameters), admittance (Y-parameters) [46] and transmission matrix (ABCD-parameters) [50] of two-port networks can be represented by the well-known Equations (3.1)-(3.6), respectively.

$$\text{Z-parameters:} \quad V_1 = z_{11}I_1 + z_{12}I_2 \quad (3.1)$$

$$V_2 = z_{21}I_1 + z_{22}I_2 \quad (3.2)$$

$$\text{Y-parameters:} \quad I_1 = y_{11}V_1 + y_{12}V_2 \quad (3.3)$$

$$I_2 = y_{21}V_1 + y_{22}V_2 \quad (3.4)$$

$$\text{Z-parameters:} \quad V_1 = AV_2 + BI_2 \quad (3.5)$$

$$I_1 = CV_2 + DI_2 \quad (3.6)$$

Since voltage and current can be measured relatively easily at low frequencies with a typical multi-meter or an oscilloscope, these quantities are widely used in low-frequency measurements. At high frequencies, however, voltage and current are difficult to measure since the signals must be treated as traveling electromagnetic waves. The traveling electromagnetic waves can be measured in terms of scattering and reflection. At high frequencies, the parameters describing a network relating the scattered and reflected traveling electromagnetic waves are called scattering parameters or S-parameters. Figure 3.1 (b) illustrates two-port networks for S-parameters. Equations (3.7)-(3.12) are linear equations describing the two-port network [46], where  $a_1$  and  $a_2$  are incident electromagnetic waves and  $b_1$  and  $b_2$  are reflected electromagnetic waves. The  $s_{11}$  and  $s_{22}$  are input and output reflection coefficients, and  $s_{21}$  and  $s_{12}$  are forward and reverse transmission coefficients, respectively.

$$b_1 = s_{11}a_1 + s_{12}a_2 \quad (3.7)$$

$$b_2 = s_{21}a_1 + s_{22}a_2 \quad (3.8)$$

$$s_{11} = \left. \frac{b_1}{a_1} \right|_{a_2=0} \quad (3.9)$$

$$s_{22} = \left. \frac{b_2}{a_2} \right|_{a_1=0} \quad (3.10)$$

$$s_{21} = \left. \frac{b_2}{a_1} \right|_{a_2=0} \quad (3.11)$$

$$s_{12} = \left. \frac{b_1}{a_2} \right|_{a_1=0} \quad (3.12)$$

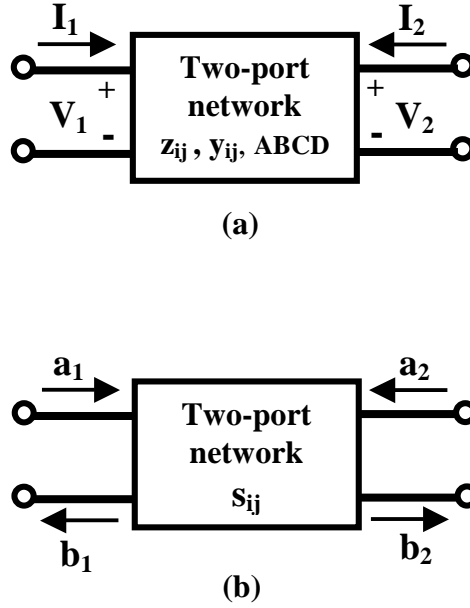


**Figure 3.1: Diagrams of two-port networks (a) for Y, Z and ABCD-parameters, and (b) for S-parameters.**

In order to perform high frequency characterizations of on-chip inductors, on-wafer S-parameter measurement method is desirable since the parasitic effects of the off-wafer fixtures and wires are minimized. The on-wafer probe pads and transmission line ground planes can be directly fabricated onto the substrate along with the on-chip inductor. Since the presence of ground planes and probe pads next to the device under test (DUT) can add some parasitics into the measurement results, de-embedding of these parasitics are crucial in order to obtain the correct characteristics of the DUT.

Exclusion of parasitic effects of probe pads and ground planes can be done by fabricating dummy devices consisting only of probe pads and ground planes (PAD) on the substrate near by the device under test as shown in Figure 3.2. By measuring S-parameters of both DUT and PAD, and subtracting effects of PAD out of those of DUT, accurate measurements for the inductors alone can be obtained.

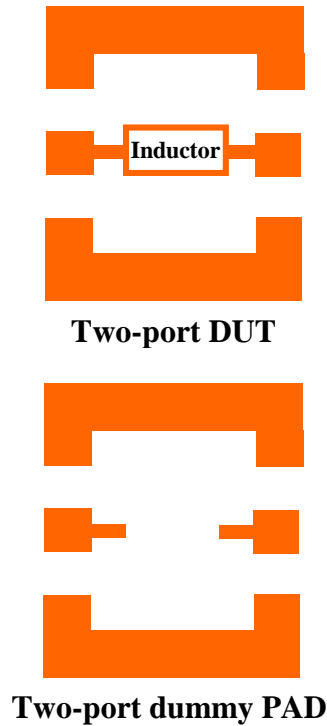


**Figure 3.2: Device under test (DUT) and dummy probe pads (PAD) for de-embedding parasitic effects.**

Typical measurement setup for high frequency characterization is a combination of vector network analyzer, S-parameter test set and a frequency sweeper. Figure 3.3 is one example of such a measurement setup consisting of Agilent 8510C vector network analyzer, HP8340B 10 MHz-26.5 GHz synthesized frequency sweeper, HP8515A S-parameters test setup, and ground-signal-ground (GSG) 40A-GSG-200-P on-wafer microprobes (GGB Industries).

Prior to S-parameters measurements, the measurement setup must be calibrated with a high frequency calibration standard. In this work, CS-5 (GGB Industries) impedance standardsubstrate (ISS) with open-short-load-thru (OSLT) calibration procedure as shown in Figure 3.4 were used to remove all parasitics in the cables and connectors and set the reference



plane for the probe tips. The parallel  $100\ \Omega$  resistors in Figure 4.3 (c) provide calibration for the effective  $50\ \Omega$  system.

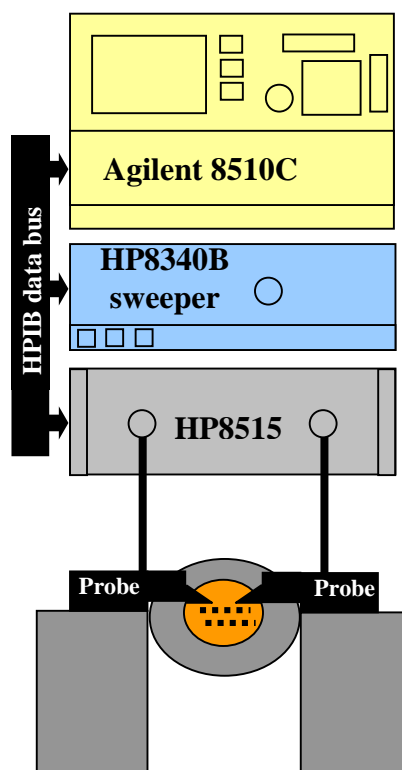


**Figure 3.3: Measurement setup consisting of an Agilent 8510C vector network analyzer, HP8340B synthesized sweeper, HP8515A S-parameter test setup and high frequency probes for on-wafer testing.**

S-parameters of the DUT and the PAD can be measured and the S-parameter data can be stored as text files in CITIFILE standard format. In order to process S-parameter data easily, the data in CITIFILE format can be converted into the widely used Touchstone format by a MATLAB computer program `citi2touch.m` as shown in Appendix C in this dissertation.

Once the PAD data and the DUT data are obtained, the PAD data must be subtracted out of DUT data so that one can have accurate data for the DUT without any parasitics. Two parasitics de-embedding methods have been used in the literatures. Arcioni *et al.* converted S-

parameter matrices of the DUT and the PAD into ABCD-parameter metrices. The inverse matrices of ABCD-parameters of the PAD were multiplied in front of and behind that of the DUT, resulting in a de-embedded ABCD-parameter matrix which in turn is converted into Y-parameters for usage in inductor modeling [47]. P. J. van Wijnen *et al.* performed de-embedding simply by converting S-parameter matrices of the DUT and the PAD into Y-parameter matrices and then subtracting Y-parameters of the PAD out of those of the DUT [48]. Both methods were tested in this work. The results from both methods were found identical. Since matrix subtraction is easier than matrix inversion and multiplication, de-embedding by Y-parameter subtraction method is used in this work..

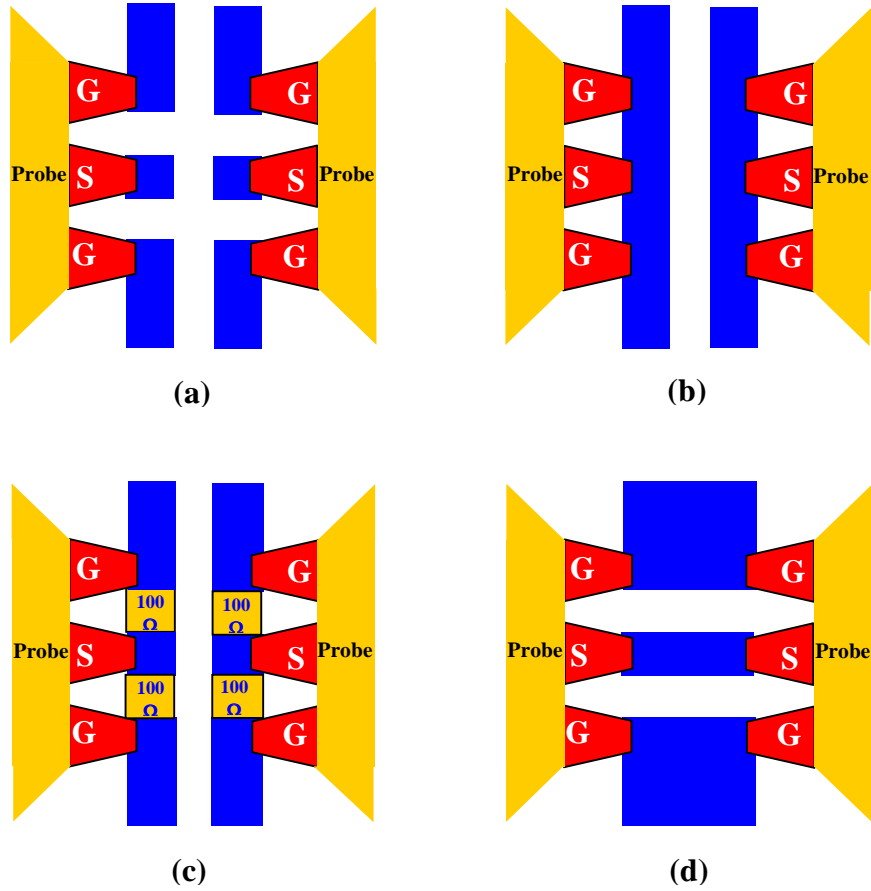


**Figure 3.4: Open-short-load-thru calibration procedures of the on-wafer probes**  
 (a) open, (b) short, (c) 50  $\Omega$  load (parallel 100  $\Omega$ ), and (d) thru.

S-parameters of both inductor with probe pads (DUT) and S-parameters of probe pads only (PAD) are converted into Y-parameters (admittances) using Equations (3.13)-(3.16) for two-port inductors and Equation (3.15) for one-port inductors [46].

$$y_{11} = \frac{1}{Z_0} \frac{(1-s_{11})(1+s_{22}) + s_{12}s_{21}}{(1+s_{11})(1+s_{22}) - s_{12}s_{21}} \quad (3.13)$$

$$y_{12} = \frac{1}{Z_0} \frac{-2s_{12}}{(1+s_{11})(1+s_{22}) - s_{12}s_{21}} \quad (3.14)$$

$$y_{21} = \frac{1}{Z_0} \frac{-2s_{21}}{(1+s_{11})(1+s_{22}) - s_{12}s_{21}} \quad (3.15)$$

$$y_{22} = \frac{1}{Z_0} \frac{(1+s_{11})(1-s_{22}) + s_{12}s_{21}}{(1+s_{11})(1+s_{22}) - s_{12}s_{21}} \quad (3.16)$$

where  $Z_0 = 50 \, \Omega$  and  $Y_0 = 0.2 \, S$  are characteristic impedance and admittance of the system, respectively.

In order to obtain the parasitics de-embedded Y-parameters of the inductor only, Y-parameters of the probe pads were subtracted from the inductor with probe pads as shown in Equation (3.17). These de-embedded Y-parameters include only the effect of the inductors and the substrates. Modeling of equivalent inductor circuits is discussed in the next subsection.

$$\begin{bmatrix} y_{11} & y_{12} \\ y_{21} & y_{22} \end{bmatrix}_{\text{De-embedded}} = \begin{bmatrix} y_{11} & y_{12} \\ y_{21} & y_{22} \end{bmatrix}_{\text{Inductor with probe pads}} - \begin{bmatrix} y_{11} & y_{12} \\ y_{21} & y_{22} \end{bmatrix}_{\text{Probe pads only}} \quad (3.17)$$

The de-embedded S-parameters can be converted back from the de-embedded Y-parameters [46] using Equations (3.18)-(3.21).

$$s_{11} = \frac{(1 - y_{11}Z_0)(1 + y_{22}Z_0) + y_{12}y_{21}Z_0^2}{(1 + y_{11}Z_0)(1 + y_{22}Z_0) - y_{12}y_{21}Z_0^2} \quad (3.18)$$

$$s_{12} = \frac{-2y_{12}Z_0}{(1 + y_{11}Z_0)(1 + y_{22}Z_0) - y_{12}y_{21}Z_0^2} \quad (3.19)$$

$$s_{21} = \frac{-2y_{21}Z_0}{(1 + y_{11}Z_0)(1 + y_{22}Z_0) - y_{12}y_{21}Z_0^2} \quad (3.20)$$

$$s_{22} = \frac{(1 + y_{11}Z_0)(1 - y_{22}Z_0) + y_{12}y_{21}Z_0^2}{(1 + y_{11}Z_0)(1 + y_{22}Z_0) - y_{12}y_{21}Z_0^2} \quad (3.21)$$

MATLAB program de-embed.m in Appendix C converts S-parameters of DUT and PAD into Y-parameters, subtract admittances of PAD out of those of DUT and converts the resulted Y-parameters into de-embedded S-parameters to be used as a corrected measurement data in circuit modeling.

### 3.2 Equivalent Circuit Modeling Methods of On-chip Inductors

On-chip inductors are typically used in high frequency circuits in both floating and shunt configurations. For floating configuration, the inductor is a two-port network in which neither port is grounded. In shunt configuration, one port of the inductor is connected to a part of the circuit while the second port is grounded. Since the model of shunt inductor can be derived from the model of a floating inductor by grounding one of the two ports, a two-port model for inductors is used in this work. Conventionally, on-chip inductors are modeled as a  $\pi$ -network with the series branch consisting of an inductance in series with a resistance, and each shunt branch consisting of a capacitance in series with a resistance [25, 49] as shown in Figure 3.5.

In order to determine the values of inductance, resistances and capacitances in this model, the measured de-embedded S-parameters can be directly converted into ABCD-parameters [50, 51] using Equations (3.22)-(3.25).

$$A = \cosh(l\gamma) = \frac{(1 + s_{11})(1 - s_{22}) + s_{12}s_{21}}{2s_{21}} \quad (3.22)$$

$$B = Z_0 \sinh(l\gamma) = Z_0 \frac{(1 + s_{11})(1 + s_{22}) - s_{12}s_{21}}{2s_{21}} \quad (3.23)$$

$$C = \frac{1}{Z_0} \sinh(l\gamma) = \frac{1}{Z_0} \frac{(1 - s_{11})(1 - s_{22}) - s_{12}s_{21}}{2s_{21}} \quad (3.24)$$

$$D = \cosh(l\gamma) = \frac{(1 - s_{11})(1 + s_{22}) + s_{12}s_{21}}{2s_{21}} \quad (3.25)$$

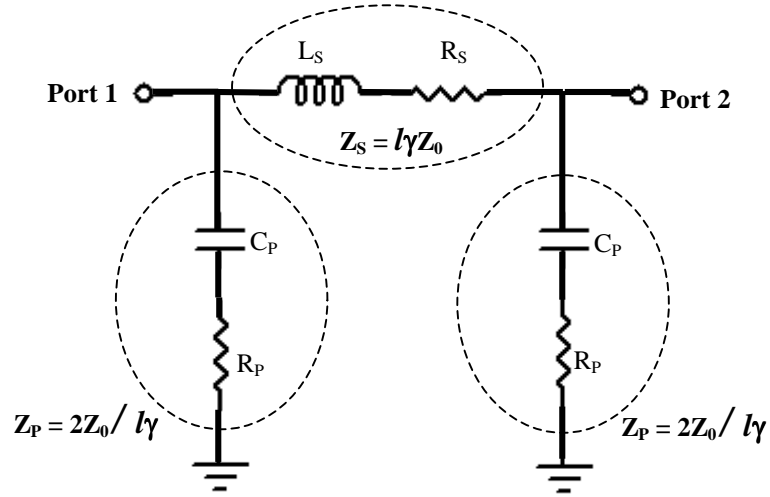
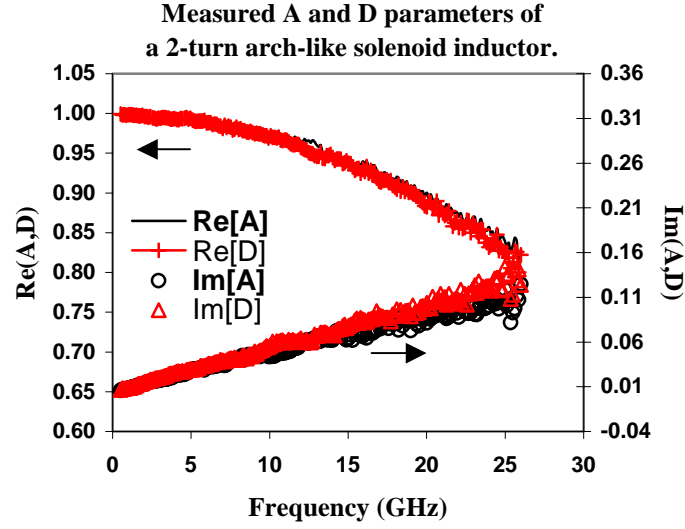


**Figure 3.5: Traditional model of a two-port on-chip inductor.**

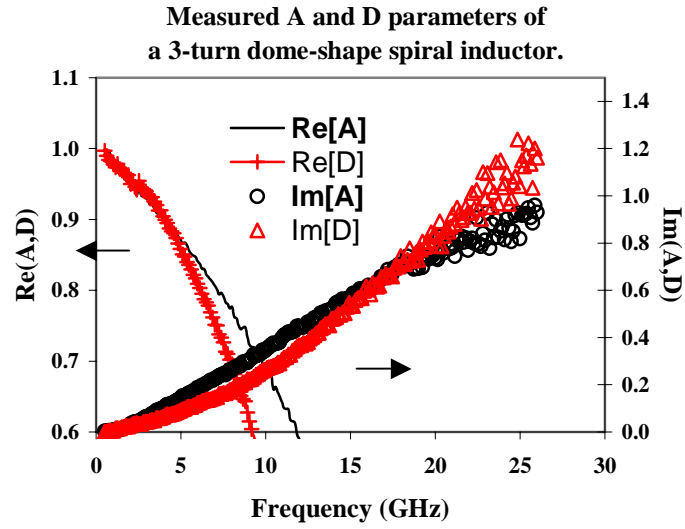
The A and D parameters of a 2-turn arch-like solenoid inductor and a 3-turn dome-shaped solenoid inductor were measured. Their real and imaginary parts were plotted as shown in Figure 3.6 (a) and (b), respectively. Since the A and D parameters are almost equal, their average value is used in calculation of the product of the wave propagation constant and the propagation path length  $l\gamma$  at each frequency as shown in Equation (3.26).

The resulting value of  $l\gamma$  is then used to determine the characteristic impedance of the propagation path using Equation (3.27).

$$l\gamma = \cosh^{-1}\left(\frac{A+D}{2}\right) \quad (3.26)$$



(a)



(b)

Figure 3.6: Comparison of the measured A and D parameters of (a) an arch-like solenoid inductor, and (b) a dome-shaped spiral inductor.

$$Z_0 = \frac{B}{\sinh(l\gamma)} \quad (3.27)$$

Knowing  $l\gamma$  and  $Z_0$ , the complex impedance  $Z_S$  and  $Z_P$  of each series and shunt branch in the  $\pi$ -network can be calculated using Equations (3.28)-(3.29). Here, the propagation path length  $l$  need not be calculated since the product  $l\gamma$  is used in all calculations.

$$Z_S = Z_0 l\gamma \quad (3.28)$$

$$Z_P = \frac{2Z_0}{l\gamma} \quad (3.29)$$

Equations (3.30)-(3.35) show the extractions of the corresponding  $L_S$ ,  $R_S$ ,  $R_P$  and  $C_P$  values from  $Z_S$  and  $Z_P$ .

$$Z_S = R_S + j\omega L_S \quad (3.30)$$

$$R_S = \text{Re}(Z_S) \quad (3.31)$$

$$L_S = \frac{\text{Im}(Z_S)}{\omega} \quad (3.32)$$

$$Z_P = R_P - \frac{1}{\omega C_P} j \quad (3.33)$$

$$R_P = \text{Re}(Z_P) \quad (3.34)$$

$$C_P = \frac{-1}{\omega \text{Im}(Z_P)} \quad (3.35)$$

The Y-parameters of the traditional  $\pi$ -model for inductors can be directly determined from the  $\pi$ -network series and shunt impedances [47] as shown in Equations (3.36) and (3.37). The S-parameters are then converted from Equations (3.18)-(3.21).

$$y_{21} = y_{12} = -\frac{1}{Z_S} = -\frac{1}{R_S + j\omega L_S} \quad (3.36)$$

$$y_{11} = y_{22} = \frac{1}{Z_S} + \frac{1}{Z_P} = \frac{1}{R_S + j\omega L_S} + \frac{1}{R_P - j\frac{1}{\omega C_P}} \quad (3.37)$$

The Q-factor of an inductor can be calculated from the measured data from the ratio of the imaginary parts to the real parts of the equivalent one-port input impedance. The latter is transformed from a two-port network by grounding one of the ports [47]. This equivalent one-port input impedance can be calculated using Equation (3.38). The measured Q-factor can be calculated from Equation (3.39).

$$Z_{in} = \frac{1}{\frac{1}{Z_P} + \frac{1}{Z_S}} \quad (3.38)$$

$$Q = \frac{\text{Im}(Z_{in})}{\text{Re}(Z_{in})} \quad (3.39)$$

In order to determine the Q-factor from the traditional inductor model, the equivalent one-port input impedance of the model is calculated using Equation (3.40). Its imaginary and real parts are used to find Q-factor of the model using Equation (3.39).

$$Z_{in} = \frac{1}{\frac{1}{R_P} + j\omega C_P + \frac{1}{R_S + j\omega L_S}} \quad (3.40)$$

Although the traditional inductor model is easily implemented by extracting parameter from the measured  $\pi$ -network, its parameters do not represent the physical conditions of on-chip inductors because it does not take into account the inter-turn fringing capacitances. Figure 3.7 shows a physical circuit model [49] that better represents an on-chip inductor. This physical model is a two-port  $\pi$ -network of series and shunt components of inductor, capacitors.

At the series branch of the  $\pi$ -network, model parameters  $L_S$ ,  $R_S$  and  $C_S$  represent series inductance, series resistance and inter-turn fringing capacitance of the inductor, respectively. In addition, the shunt branch of the  $\pi$ -network represents parasitic components of conductive substrate that has influence on the inductors.



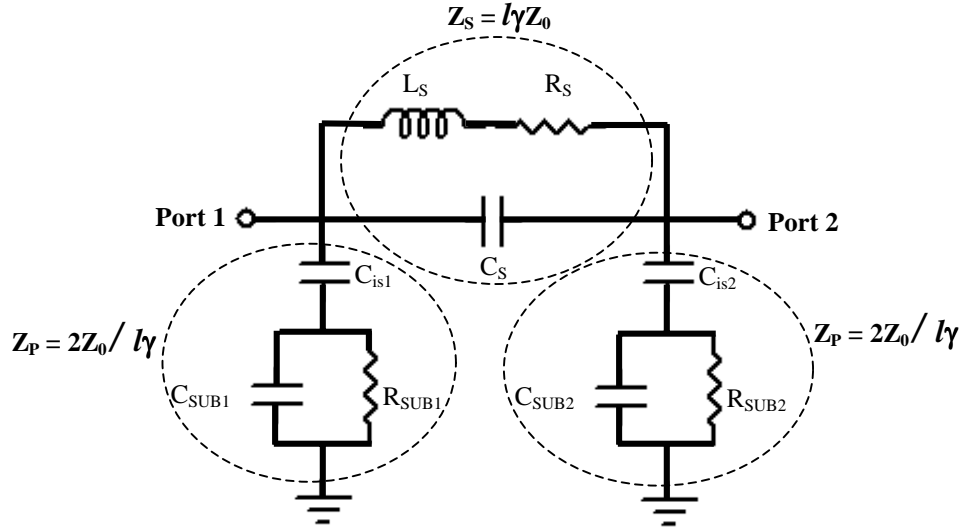


**Figure 3.7: Physical model of a two-port on-chip inductor.**

The model parameter  $C_{is}$  represents coupling-capacitance between the suspended inductor body and the substrate, *i.e.* capacitances of the air-gap and the oxide layer.  $C_{SUB}$  and  $R_{SUB}$  represent capacitance and resistance of the substrate respectively. Inevitably, parasitic resistances and capacitances tag along with the desired inductance in a practical on-chip inductor. Hence, instead of only storing magnetic energy in the inductor, a practical inductor also stores electric energy in fringing capacitances and dissipates heat energy through the parasitic resistances.

Physical model parameters can be evaluated by constructing equations for model admittances and then performing curve fittings of these equations to the measured parameters. At high frequencies, a conductor is subjected to skin effect in which the current flow is limited to a confined area near the conductor surface. The skin depth  $\delta$  or the depth of penetration of current in the conductor is given by

$$\delta = \sqrt{\frac{\rho}{\pi \mu f}} \quad (3.41)$$

where  $\rho$ ,  $\mu$ , and  $f$  represent the resistivity in  $\Omega\cdot\text{m}$ , permeability in H/m, and frequency, respectively. Due to this effect, the resistance of a conductor can be determined by

$$R_s = \frac{\rho l}{w\delta(1 - e^{-t/\delta})} \quad (3.42)$$

where  $l$ ,  $w$ ,  $t$ ,  $\rho$ , and  $\delta$  represent the length, width, thickness, resistivity, and skin depth of the conductor. With an assumption that  $t$  is greater than  $2\delta$ ,  $R_s$  is inversely proportional to  $\delta$ , and  $\delta$  is inversely proportional to  $\sqrt{f}$ . Therefore the series resistance  $R_s$  is proportional to  $\sqrt{f}$  as follows:

$$R_s = R_0 + \lambda R_0 \sqrt{f} \quad (3.43)$$

where  $R_0$  represents DC resistance and  $\lambda$  represents coefficient of frequency dependent resistance component. In curve fitting, the high frequency resistance may not be strictly proportional to the square root of frequency. Therefore, the power of  $f$  is not defined strictly to 0.5 but is allowed to vary in the vicinity of 0.5 in order to give more freedom during curve fitting for frequency dependent of the series resistance. Equation (3.44) represents series resistance as a function of frequency [53].

$$R_s = R_0[1 + \lambda(f^\beta)] \quad (3.44)$$

where  $\lambda$  and  $\beta$  are constants to be obtained from the optimization process. Other model parameters besides  $R_s$  are frequency independent and need to be optimized by curve fitting to the measured  $\pi$ -network parameters  $Y_s = 1/Z_s$  and  $Y_p = 1/Z_p$  computed from the ABCD-parameters in Equations (3.26)-(3.29). In the  $\pi$ -network,  $Y_s$  and  $Y_p$  can be represented by Equations (3.45) and (3.46), respectively.

$$Y_s = \frac{1}{Z_s} = \frac{1}{R_s + j\omega L_s} + j\omega C_s \quad (3.45)$$

$$Y_P = \frac{1}{Z_P} = \frac{1}{\frac{1}{j\omega C_{is}} + \frac{1}{\frac{1}{R_{SUB}} + j\omega C_{SUB}}} \quad (3.46)$$

Estimated values for  $L_S$ ,  $R_0$ ,  $\lambda$ ,  $\beta$ ,  $C_S$ ,  $C_{is}$ ,  $C_{SUB}$  and  $R_{SUB}$  are plugged into Equations (3.43) and (3.44) to evaluate the initial values of  $Y_S$  and  $Y_P$ , and compared to the measured value for  $Y_S$  and  $Y_P$ . The values of model parameters are then adjusted and the process is reiterated until the difference between the model and measured parameters is sufficiently small. MATLAB program “twoportfit.m” in Appendix C performs the optimization process using the nonlinear least-square curve fitting function “lsqcurvefit.m”. Alternatively, the curve fit optimization feature in HSPICE (Avant Corporation) can be used to fit the specified model network parameters to the measured de-embedded S-parameter data [54]. In order to obtain the optimized model parameters, good initial guess and their range for the expected parameters are important. Sometimes choosing initial guess values and their ranges to get a good fit can be difficult and time consuming. To avoid curve-fitting difficulties, a modified physical model for an inductor was proposed by Yue *et al.* [51].

The third modeling method used in this chapter is the simplified physical model of a two-port inductor, which is modified from the physical model by replacing  $C_{is}$ ,  $C_{SUB}$  and  $R_{SUB}$  of the physical model in Figure 3.7 with  $C_P$  and  $R_P$  as shown in Figure 3.8. The shunt admittance of the network consisting of  $C_{is}$ ,  $C_{SUB}$  and  $R_{SUB}$  in Equation (3.46) can be rewritten as

$$Y_P = \frac{1}{R_P} + j\omega C_P = \frac{\omega^2 C_{is}^2 R_{SUB}}{1 + [\omega R_{SUB} (C_{SUB} + C_{is})]^2} + \frac{j\omega C_{is} [1 + \omega^2 (C_{SUB} + C_{is}) C_{SUB} R_{SUB}^2]}{1 + [\omega R_{SUB} (C_{SUB} + C_{is})]^2} \quad (3.47)$$

Comparing the real part of Equation (3.47) to the term  $1/R_P$ , the shunt resistance  $R_P$  is found to be:

$$R_P = \frac{1}{\omega^2 C_{is}^2 R_{SUB}} + R_{SUB} \frac{(C_{SUB} + C_{is})^2}{C_{is}^2} \quad (3.48)$$

The imaginary part of Equation (3.47) is compared to the term  $j\omega C_P$ . Equation (4.49) shows the resulting expression for the shunt capacitor  $C_P$ .

$$C_P = C_{is} \frac{1 + \omega^2 (C_{SUB} + C_{is}) C_{SUB} R_{SUB}^2}{1 + \omega^2 (C_{SUB} + C_{is})^2 R_{SUB}^2} \quad (3.49)$$

For the series branch of the network, the model parameters  $L_S$  and  $R_S$  can be extracted directly from real and imaginary parts of the series impedance  $Z_S$  using Equations (3.50) and (3.51). Since  $C_S$  represents the conductor-conductor fringing capacitance, it can be treated as a frequency independent component. The values of  $C_S$  can be extracted if the self-resonant frequency  $\omega_0$  of the series branch  $Z_S$  and the low frequency  $L_S$  values are known. The resonance frequency of  $Z_S$  is the frequency at which its maximum magnitude occurs. The frequency independent  $C_S$  can be calculated using Equation (3.52).

$$R_S = \text{Re}(Z_S) \quad (3.50)$$

$$L_S = \frac{\text{Im}(Z_S)}{\omega} \quad (3.51)$$

$$C_S = \frac{1}{\omega_0^2 L_{\text{low-freq}}} \quad (3.52)$$

where  $L_{\text{low-freq}}$  represents inductance of  $L_S$  at low frequencies. Extraction of  $R_P$  and  $C_P$  values can be done directly by comparison of real and imaginary parts of the shunt impedance as shown in Equations (3.53) and (3.54).

$$R_P = \frac{1}{\text{Re}\left[\frac{1}{Z_S}\right]} \quad (3.53)$$

$$C_P = -\frac{\text{Im}\left[\frac{1}{Z_S}\right]}{\omega} \quad (3.54)$$

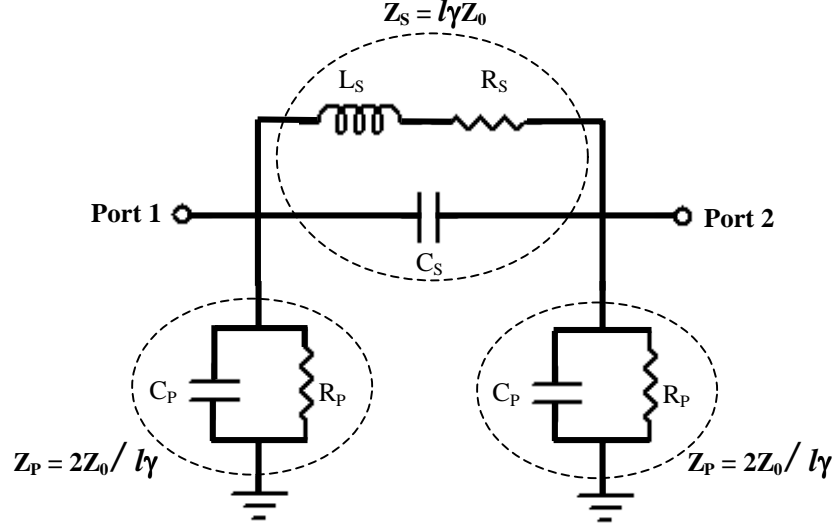


**Figure 3.8: Simplified physical model of a two-port on-chip inductor.**

In the simplified physical model for inductors, the Y-parameters can be directly determined from the  $\pi$ -network series and shunt impedances [47] as shown in Equations (3.55) and (3.56). The S-parameters are then obtained by conversion from the Y-parameters using Equations (3.18)-(3.21).

$$y_{21} = y_{12} = -\frac{1}{Z_S} = -\frac{1}{R_S + j\omega L_S} - j\omega C_S \quad (3.55)$$

$$y_{11} = y_{22} = \frac{1}{Z_S} + \frac{1}{Z_P} = \frac{1}{R_S + j\omega L_S} + j\omega C_S + \frac{1}{R_P} + j\omega C_P \quad (3.56)$$

In order to analyze the Q-factor of the model, the two-port network is transformed to an equivalent one-port network by grounding one of the ports. Figure 3.9 shows the equivalent one-port network transformed from a two-port network. By definition [51], Q-factor of an inductor is

$$Q_{inductor} = 2\pi \left[ \frac{\text{Peak magnetic energy} - \text{Peak electric energy}}{\text{Energy loss per cycle}} \right] \quad (3.57)$$

$$\text{Peak magnetic energy} = \frac{V_0^2 L_S}{2[(\omega L_S)^2 + R_S^2]} \quad (3.58)$$

$$\text{Peak electric energy} = \frac{V_0^2 (C_P + C_S)}{2} \quad (3.59)$$

$$\text{Energy loss per cycle} = \frac{2\pi}{\omega} \cdot \frac{V_0^2}{2} \left[ \frac{1}{R_P} + \frac{R_S}{(\omega L_S)^2 + R_S^2} \right] \quad (3.60)$$

where  $V_0$  represents the peak voltage across the circuit terminal.

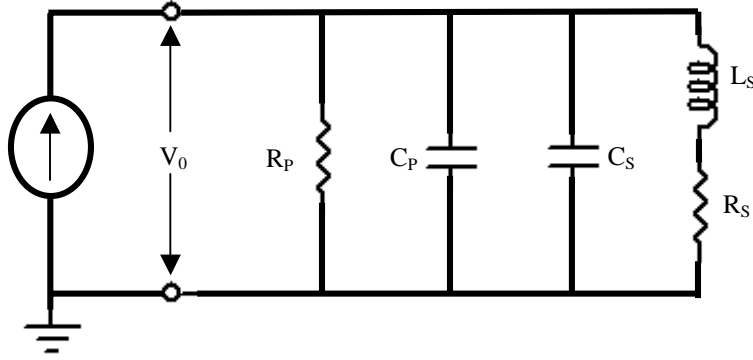


**Figure 3.9: Equivalent one-port model of the simplified two-port physical model of on-chip inductor used in Q-factor analysis.**

By plugging Equations (3.58)-(3.60) into Equation (3.57), the Q-factor of an inductor can be rewritten as

$$\begin{aligned} Q_{inductor} &= \frac{\omega L_S}{R_S} \cdot \frac{1}{1 + \frac{R_S}{R_P} \left[ \left( \frac{\omega L_S}{R_S} \right)^2 + 1 \right]} \cdot \left[ 1 - \frac{R_S^2 (C_S + C_P)}{L_S} - \omega^2 L_S (C_S + C_P) \right] \\ &= \frac{\omega L_S}{R_S} \cdot \text{substrate loss factor} \cdot \text{self - resonance factor} \end{aligned} \quad (3.61)$$

Q-factor of the simplified physical model calculated from Equation (3.61) can be compared with the measured Q-factor determined by the ratio of the imaginary to real parts of the

equivalent one-port input impedance shown in Equation (3.40). The first term of Equation (3.61) represents the Q-factor for an ideal inductor with series resistance. The second and third terms represent the substrate loss factor due to the effects of a conductive substrate and the self-resonance factor, respectively. In the self-resonance factor, the total capacitance of both shunt and series capacitances determines the Q-factor. It can be seen that the substrate loss factor approaches unity when the shunt resistance  $R_P$  approaches infinity. This observation implies that increasing  $R_P$  to infinity will eliminate energy dissipation in the substrate. From Equation (3.48), the shunt resistance  $R_P$  will increase to infinity if the substrate resistance  $R_{SUB}$  is either infinity or zero. According to this observation, using non-conductive material such as glass or high resistivity silicon, or removing the part of silicon substrate underneath the inductor are the ways to increase  $R_{SUB}$  and Q-factor. On the other hand, shielding the substrate with a perforated metal ground plane to decrease  $R_{SUB}$  to zero is another way to improve the Q-factor.

In this chapter, the measurement of on-chip inductor, the probe pads and ground plane parasitic de-embedding, and the modeling methods for the inductor were discussed. In chapters 4 and 5, the measurement and modeling methods developed in this chapter will be used to characterize the suspended arch-like solenoid inductors and the suspended dome-shaped spiral inductors, respectively.

## CHAPTER 4

### ON-CHIP ARCH-LIKE SOLENOID INDUCTORS

Integration of passive inductors with active circuitry is of great interest as described in chapter 1. The most common geometry for passive on-chip inductors is a planar spiral geometry. Conventional three-dimensional solenoid on-chip inductor as shown in Figure 4.1 (a) has two inherent advantages over planar spiral inductors. First, the capacitive coupling between the conductors and the substrate is minimized since only the bottom conductors are directly facing the substrate. Second, the center axis of the solenoid core, along which the strongest high frequency magnetic field exists, is parallel to the substrate. If the substrate has low resistivity, such as an epitaxial silicon substrate used in CMOS chip, the strong magnetic flux that passes into the substrate induces eddy current flow in the substrate and generates heat losses. This eddy current loss can be smaller for a solenoid inductor geometry than for a planar spiral inductor geometry. Even with these advantages, solenoid inductor geometry is not very common in on-chip integration primarily due to inherent fabrication difficulties.

This chapter describes design, fabrication, and characterization of a novel three-dimensional on-chip solenoid inductor with arch-like shape suitable for high frequency application. The on-chip arch-like solenoid inductor was fabricated utilizing fundamental processes developed during this research. These specialized fabrication steps developed in this work include thick photoresist mold-based metallic microstructure electroplating (section 2.1), patterning and deformation of polymeric mesa (section 2.2), conformal electrodeposition and patterning of photoresists (section 2.3), and removal of sacrificial polymeric layers (section 2.4). High frequency measurement method is also taken into account in the design of these inductors



so that inductor physical layout is compatible with the dedicated high frequency measurement setup (chapter 3).

## 4.1 Design

This section describes design issues associated with on-chip passive inductors for high frequency applications and discusses a new design carried out in this work in detail. One of the most important figures of merit of the inductor is its Q-factor. In order to improve the Q-factor of a solenoid inductor, a low resistivity of the conductor and a high resistivity of the substrate are desirable.

One of the major sources contributing to high resistance in a microfabricated conductor is contact resistance that occurs at the interface of two metallic layers. As a result, resistance of a conductor line increases as the number of contact points in the conduction path increases. Conventional solenoid inductors have four contact points per turn as shown in Figure 4.1 (a). In this work, a solenoid inductor, which has an arch-like shape, has been designed. Figure 4.1(b) and 4.1(c) show conceptual drawings of this novel arch-like on-chip air-core solenoid inductors. This three-dimensional solenoid inductor has a flat bottom conductor and an arch-like top conductor. The top and bottom conductors are connected through via pads. This newly designed inductor has only two contact points per turn as depicted in Figure 4.1 (b). By choosing low resistivity material such as copper as a conductor, the series resistance can now be significantly decreased.

Excluding substrate losses and self-resonant factors, degradation of inductor Q is only due to its series resistance. Copper has resistivity  $1.66 \mu\Omega\text{-cm}$  or about 60 percent of that of aluminum ( $2.65 \mu\Omega\text{-cm}$ ) [55]. By simply changing conductor material from aluminum to copper increases the Q-factor of the inductor a factor of 1.67 as seen from Equation (4.1).

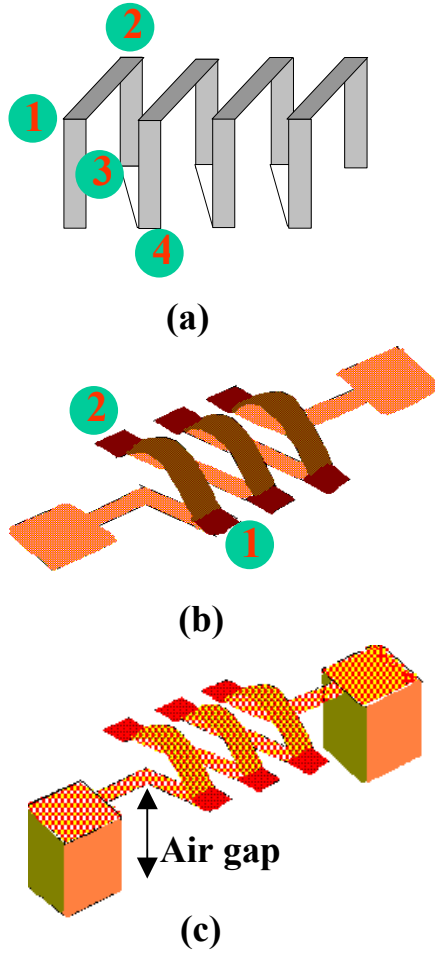


**Figure 4.1: Three-dimensional on-chip air-core solenoid inductors. (a) Conventional three-dimensional inductor design. (b) Non-suspended arch-like solenoid inductor. (c) Suspended arch-like solenoid inductor.**

$$Q_{Cu} = \frac{\omega L}{R_{Cu}} = \frac{\omega L}{0.6 R_{Al}} \approx 1.67 Q_{Al} \quad (4.1)$$

A low resistivity substrate is another factor that significantly limits the Q-factor of an inductor. As discussed in chapter 3, using high resistivity material as a substrate, removing the substrate bulk beneath the inductor, or suspending the inductor above the substrate with surface micromachining reduces this problem. In this work, surface micromachining technique is utilized to raise the inductor's body above the substrate with metallic spacers at both ends as shown in

Figure 4.1 (c) to reduce substrate losses. Materials inside an inductor core can also degrade inductor performance. Lee *et al.* [36] filled the air-core solenoid inductor with a polymer and found that self-resonant frequency decreased by approximately 7%.

Sonnet EM (Sonnet Software) electromagnetic simulation tool has been used to simulate suspended solenoid inductors with air-gap heights varying from zero to 400  $\mu\text{m}$  in order to find a relationship between the height of the air-gap and the inductor Q-factor. The Sonnet EM software version used in this work cannot accommodate full three-dimensional geometry. Due to the software limitations, inductors are simulated with a conventional flat conductor as shown in Figure 4.2 instead of a true three-dimensional arch-like shape for the top conductors.

The simulated Q-factors of a 2-turn inductor with various air-gap heights are shown in Figure 4.3. It can be seen that the non-suspended inductor has lower Q than suspended inductor. Figure 4.4 shows the equivalent circuit models of the inductor at peak Q-frequencies for two different air-gap values. Table 4.1 shows the model parameters given by Sonnet EM simulations.

From Figure 4.3 and Table 4.1, increasing the air-gap height from 30  $\mu\text{m}$  up to 400  $\mu\text{m}$  does not improve Q-factors or the self-resonant frequency significantly. Based on these simulation results, air-gap of 30  $\mu\text{m}$  will be used in the fabrication of the suspended arch-like solenoid inductors.

In order to find approximate inductance values in designs of conventional solenoid inductors, a current sheet inductance approximation [34] or a Wheeler's inductance formula for a circular solenoid [56] are generally used as given by Equations (4.2) and (4.3), respectively.

Current sheet inductance approximation:

$$L_{\text{Current sheet}} = \frac{N^2 A \mu}{l} \quad (4.2)$$

Wheeler's formula (finite length circular solenoid):

$$L_{\text{Wheeler}} = \frac{r^2 N^2}{9r + 10l}, \quad (4.3)$$

where  $N$ ,  $A$ ,  $\mu$ ,  $l$ , and  $r$  represent the number of turns, cross-sectional area of the core, permeability of the core, core length and core radius, respectively. The Wheeler's formula assumes that the solenoid core has circular cross-section. Inductances of a 2-turn inductor with  $N = 2$ ,  $A = 2250 \mu\text{m}^2$ ,  $\mu = 4\pi \times 10^{-7} \text{ H/m}$  and  $l = 135 \mu\text{m}$  used in Sonnet EM simulation are calculated using Equations (4.2) and (4.3).

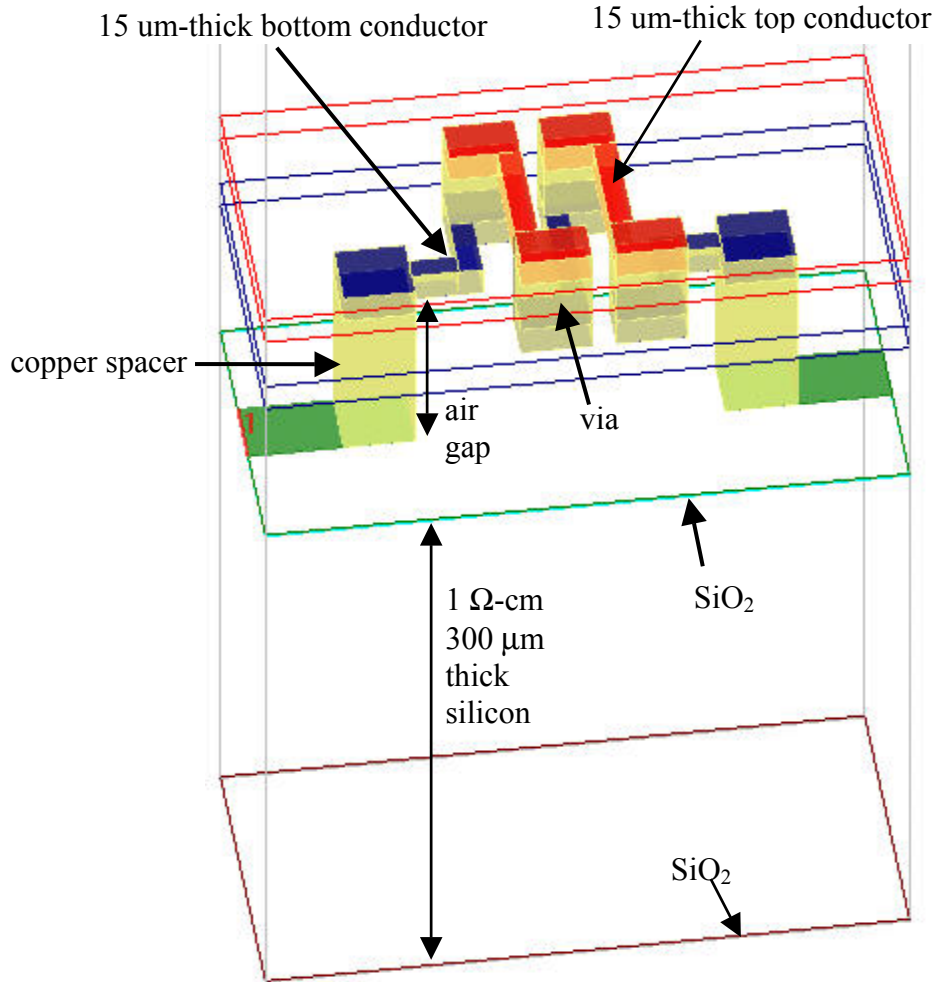


**Figure 4.2: Suspended solenoid inductor used in Sonnet EM simulation.**

The current sheet inductance approximation and the Wheeler's formula give inductance values of 0.083 nH and 0.071 nH, respectively, compared to 0.28 nH obtained from the Sonnet EM simulation. The inductance obtained from Sonnet simulation includes self-inductances of extra straight wires such as the substrate spacers, suspending beams, and via pads. The values of these extra self-inductances are given by [57]:

$$L_{Straight\ wire} = 0.002l \left[ \ln \left( \frac{2l}{w+t} \right) + 0.50049 + \left( \frac{w+t}{3l} \right) \right], \quad (4.4)$$

where  $l$ ,  $w$ , and  $t$  represent the length, width, and thickness of the wire, respectively. The total extra self-inductance of the straight wires is 0.127 nH. Subtracting this extra self-inductance from the values obtained from Sonnet simulation gives corrected inductance of 0.153 nH.

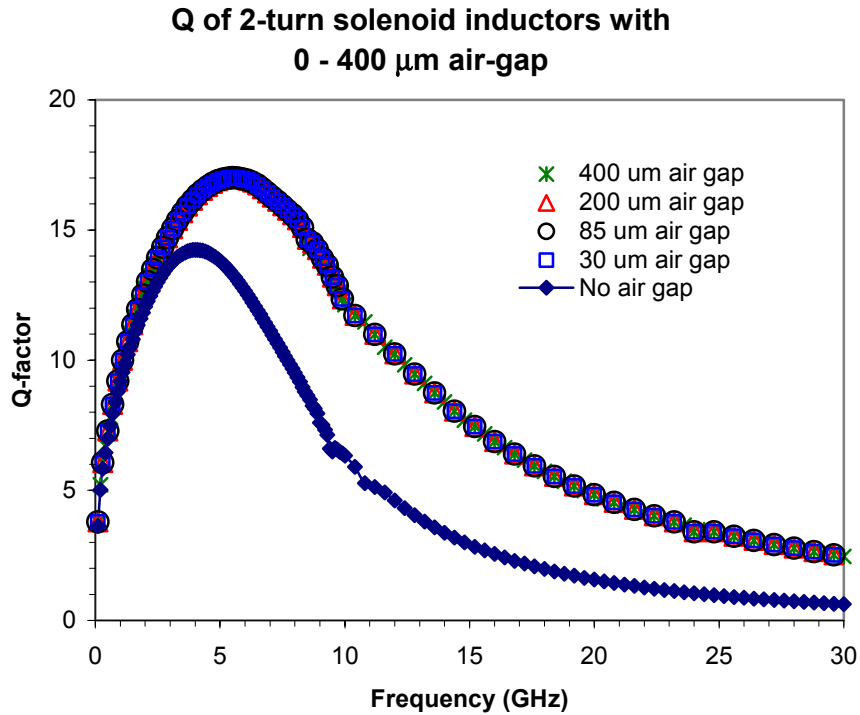


**Figure 4.3: Sonnet EM simulated Q-factors of a 2-turn copper inductor with various air-gap heights.**

**Table 4.1 Model parameters of 2-turn solenoid inductors simulated by Sonnet EM.**

Air-gap	Peak Q	Peak-Q freq. (GHz)	$L_S$ (nH)	$R_S$ ( $\Omega$ )	$C_P$ (fF)	Self-resonant freq. (GHz)
None	14.2	4.3	0.2816	0.2516	86.10	33.2
30 $\mu\text{m}$	17.0	5.7	0.2764	0.2838	28.03	69.0
85 $\mu\text{m}$	17.0	5.7	0.2764	0.2844	28.53	69.0
200 $\mu\text{m}$	17.0	5.7	0.2764	0.2831	28.53	69.0
400 $\mu\text{m}$	17.0	5.7	0.2764	0.2838	29.95	69.0

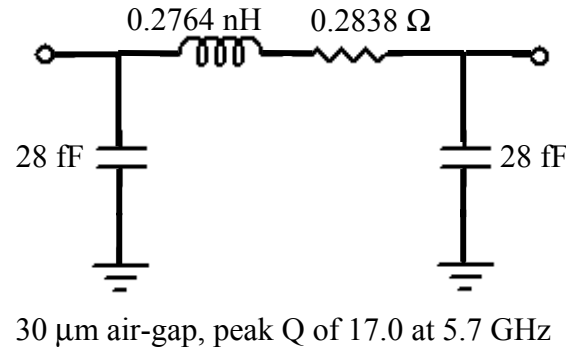
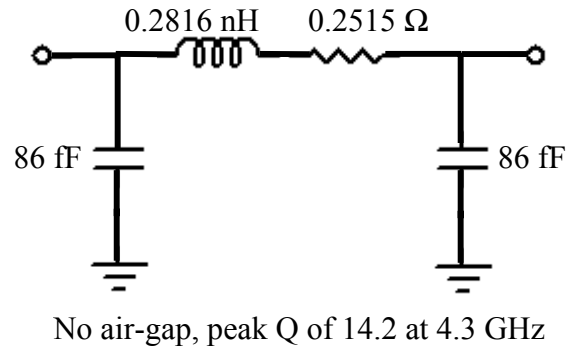


**Figure 4.4 Sonnet EM simulated equivalent circuit models of 2-turn solenoid inductors with no air-gap and 30  $\mu\text{m}$  high air-gap at their peak-Q frequencies.**

From design considerations and simulation results described in this subsection, suspended arch-like solenoid copper inductors are fabricated with the following dimensions. The copper conductors are 25  $\mu\text{m}$  wide and 15  $\mu\text{m}$  thick. The vias are of 40  $\mu\text{m}$  by 40  $\mu\text{m}$  in area. The air core is of 75  $\mu\text{m}$  wide, 80  $\mu\text{m}$  long per turn, and 30  $\mu\text{m}$  high at the arch top. The die areas

occupied by 2-turn, 3-turn, and 5-turn inductors are  $0.012 \text{ mm}^2$ ,  $0.018 \text{ mm}^2$ , and  $0.030 \text{ mm}^2$ , respectively. The inductors will be suspended  $30 \text{ }\mu\text{m}$  above the silicon substrate. Figure 4.5 shows a schematic diagram of the three-dimensional model of 2-turn suspended arch-like solenoid inductor in this configuration.

## 4.2 Fabrication

Three-dimensional arch-like air-core suspended solenoid on-chip inductors as per design described in section 4.1 are fabricated using specific processes developed as described in chapter 2. This section describes fabrication of such inductors in detail.

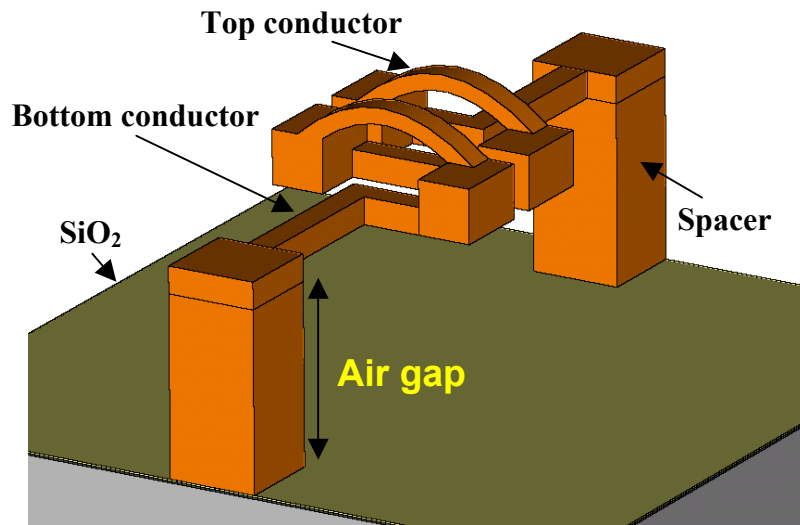


**Figure 4.5: A drawing of a suspended 2-turn air-core arch-like solenoid on-chip inductor.**

A brief fabrication sequence of a three-dimensional suspended air-core arch-like solenoid inductor is shown in Figure 4.6. The fabrication sequence is started with the deposition of a 10 nm Cr / 150 nm Cu / 10 nm Cr plating base layer on an oxidized silicon wafer. A layer of  $30 \text{ }\mu\text{m}$  thick SU-8 2025 is spin-coated on the substrate and the sample is soft baked at  $65 \text{ }^\circ\text{C}$  for 2 minutes and then at  $95 \text{ }^\circ\text{C}$  for 6 minutes in an oven. The sample is exposed by UV light through

a photomask for substrate spacer posts, probe pads and ground plane patterns using a dose of 236 mJ/cm<sup>2</sup>. It is post-exposure baked with the same conditions as those for the soft baking. Then, the SU-8 film was developed in the Nano SU-8 developer for 1.5 minutes.

Prior to electroplating of copper spacer, invisible SU-8 residues are removed by etching in 100 % O<sub>2</sub> plasma RIE with a gas pressure of 100 mTorr and incident RF power of 100 W for 6 minutes. The spacer molds are filled to the top by copper electroplating as shown in Figure 4.6 (a). The next layer of plating base is coated over the wafer and a layer of 30 µm thick SU-8 is spin-coated and patterned on top of the copper spacers to be used as an electroplating mold for bottom conductors. This mold is then cleaned in O<sub>2</sub> plasma RIE and it is filled to the top by copper electroplating as shown in Figure 4.6 (b).

A 30 µm thick SJR5740 layer is spin-coated and patterned to create 70 µm wide and 500 µm long rectangular mesa structure as shown in Figure 4.6 (c). This mesa is significantly deformed to obtain an arch-like cross-sectional profile sacrificial photoresist core for fabricating the top conductors. The deformed mesa core is coated with a 10 nm Cr / 300 nm Cu plating base. A 15 µm thick EAGLE2100 ED photoresist layer is conformally electroplated on the sacrificial polymeric core as shown in Figure 4.6 (d). This conformal photoresist layer is then patterned to obtain a conformal photoresist mold for formation of the arch-like top conductors. This photoresist mold is cleaned by O<sub>2</sub> plasma RIE and filled to the top by copper electroplating as shown in Figure 4.6 (e).

Finally, all sacrificial polymeric materials are etched away by O<sub>2</sub> plasma RIE with 10 % CF<sub>4</sub>, and all plating base are removed by wet etching as shown in Figure 4.6 (f). Here, a mixture of 10 ml H<sub>2</sub>SO<sub>4</sub> : 10 ml H<sub>2</sub>O<sub>2</sub> : 200 ml H<sub>2</sub>O is used to etch copper and 40 g K<sub>3</sub>Fe(CN)<sub>6</sub> : 40 g NaOH : 200 ml H<sub>2</sub>O is used to etch chromium. The removal of Cu plating base sacrificial layers



are done without protection for copper conductors since the plating base layers are much thinner than copper conductors. This causes the resulting copper conductors to be thinner than the designed thickness. Figure 4.7 - 4.10 are photomicrographs showing plan views of a 5-turn inductor during fabrication.

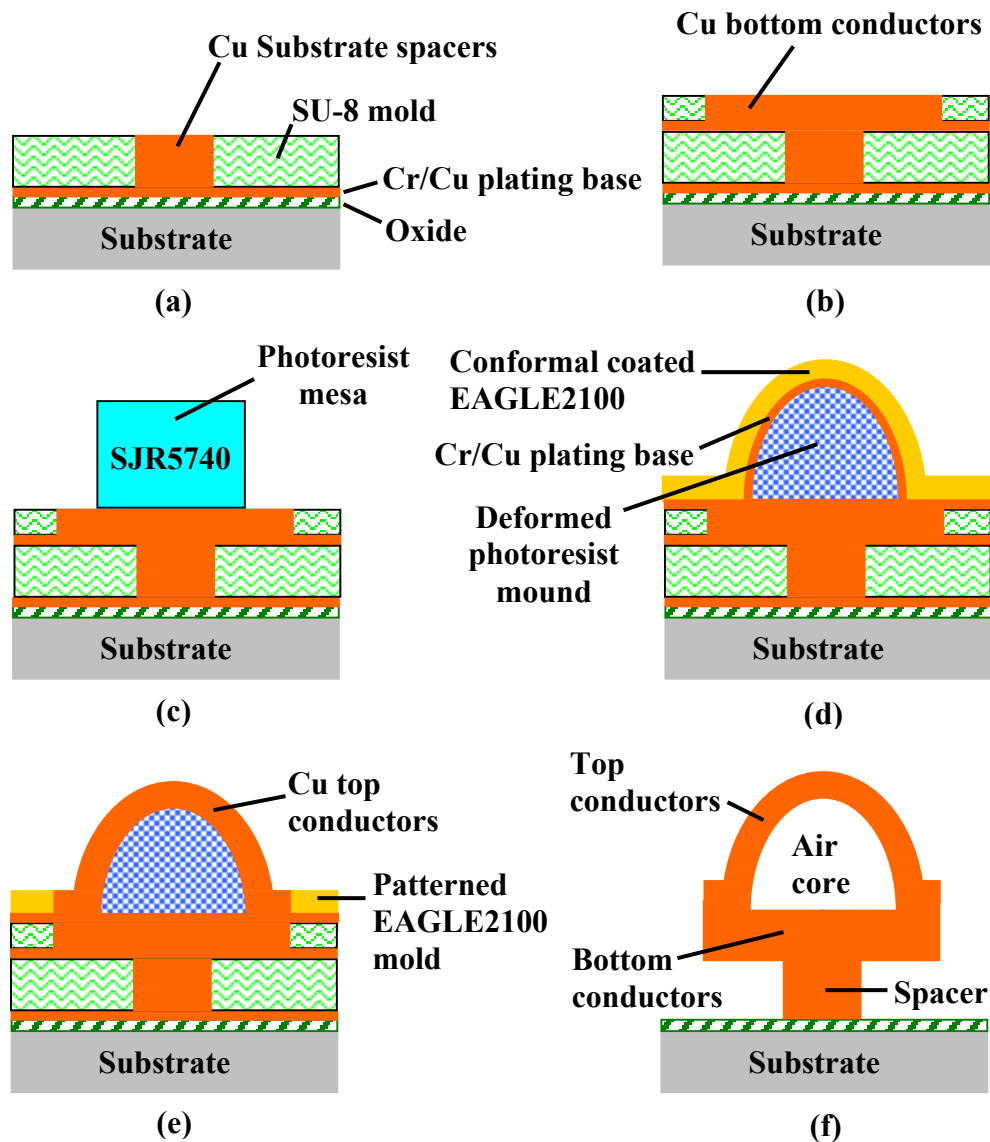
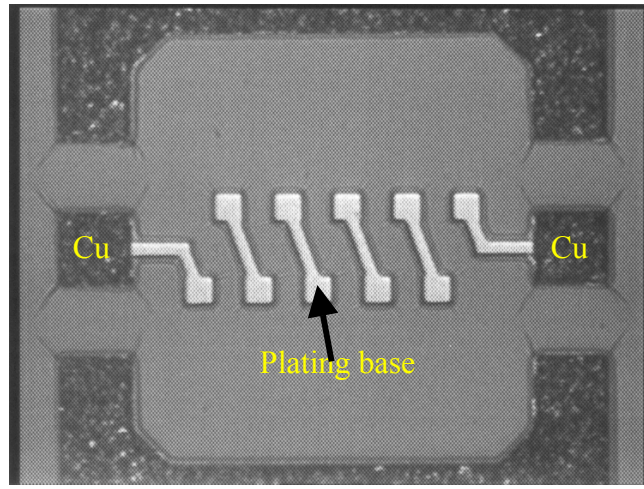
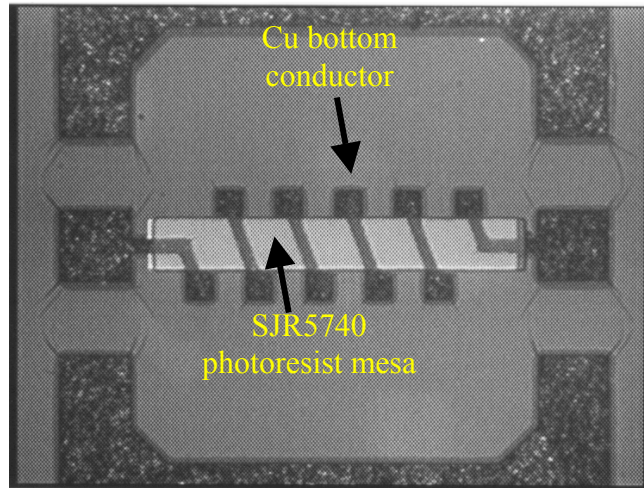


**Figure 4.6: Fabrication sequence of a three-dimensional suspended air-core arch-like solenoid on-chip inductor.**

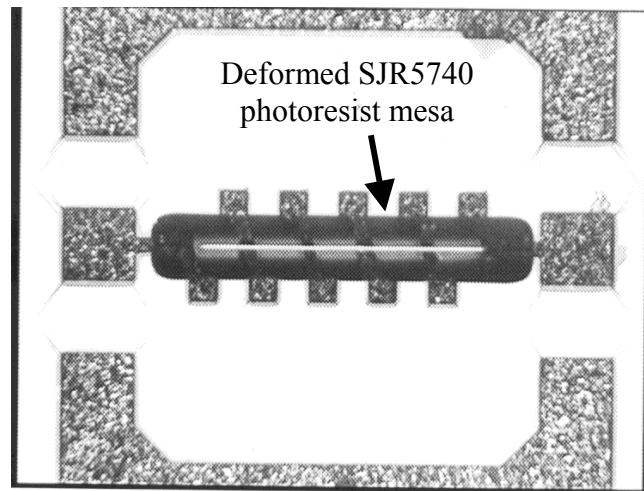


(a)

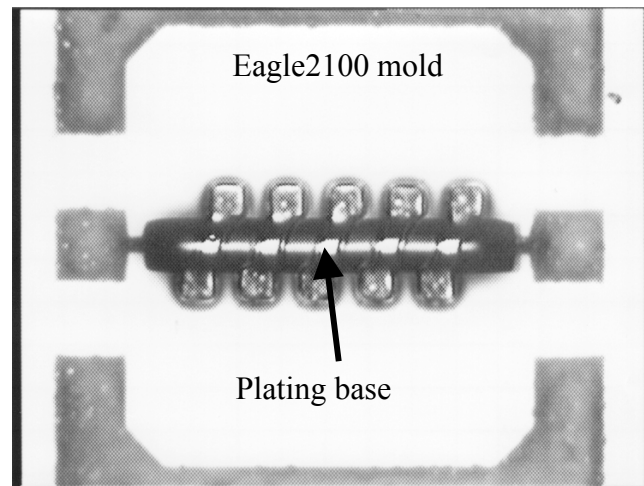


(b)

**Figure 4.7: Photomicrographs of a 5-turn arch-like solenoid on-chip inductor under fabrication: (a) after copper spacer electroplating and bottom conductor photo resist mold development, (b) after bottom conductor electroplating and photo resist mesa development.**

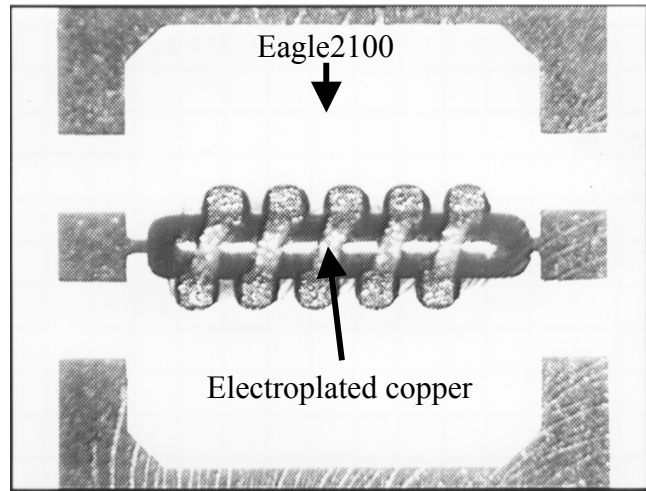


(a)

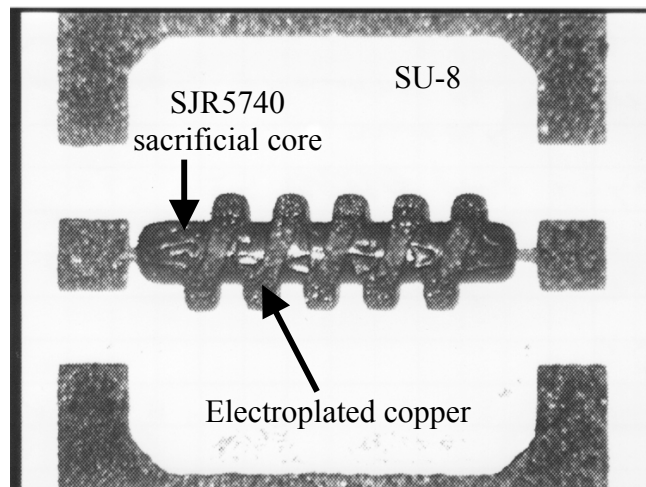


(b)

**Figure 4.8: Photomicrographs of a 5-turn arch-like solenoid on-chip inductor under fabrication: after deformation of photoresist mesa, (b) after development of top conductor EAGLE2100 mold.**

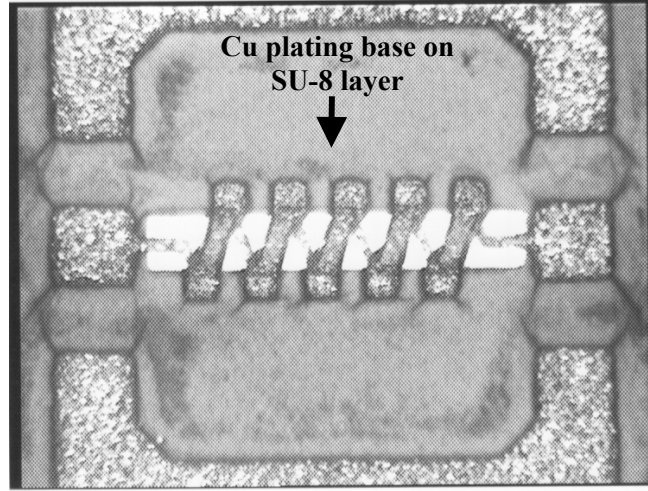


(a)

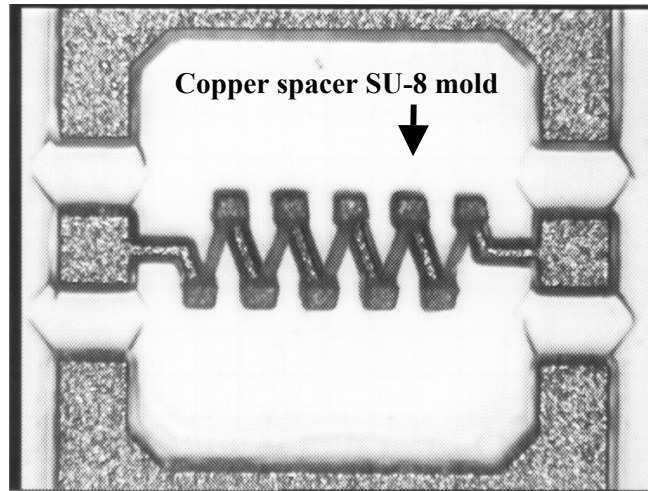


(b)

**Figure 4.9: Photomicrographs of a 5-turn arch-like solenoid on-chip inductor under fabrication: (a) after copper electroplating of top conductors and (b) Eagle2100 mold removal.**



(a)



(b)

**Figure 4.10: Photomicrographs of a 5-turn arch-like solenoid on-chip inductor under fabrication: (a) after removal of sacrificial SJR5740 core, (b) after removal of bottom conductor SU-8 mold.**

Figure 4.11 (a), (b) and (c) show the resulted 2-turn and 3-turn suspended three-dimensional arch-like air-core inductors with 30  $\mu\text{m}$  air gap, 75  $\mu\text{m}$  core width, 30  $\mu\text{m}$  bottom conductors thickness, and 15  $\mu\text{m}$  top conductors thickness. The conductor width is 25  $\mu\text{m}$  and

the contact vias are  $30\ \mu\text{m}$  by  $45\ \mu\text{m}$  in size. Thin SU-8 residues remaining underneath the bottom conductors can be seen in these figures. Figure 4.11 (d) shows a copper arch-like inductor with over-electroplated top conductors in order to compensate for copper bulk loss during several batches of thin copper plating base removals from under every photoresist layer.

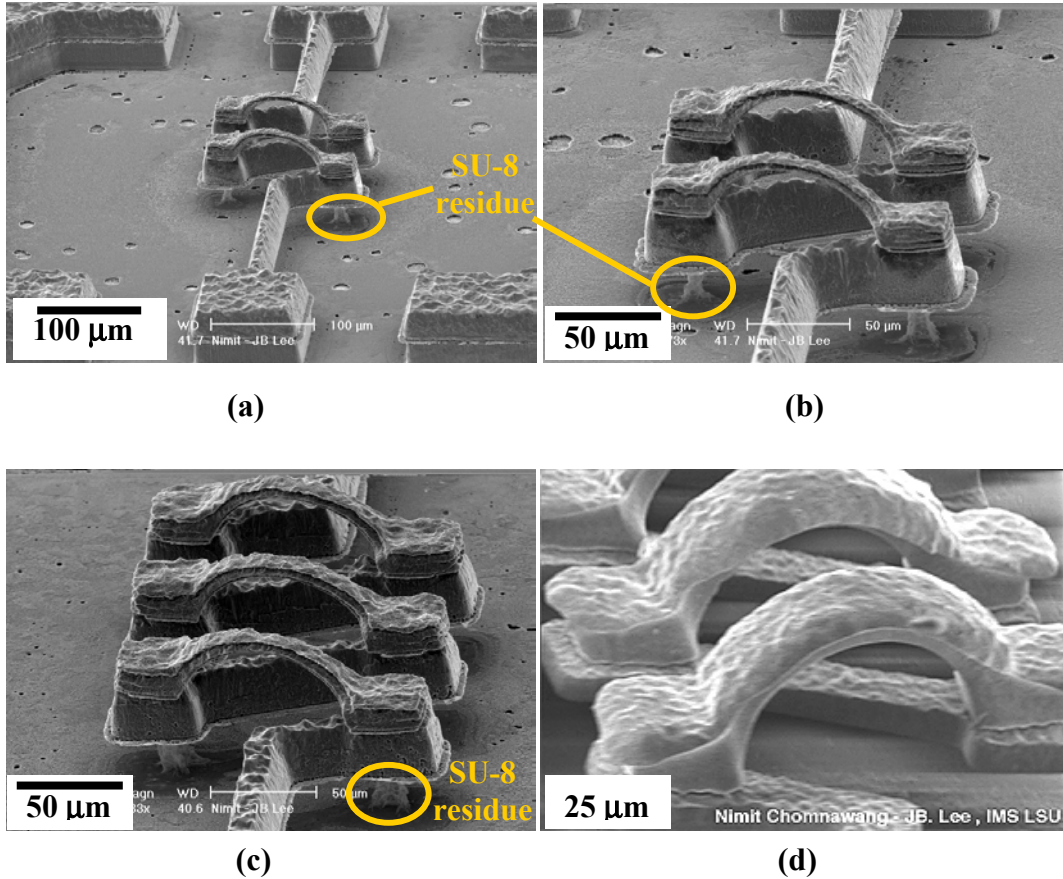


**Figure 4.11: SEM photomicrographs of copper arch-like inductors suspended in air  $30\ \mu\text{m}$  above the substrate: (a) 2-turn, (b) 2-turn , (c) 3-turn, and (d) close view of an inductor with over-electroplated top conductors.**

### 4.3 Measurements, Modeling Results, and Discussions

High frequency measurement procedures described in chapter 3 are used to characterize fabricated 2-turn, 3-turn, and 5-turn arch-like solenoid inductors. Probe pads and ground plane with inductor (DUT), and probe pads and ground plane without inductor (PAD) are measured

with an Agilent 8510C automatic vector network analyzer from 500 MHz to 26 GHz using a pair of G-S-G (ground-signal-ground) type on-wafer 40A-GSG-200-P microprobes. Before measurements, the equipment is calibrated with a CS-5 standard impedance substrate by open-short-load-thru method.

The parasitic effect of the probe pads and the ground plane is de-embedded from the measured data by converting S-parameters of the DUT and the PAD into Y-parameters and subtracting Y-parameters of the PAD from those of the DUT. Figures 4.12 - 4.14 show Smith charts of S-parameter of the DUT, the PAD, and the de-embedded DUT. From the Smith charts, it can be noticed that the trace of  $S_{11}$  is almost identical to  $S_{22}$ , and  $S_{21}$  is almost identical to  $S_{12}$ . This implies a good symmetry between port 1 and port 2.

In the Smith chart for S-parameters of the PAD, the reflection coefficients  $S_{11}$  and  $S_{22}$  are in the capacitive region (negative reactance). Therefore, the dominant parasitic effect of the probe pads and the ground plane is due to their stray capacitance to the substrate. In addition, the curly tails at high frequency regions of  $S_{11}$  and  $S_{22}$  in the Smith chart for PAD (pointed by an arrow inside a circle in Figure 4.12 (b) suggests that the probe pads and ground plane dummy patterns create parasitic capacitance similar to the one observed in a tunable capacitor fabricated on a low-resistivity silicon substrate [6].

In this work, three modeling methods are used to characterize arch-like on-chip solenoid inductors. They are the traditional  $\pi$ -network modeling, the physical  $\pi$ -network modeling, and the simplified physical  $\pi$ -network modeling. The traditional  $\pi$ -network model translates two-port ABCD-parameters into a particular circuit representation with a  $\pi$ -network at each frequency. The model hence specifies circuit valid at a single frequency. In other words, this is a narrow band model.



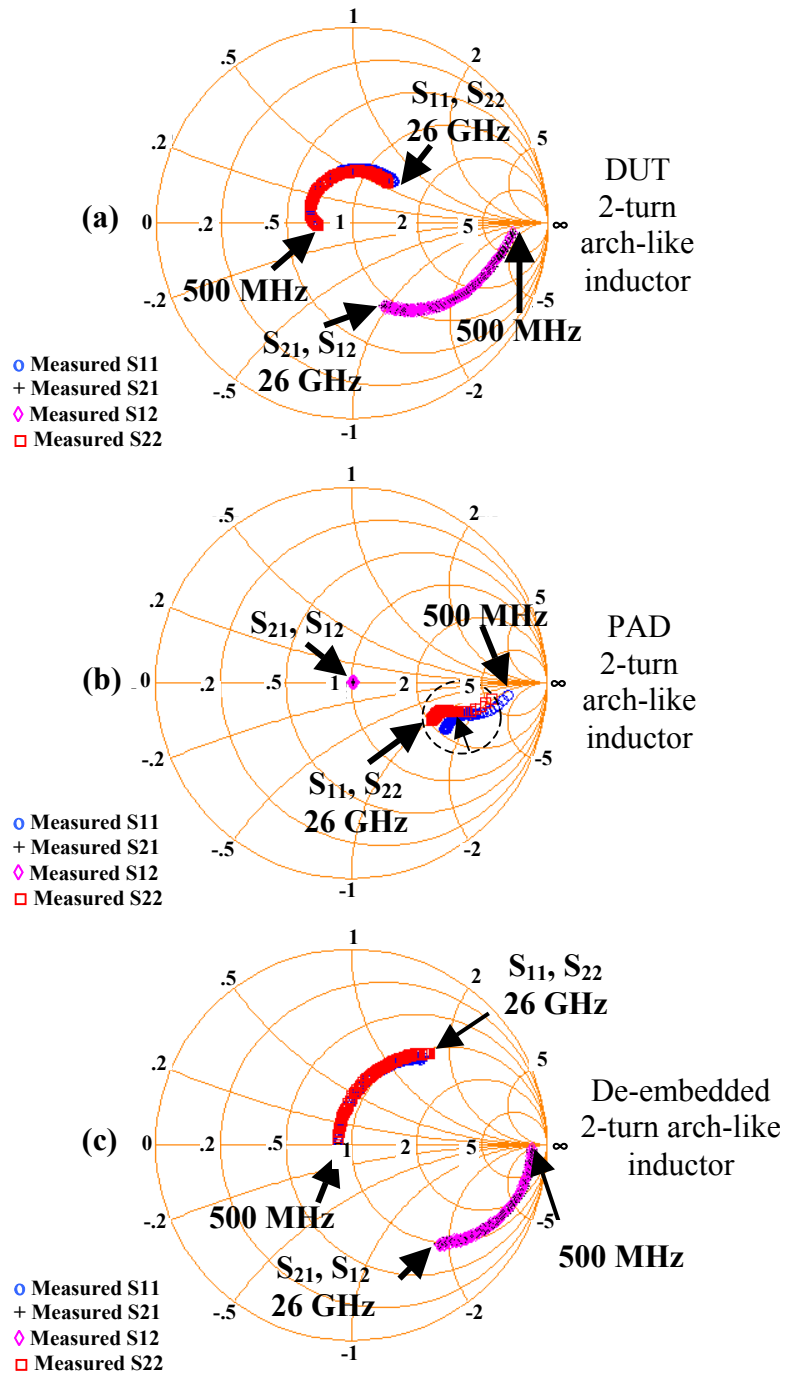


**Figure 4.12: Measured S-parameters of a 2-turn arch-like solenoid inductor: (a) DUT, (b) PAD, and (c) parasitic de-embedded.**



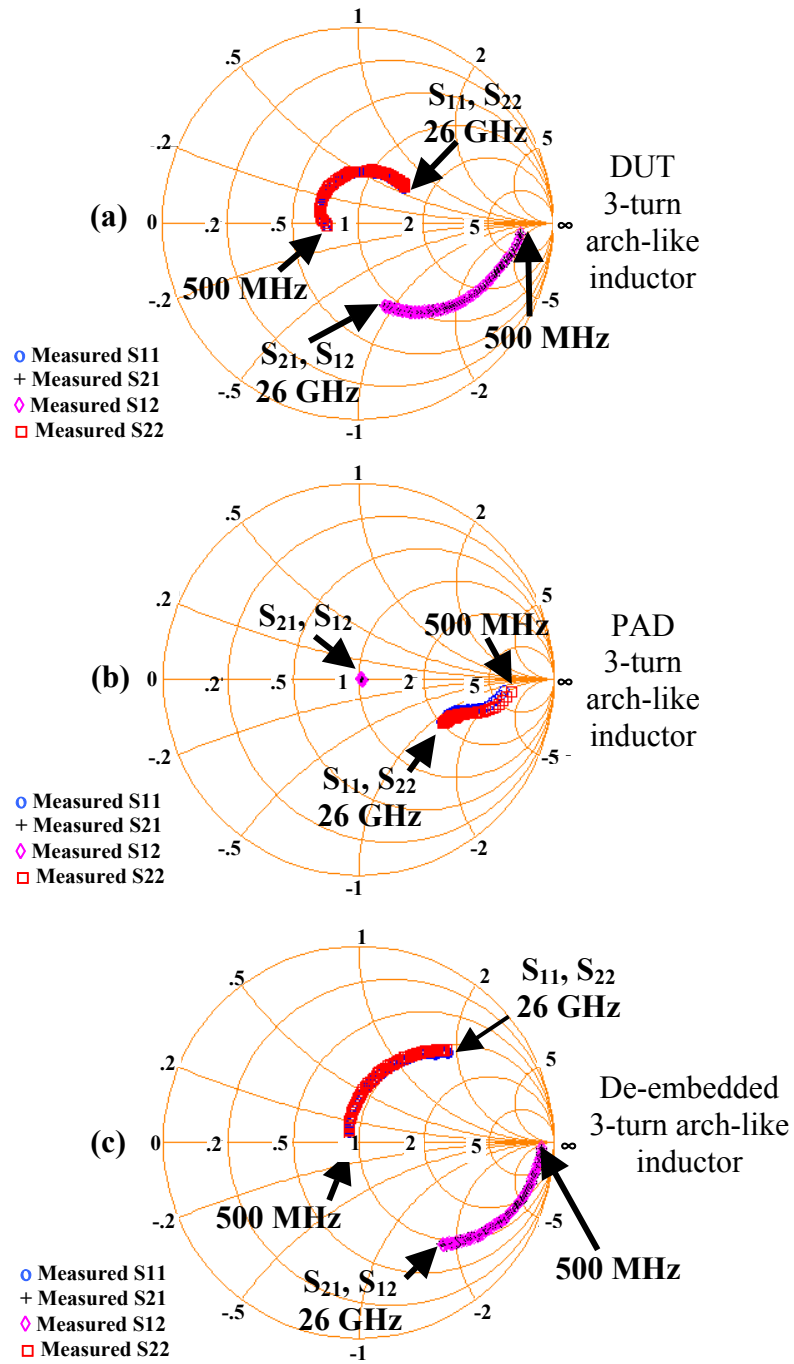


**Figure 4.13: Measured S-parameters of a 3-turn arch-like solenoid inductor: (a) DUT, (b) PAD, and (c) parasitic de-embedded.**

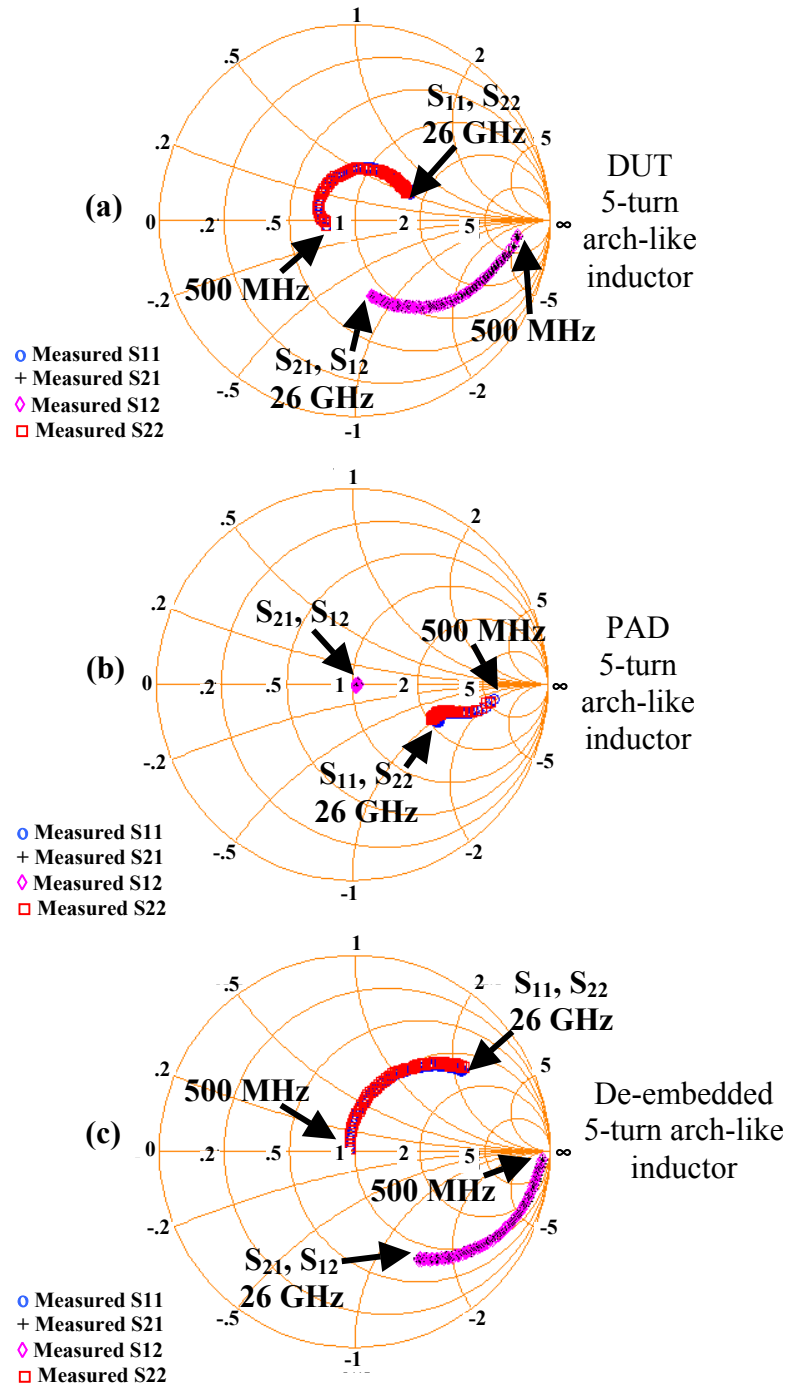


**Figure 4.14: Measured S-parameters of a 5-turn arch-like solenoid inductor: (a) DUT, (b) PAD, and (c) parasitic de-embedded.**

The drawback of traditional  $\pi$ -network modeling method is that the model parameters obtained do not represent physical elements of the inductor. The models tend to include stray capacitances in the inductance value. Furthermore, the models often give negative resistances at high frequencies. Similar effect of negative resistance occurs in Wye-to-Delta conversions of two-port networks containing large capacitances [58].

Figures 4.15 and 4.16 show Q-factors and model parameters of 2-turn, 3-turn, and 5-turn arch-like solenoid inductors as a function of frequency. The traditional models of 2-turn, 3-turn, and 5-turn arch-like solenoid inductors give series inductance of 0.61 nH, 0.66 nH, and 0.79 nH, respectively. These inductance values decrease slowly as the frequency increases. The series resistances are near 1  $\Omega$  and become negative at frequencies above 15 GHz. For the shunt capacitance-resistance, the capacitance values decrease exponentially with frequency and become less than 0.5 pF at frequencies above 5 GHz while the resistance values are in a range of 300  $\Omega$  to 1 k $\Omega$ .

Maximum Q-factors of arch-like solenoid inductors occur approximately in between 4 GHz to 7 GHz. The model parameters at peak-Q frequencies are summarized in Table 4.2, where the self-resonance frequencies are approximated by the inductance  $L_S$  at low frequency and capacitance  $C_P$  at high frequency. Many of these model parameters have good agreements with those obtained from Sonnet EM simulations. For example, the peak Q-factor of the 2-turn arch-like inductor is 17.66 at 4.71 GHz in this model while it is 17.0 at 4.3 GHz in the Sonnet model. Approximate self-resonant frequency is 34.54 GHz in this model while it is 33.2 GHz in the Sonnet model. Figure 4.17 shows traditional  $\pi$ -models for 2-turn, 3-turn, and 5-turn arch-like solenoid inductors at their peak-Q frequencies. For the series inductance and resistance, the

traditional  $\pi$ -model gives approximately twice the values than those obtained from Sonnet simulation.

Physical model curve-fitting is the second modeling method used. Physical models of the 2-turn, 3-turn, and 5-turn arch-like suspended solenoid inductors are obtained by curve fitting between guess values for  $\pi$ -model parameters and measured values. The MATLAB program “indmodel.m” as shown in Appendix C is used to perform curve fitting. The resulting physical model parameters are shown in Table 4.3.

Self-resonant frequency of an inductor can be determined by the frequency at which the magnitude of its  $S_{21}$  is minimum [53]. The self-resonant frequencies of these suspended arch-like inductors are beyond 26 GHz since the input  $S_{21}$  does not have a minima below this frequency as shown in Figure 4.18.

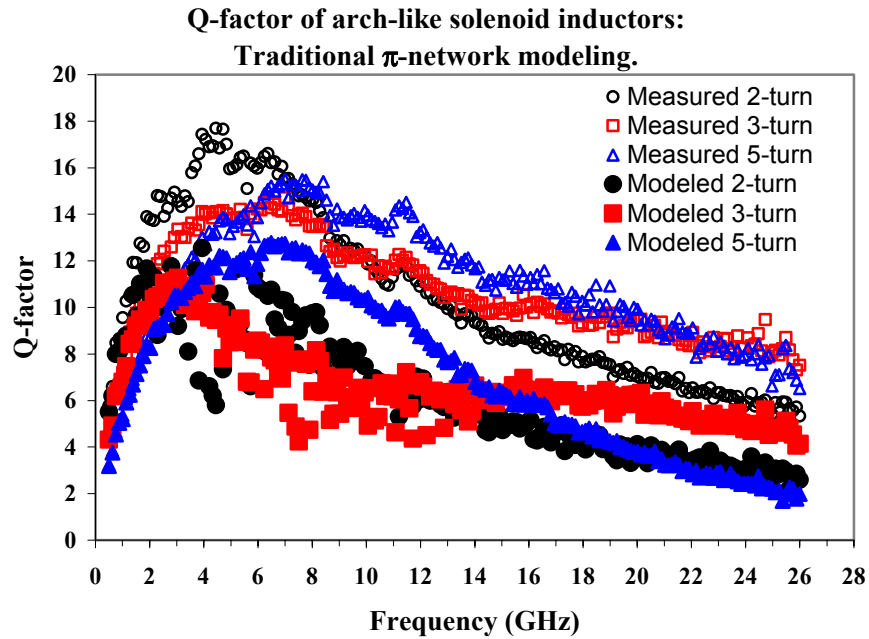


**Figure 4.15: Measured Q-factors of arch-like solenoid inductors and Q-factors obtained from the traditional  $\pi$ -network models.**

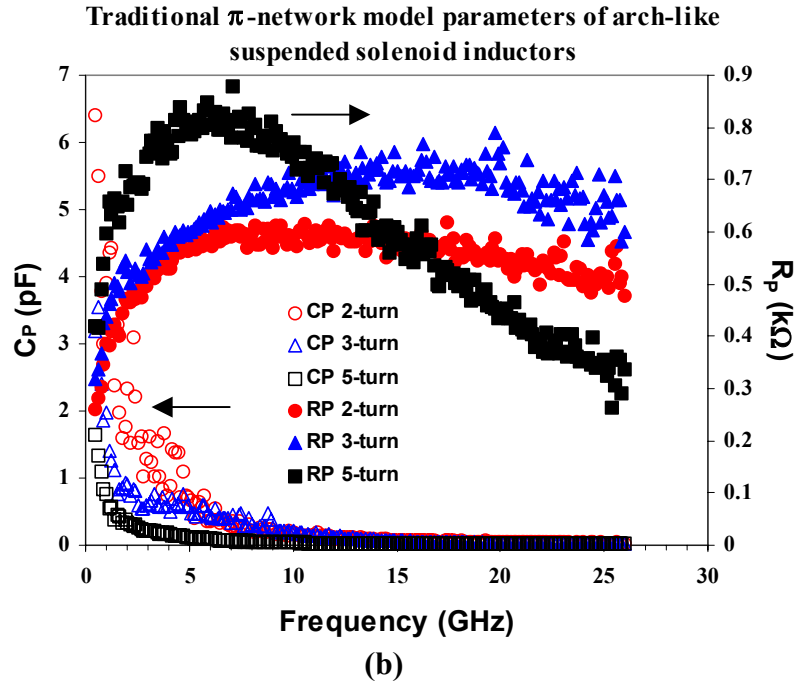
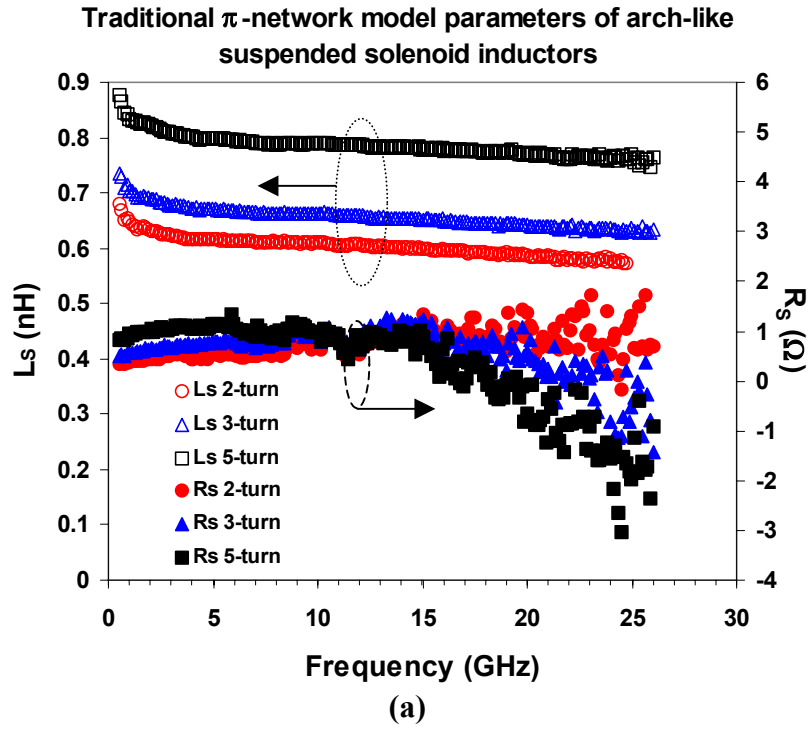


**Figure 4.16: Traditional  $\pi$ -network model parameters of arch-like solenoid inductors: (a)  $L_s$  and  $R_s$ , and (b)  $C_p$  and  $R_p$ .**

**Table 4.2: Parameters of 2-turn, 3-turn, and 5-turn arch-like solenoid inductors for the traditional  $\pi$ -models.**

No. of turns	Peak Q	$f_{Q\max}$ (GHz)	$L_S$ (nH)	$R_S$ ( $\Omega$ )	$C_P$ (pF)	$R_P$ (k $\Omega$ )	$f_{\text{Self-resonant}}$ (GHz)
2	17.66	4.71	0.616	0.449	1.080	0.570	34.54
3	14.71	6.36	0.666	0.682	0.400	0.628	41.29
5	15.50	7.00	0.791	0.903	0.067	0.781	46.23

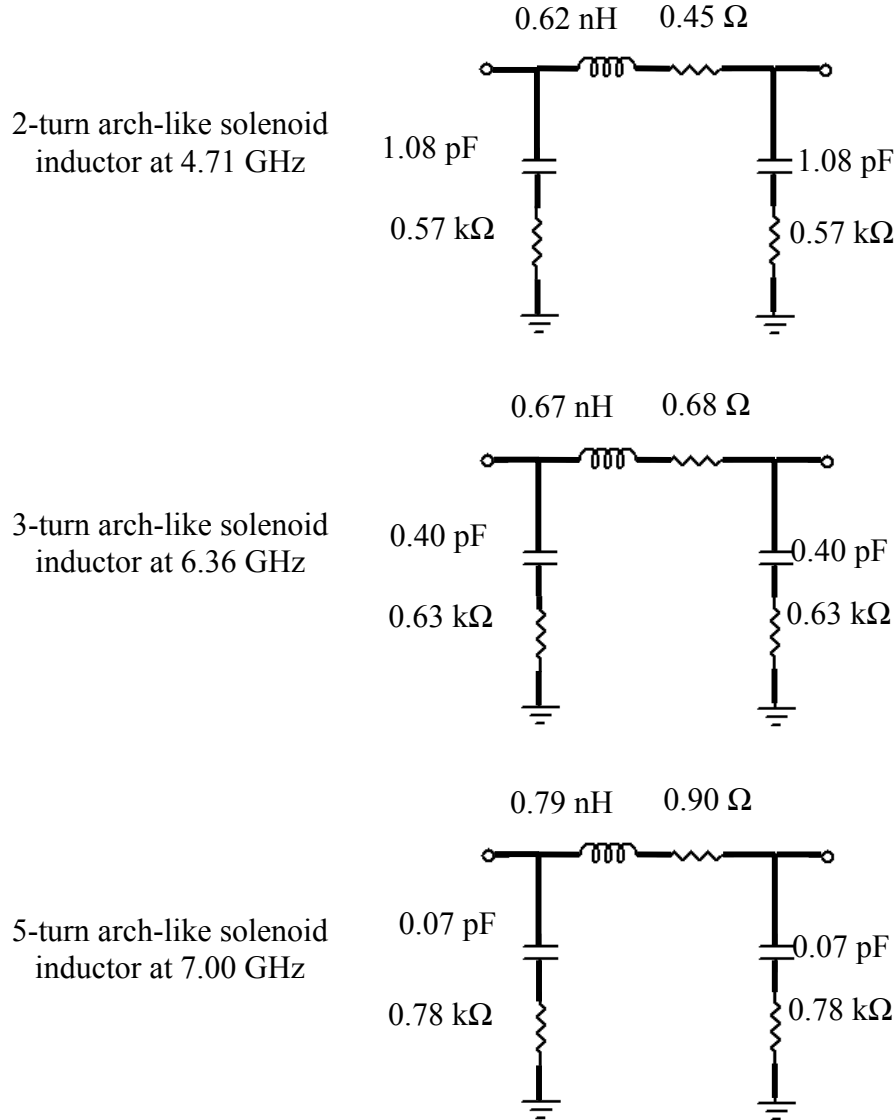


**Figure 4.17: Simple  $\pi$ -models of 2-turn, 3-turn, and 5-turn arch-like solenoid inductors at their peak-Q frequencies.**

**Table 4.3: Physical model parameters of arch-like suspended solenoid inductors obtained from a curve-fitting modeling method.**

Physical model parameters	2-turn	3-turn	5-turn
$L_S$ (nH)	0.623	0.680	0.801
$R_0$ (m $\Omega$ )	63	71	251
$R_S$ ( $\Omega$ )	$R_0+0.084f^{0.238}$	$R_0+0.040f^{0.276}$	$R_0+0.0023f^{0.364}$
$C_S$ (F)	$3.911 \times 10^{-26}$	$2.7 \times 10^{-28}$	$5.78 \times 10^{-27}$
$C_{is1}$ (pF)	0.472	0.337	0.434
$C_{is2}$ (pF)	0.645	0.395	0.395
$R_{SUB1}$ (k $\Omega$ )	0.771	0.734	0.691
$R_{SUB2}$ (k $\Omega$ )	0.966	0.331	0.728
$C_{SUB1}$ (fF)	2.85	4.10	9.04
$C_{SUB2}$ (fF)	4.02	1.93	8.10
Peak Q	22.15	20.45	20.01
$f_{Qmax}$ (GHz)	6.36	8.40	8.40
Self-resonant frequency (GHz)	> 26	> 26	> 26

Figure 4.19 shows the S-parameters of 2-turn, 3-turn, and 5-turn arch-like suspended solenoid inductors obtained from measurements and from the curve-fitting modeling. These curve-fitted models have S-parameter values close to those obtained from measurements but do not show exact fit. From the results summarized in Table 4.3, a 2-turn arch-like inductor has an inductance of 0.62 nH, a maximum Q-factor of 22.15 at 6.36 GHz, and a very small turn-to-turn stray capacitance. With more turns, the 3-turn and 5-turn arch-like solenoid inductors have inductances of 0.68 nH and 0.80 nH, and slightly lower maximum Q-factor of 20.45 and 20.01, respectively. In Figure 4.20, the model Q-factors are seen to be lower than the measured Q-factor values but they both have the same trend in that the more the number of turns, the lower the Q-factor. The model peak-Q frequencies are in good agreement with the measurements. Figure 4.21 shows physical models of 2-turn, 3-turn, and 5-turn arch-like solenoid inductors.

In curve-fitting of the model equations to the measured data, initial guesses of model parameters and their lower and upper bounds have to be first defined. Convergence of model parameters to the solutions of the model equations depends largely on the choices of the initial values and the upper and lower bounds. It has been found that the imaginary part of measured admittances fit to the model equations very well. This makes the initial guess value of inductance converges very easily even when the guess value varies by an order of magnitude. On the other hand, the real part of measured admittances does not fit well to the model equations especially at low frequencies. This gives Q-factor values of the model lower than the values obtained from the measurements.

Simplified physical model is the third modeling method used here. Similar to traditional  $\pi$ -model method, simplified physical model method translates the two-port ABCD-parameters into a particular narrow band circuit representation with a  $\pi$ -network. The advantage of the

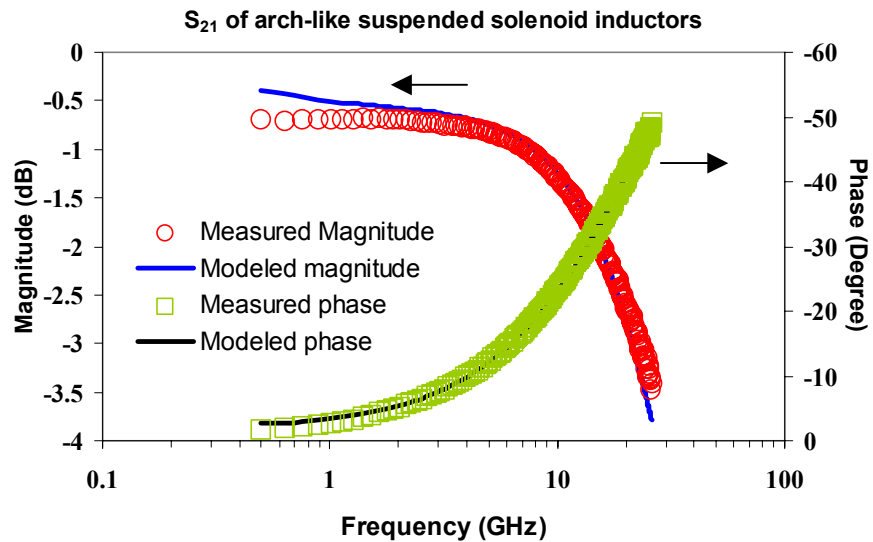


**Figure 4.18:  $S_{21}$  parameter of a 2-turn arch-like solenoid inductor obtained from measurements and from curve-fitting modeling.**



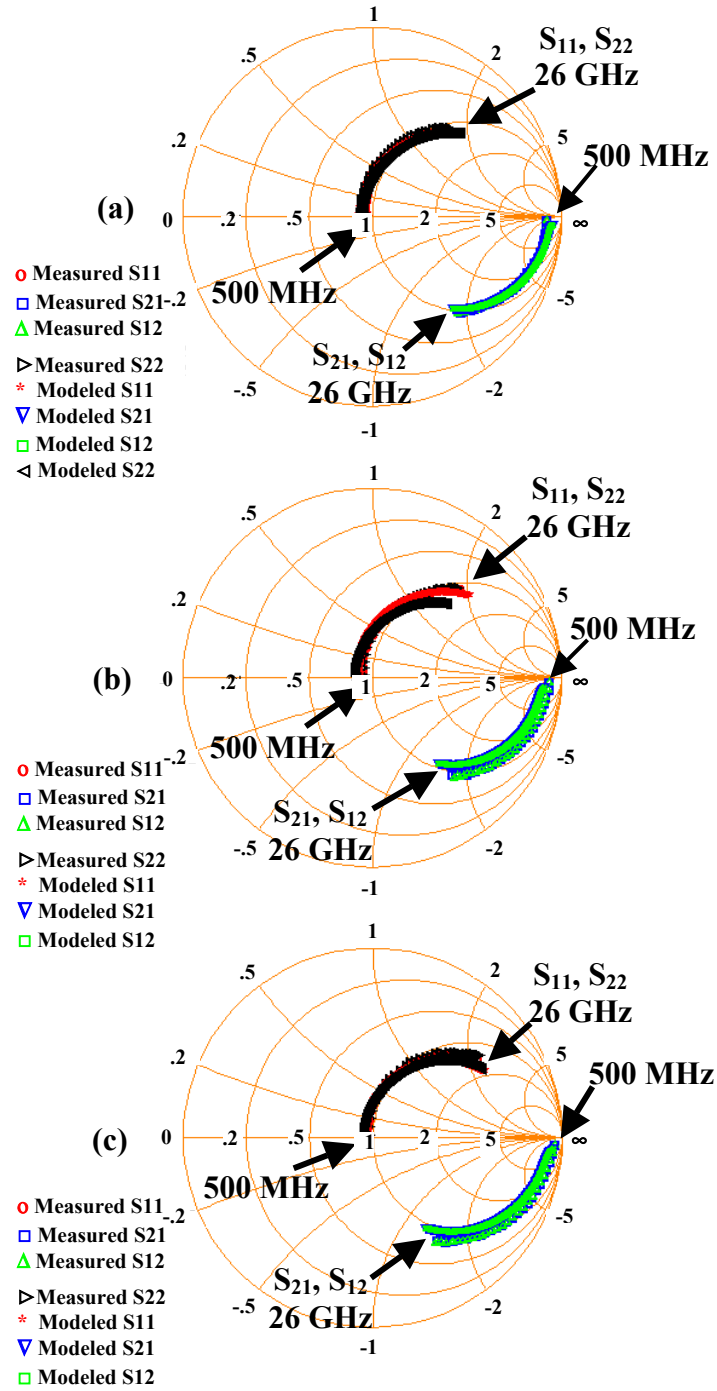
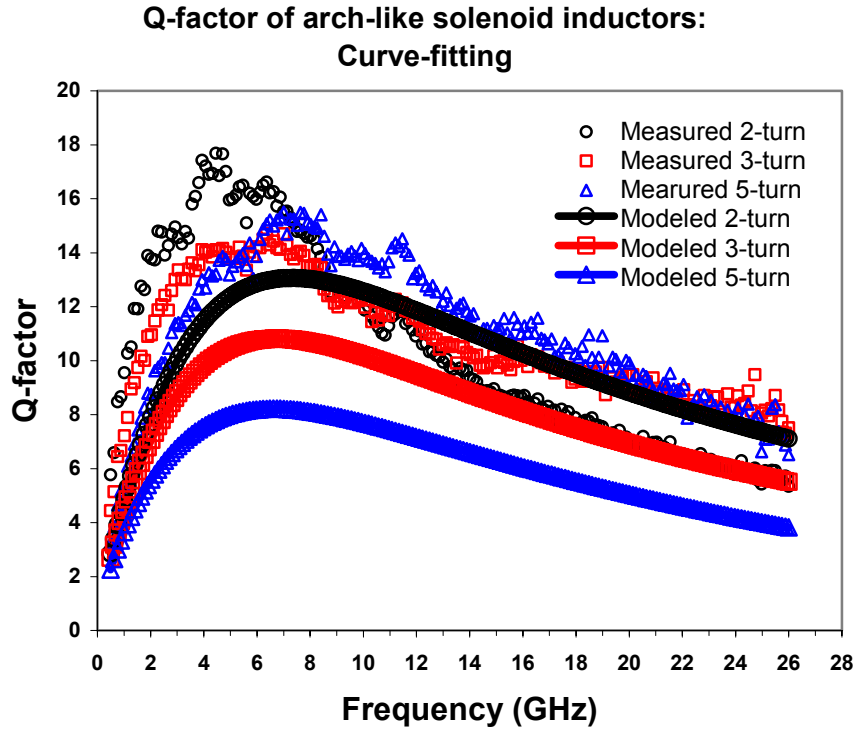


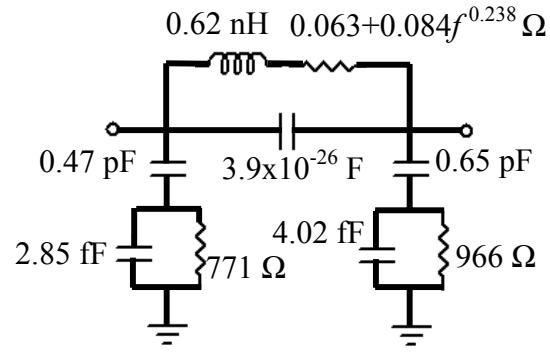
Figure 4.19: S-parameters of (a) 2-turn, (b) 3-turn, and (c) 5-turn arch-like suspended inductors obtained from measurements and from curve-fitting modeling.



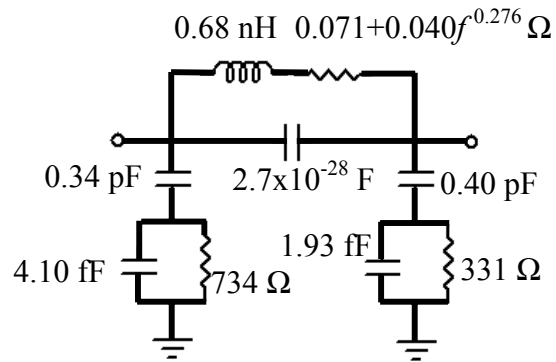
**Figure 4.20: Q-factors of arch-like suspended solenoid inductors from measurements and from curve-fitting modeling.**

simplified physical modeling method is its simplicity. It provides physical representation of the inductors without difficulties of curve-fitting. The drawback of the simplified physical modeling method is that it often gives negative resistances at high frequencies. Figure 4.22 show the simplified physical model parameters of 2-turn, 3-turn, and 5-turn arch-like solenoid inductors as a function of frequency.

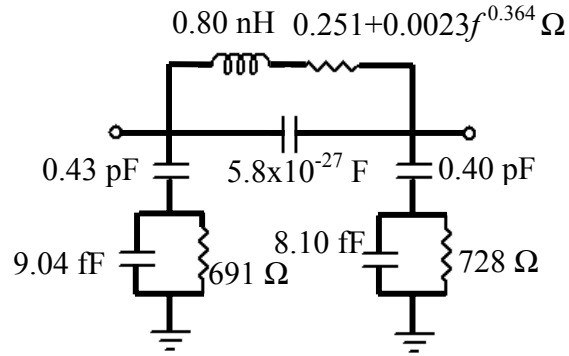
In this model, inductance values decrease slowly as the frequency increases. The series resistances are near  $1\ \Omega$  and become negative at frequencies above 15 GHz. For the shunt capacitance and resistance, the capacitance value decreases exponentially with frequency and become less than 10 fF at frequencies above 5 GHz while the shunt resistance values are in the range of  $350\ \Omega$  to 1 k $\Omega$ .



(a)



(b)



(c)

**Figure 4.21: Physical  $\pi$ -models of (a) 2-turn, (b) 3-turn, and (c) 5-turn arch-like inductors from curve-fitting.**

Since the series branch of the  $\pi$ -network does not have self-resonant frequency below 26 GHz, its measured value of self-resonant frequency and stray inter-turn capacitance  $C_S$  cannot be determined from the measurement data. The value of  $C_S$  is then determined by the guess value that gives Q-factor values from the model close to the Q-factor values from the measurements.

Figure 4.23 shows Q-factors of a 2-turn arch-like solenoid inductor with different initial guess values of  $C_S$ . The Q-factors of 2-turn, 3-turn, and 5-turn arch-like solenoid inductors resulting from this model for  $C_S$  values of 2.00 fF, 3.06 fF, and 3.51 fF, respectively, are compared to the measured Q-factor values in Figure 4.24.

As discussed in section 3.2, Equation (3.61) for Q-factor for this model consists of three parts;  $\omega L_S/R_S$ , substrate loss factor, and self-resonant factor. If substrate loss and self-resonant factors can be eliminated, Q-factors of arch-like solenoid inductors can be represented only by  $\omega L_S/R_S$ . Figure 4.25 shows the substrate loss and self-resonance factors as a function of frequency. It can be seen that the substrate loss factor is the major degradation factor of Q-factor since it drops quickly as frequency increases.

Since the series resistance  $R_S$  values turn negative at frequencies approximately above 18 GHz, the substrate loss factor values in Figure 4.25 also turn negative. In Equation (3.61), when  $R_S$  values are negative, both substrate loss factor and  $\omega L_S/R_S$  parts becomes negative resulting in positive Q-factor values. Figure 4.26 shows the Q-factor values calculated with and without the substrate loss and the self-resonant factors.

Using the simplified physical modeling method, the Q-factor values of arch-like solenoid inductors are in good agreement with values obtained from the measurements and the Sonnet simulations. Figure 4.27 shows a comparison of Q-factors resulting from the Sonnet simulation,

from the measurements, and from the simplified physical model of a 2-turn arch-like solenoid inductor.

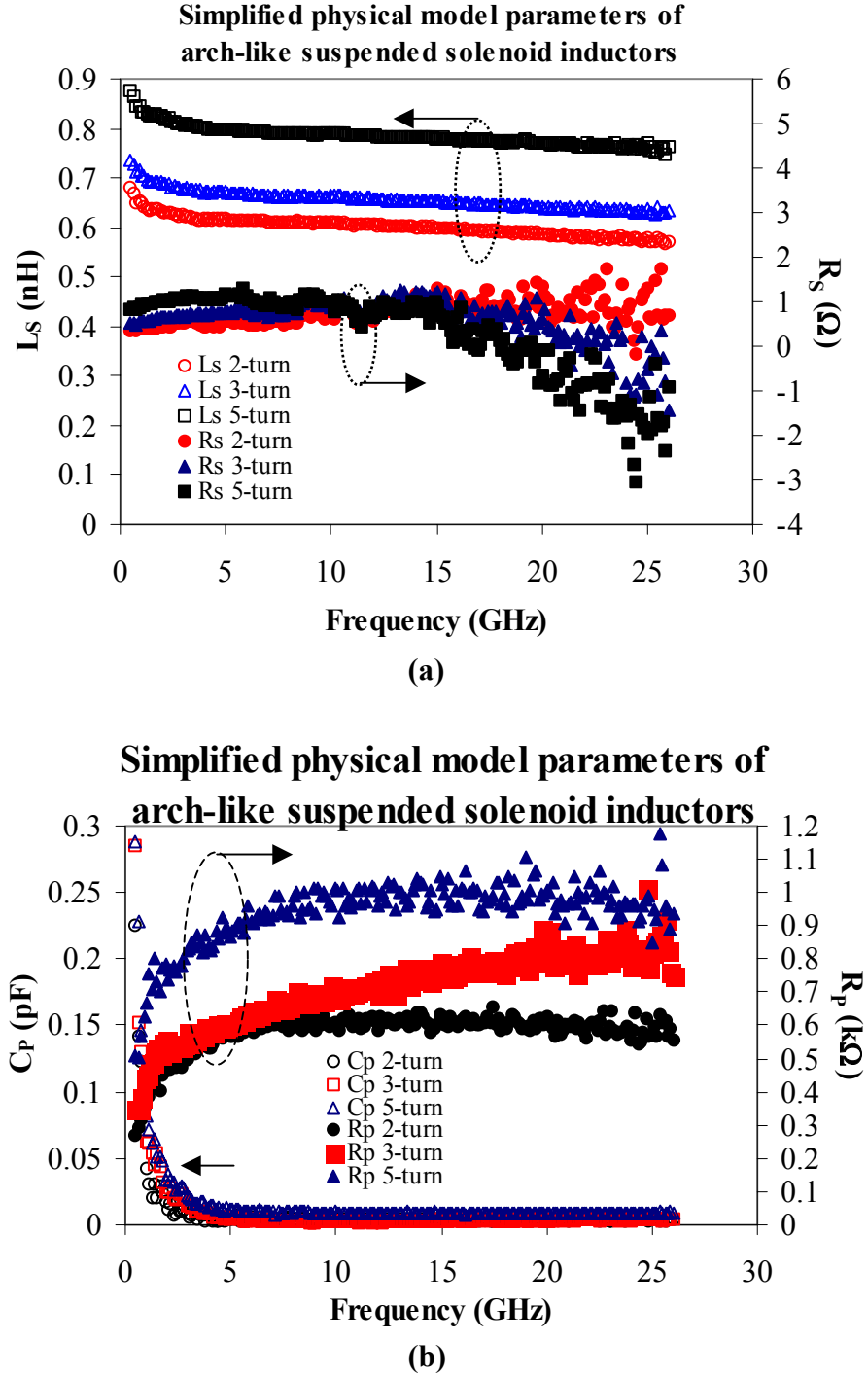


**Figure 4.22: Simplified physical  $\pi$ -model parameters of arch-like solenoid inductors: (a)  $L_S$  and  $R_S$ , and (b)  $C_P$  and  $R_P$ .**

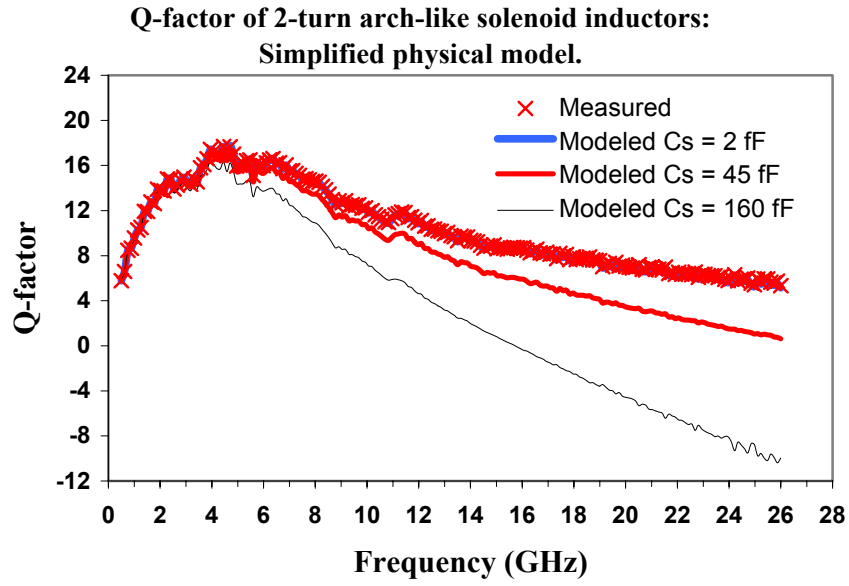


**Figure 4.23: Modeled Q-factors of a 2-turn arch-like solenoid inductor resulting from different guess values of the simplified physical  $\pi$ -model parameter  $C_s$ .**

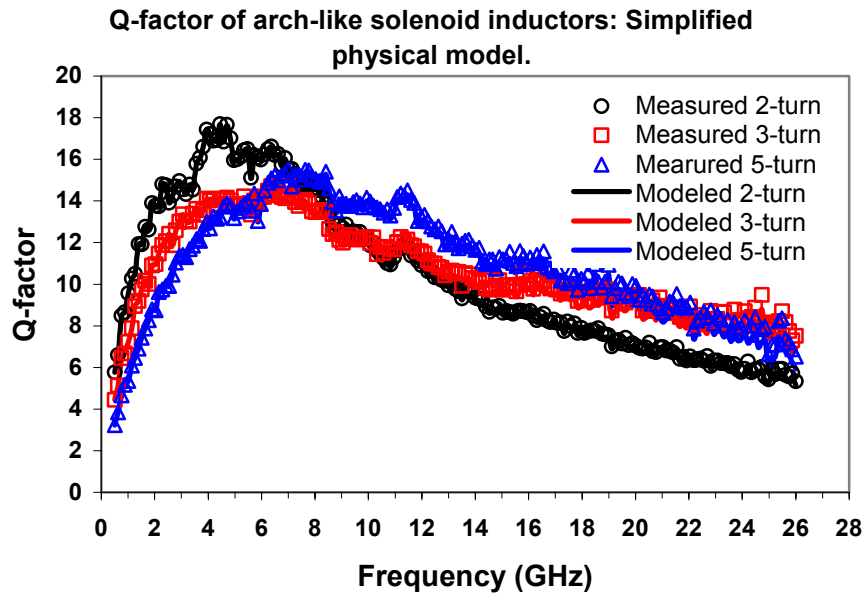


**Figure 4.24: Measured and simplified physical model Q-factor values of arch-like solenoid inductors.**

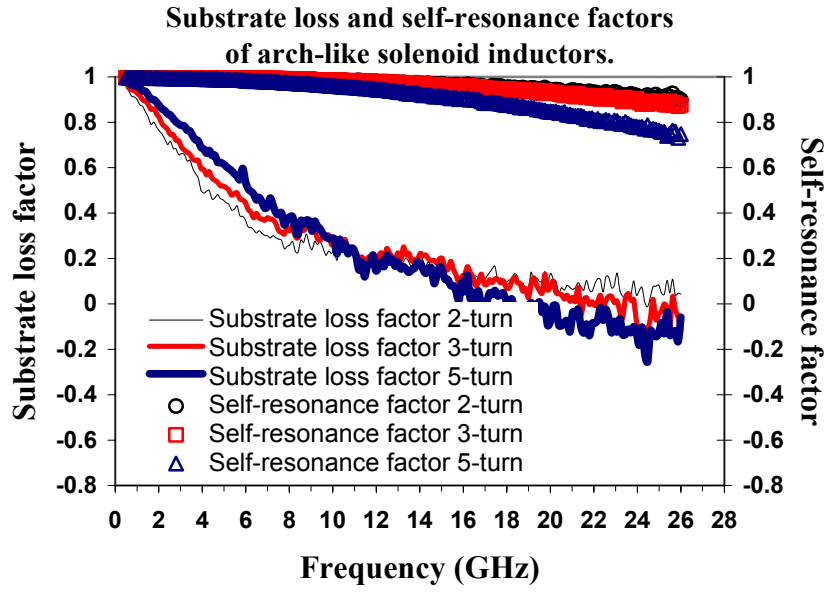


**Figure 4.25: Substrate loss and self-resonance factors of arch-like solenoid inductors obtained from a simplified physical model.**

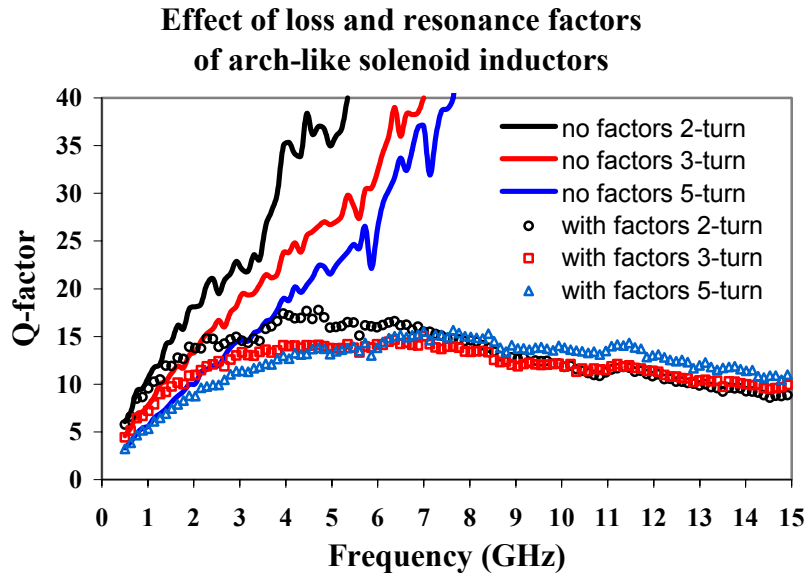


**Figure 4.26: Simplified physical modeled Q-factors of arch-like solenoid inductors with and without taking the substrate loss and resonance factors into account.**

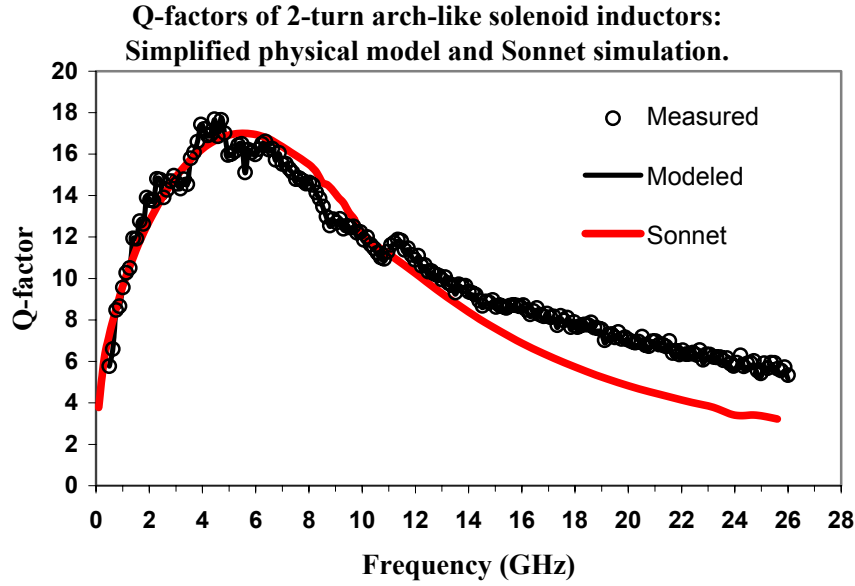


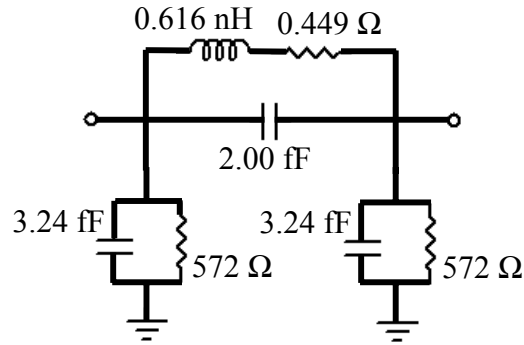
**Figure 4.27: Q-factor comparison of a 2-turn arch-like solenoid inductor resulting from Sonnet simulation, from measurements, and from the simplified physical model.**

Simplified physical model parameters at peak-Q frequencies are summarized in Table 4.4 and depicted in Figure 4.28. The self-resonance frequencies are approximated by the inductance  $L_S$  at low frequencies and capacitance  $C_P + C_S$  at high frequencies. Expressing peak normalized Q-factors in terms of Q per nH results in the 2-turn, 3-turn, and 5-turn arch-like inductors having normalized Q-factor values of  $28.64$ ,  $21.94$ , and  $19.49 \text{ (nH)}^{-1}$ , respectively.

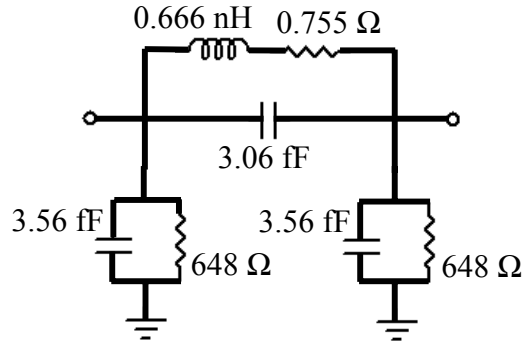
**Table 4.4: Parameters of 2-turn, 3-turn, and 5-turn arch-like solenoid inductors with simplified physical  $\pi$ -models.**

No. of turns	Peak Q	$f_{Q_{\max}}$ (GHz)	$L_S$ (nH)	$R_S$ ( $\Omega$ )	$C_S$ (fF)	$C_P$ (fF)	$R_P$ (k $\Omega$ )	$f_{\text{Self-resonant}}$ (GHz)
2	17.64	4.70	0.616	0.449	2.00	3.24	0.572	88.59
3	14.61	6.49	0.666	0.755	3.06	3.56	0.648	75.80
5	15.42	7.00	0.791	0.903	3.51	10.63	0.928	47.59

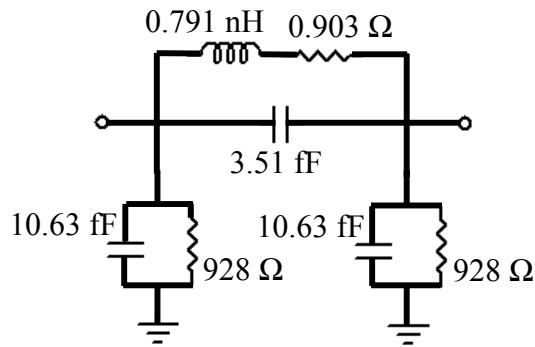




2-turn arch-like solenoid inductor at 4.70 GHz



3-turn arch-like solenoid inductor at 6.49 GHz



5-turn arch-like solenoid inductor at 7.00 GHz

**Figure 4.28: Simplified physical  $\pi$ -models of 2-turn, 3-turn, and 5turn arch-like solenoid inductors at their peak-Q frequencies.**

Using the simplified physical modeling method, the Q-factor values of arch-like solenoid inductors are close to the values from measurements and Sonnet simulations. measurement, and simplified physical model of a 2-turn arch-like solenoid inductor. Inductance values obtained from measurements and simplified physical models for the 2-turn, 3-turn, and 5-turn arch-like solenoid inductors at their peak-Q frequencies are 0.616 nH, 0.666 nH, and 0.791 nH, respectively.

These inductance values include extra self-inductances of the straight wires such as the substrate spacers, suspending beams, and via pads. The total extra self-inductance values calculated from Equation (4.4) are 0.363 nH, 0.364 nH, and 0.381 nH for 2-turn, 3-turn, and 5-turn arch-like solenoid inductors, respectively. Subtracting this extra self-inductance from the values 0.616 nH, 0.666 nH, and 0.791 nH, obtained from measurements results in the corrected inductance values of 0.253 nH, 0.302 nH, and 0.410 nH, for the 2-turn, 3-turn, and 5-turn arch-like solenoid inductors, respectively. In comparison, the inductance values obtained from Wheeler's formula given by Equation (4.3) are 0.060 nH, 0.094 nH, and 0.160 nH, respectively.

The discrepancy between the corrected inductance value (0.153 nH) obtained from Sonnet simulation and the corrected inductance value (0.253 nH) obtained from measurement of a 2-turn solenoid inductor is approximately 0.10 nH. The discrepancy between the inductance value (0.060 nH) obtained from Wheeler's formula and the corrected inductance value (0.253 nH) obtained from measurement of a 2-turn solenoid inductor is approximately 0.193 nH. The discrepancies between the inductance values (0.094 nH and 0.160 nH) obtained from Wheeler's formula and the corrected inductance values (0.302 nH and 0.410 nH) obtained from measurements of the 3-turn and 5-turn solenoid inductors are approximately 0.208 nH and 0.250 nH. The causes for discrepancies between the inductance values obtained from the Wheeler's

formula, the Sonnet simulation, and the measurements of arch-like inductors are not certain. The discrepancies may results from the cross-sectional shapes of the solenoid cores used. A rectangular shape is used for Sonnet simulations, an arch-like shape is used for the fabricated inductors, and a circular shape is used in the Wheeler's formula. Different arrangements of the conductor around the air core may be another cause for the discrepancies of inductance values since the Wheeler's formula assumes that the solenoid is tightly wound using a circular wire and the turns almost touch each other, while the simulated and the fabricated inductors have turns further apart from each other due to limitations in fabrication.

#### **4.4 Conclusions**

Arch-like suspended solenoid inductors with 2-turn, 3-turn, and 5-turn configurations have been designed, fabricated, and characterized. Sonnet EM microwave simulation software has been used to study effects of air-gap distance in which the inductor body is suspended above the substrate. Raising the inductor above the substrate can significantly increase Q-factor. It has been found that air gap of 30  $\mu\text{m}$  is a reasonable choice since there is no significant improvement in Q-factor when the air gap is greater than 30  $\mu\text{m}$ . Arch-like solenoid inductors have been fabricated using electroplating of copper through thick photoresist and through conformal photoresist molds and utilizing an arch-like profile sacrificial photoresist mound. The fabricated inductors have been characterized by high frequency measurements and by modeling. On-wafer high frequency probes and automatic vector network analyzer measurement setup has been used to obtain two-port S-parameters of the inductor. S-parameters has been converted to ABCD parameters and translated into  $\pi$ -model equivalent circuits. Simple, physical, and simplified physical  $\pi$ -models have been obtained.

Using an appropriate initial value of  $C_s$  it has been found that a simplified physical modeling method gives the equivalent circuit model and the modeled values of the Q-factors show very good agreement with the measured Q-factor values. The arch-like solenoid inductors with 2-5 turns have inductances in a range of 0.62-0.79 nH, series resistance in a range of 0.449-0.903  $\Omega$ , and Q-factors in a range of 15.42-17.64 at peak-Q frequencies in a range of 4.7-7.0 GHz. The normalized peak Q-factors are in a range of 19.49-28.64 (nH)<sup>-1</sup>. Self-resonant frequencies of arch-like inductors are above the maximum measured frequency at 26 GHz but the values estimated from simplified physical models are 88.6 GHz, 75.8 GHz, and 47.6 GHz, for the 2-turn, 3-turn, and 5-turn inductors, respectively.

## **CHAPTER 5**

### **ON-CHIP DOME-SHAPED SPIRAL INDUCTORS**

Although on-chip planar spiral inductor suffers from large capacitive coupling and eddy current losses in the substrate, its structural and fabrication simplicity is one of the well-known advantages. Since strong high frequency magnetic field along the spiral axis penetrates directly through the bulk of the substrate, the inductor body must be placed away from the substrate in order for this loss to be minimized.

Utilizing LIGA-like surface micromachining technology, copper spacers as high as several hundreds micrometers can be inserted to raise the inductor body up from the substrate. In addition, stray capacitance between the turns of inductor can be reduced, by arranging the spiraling conductors along the curvature of a sacrificial dome-shape polymer mound so that the sidewalls of the spiral conductor do not fully overlap with the adjacent turns.

This chapter describes design, fabrication, and characterization of a novel three-dimensional on-chip inductor with dome-shape spiral conductor for high frequency application. The on-chip dome-shape spiral inductor is built utilizing thick photoresist electroplating mold based microstructure, patterning and deformation of a sacrificial photoresist dome, conformal electrodeposition and patterning of photoresist, and removal of polymeric layers. High frequency measurements and equivalent circuit modeling are utilized in inductor characterization.

#### **5.1 Design**

This section describes design issues relevant to on-chip spiral inductors for high frequency applications. Similar to arch-like solenoid inductors, series resistance of the conductor is one of the major sources of Q-factor degradation at high frequencies. To minimize the series

resistance, copper is used as conductors due to its low resistivity. Other sources of parasitic effects such as substrate loss and self-resonant factors can also be reduced. The first by raising the spiral conductor away from the substrate and the latter by arranging each turn of the spiral conductor at a different height level so that their side walls have a small overlap. Utilizing CMOS compatible post-IC micromachining techniques such as copper electroplating through thick photoresist molds and through a conformal photoresist mold on a dome-shape sacrificial photoresist mound, a new type of spiral inductor as depicted in Figure 5.1 can be realized.

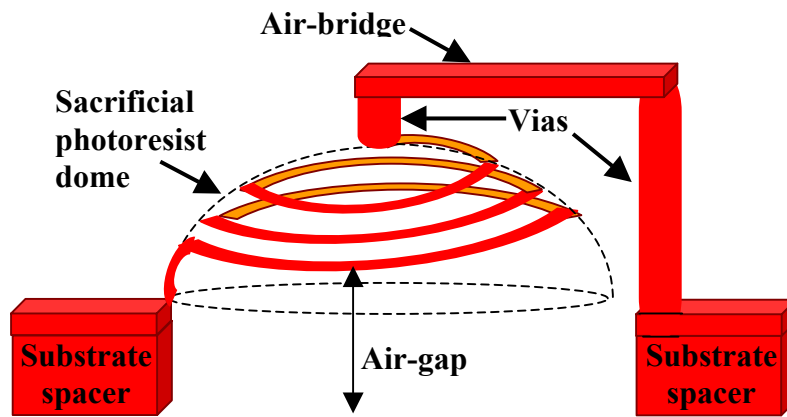


**Figure 5.1: Schematic diagram of a suspended dome-shape spiral inductor.**

The inductor consists of a pair of copper spacers, a copper spiral conductor, a short and a long via, and an air-bridge. One end of the spiral conductor is directly connected to one of the spacers. The other side of the spiral conductor is connected to the other spacer through the short via, the air-bridge, and the long via.

In order to evaluate the appropriate height of the air-gap between the substrate and the inductor's body needed for improved performance, Sonnet EM electromagnetic software tool is used to simulate performances of spiral inductors with different air-gaps above the silicon

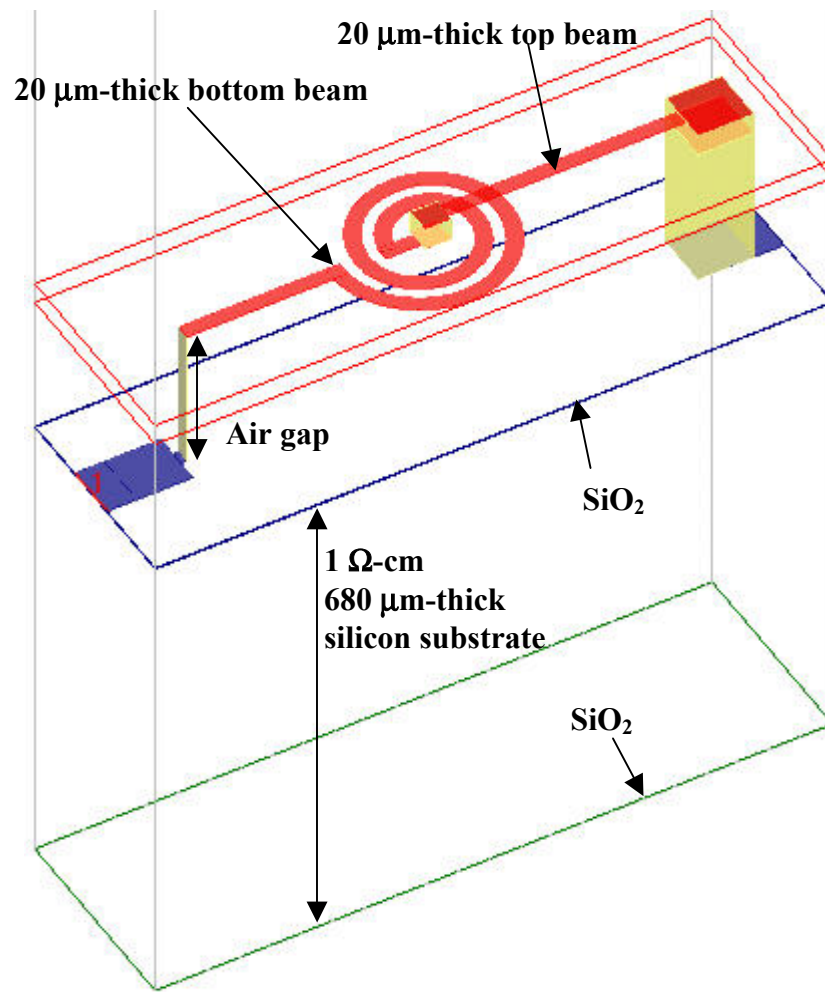
substrate. Due to limited software capabilities, only a flat spiral inductor can be simulated. In addition, only suspended spiral inductors with up to 2 turns can be simulated since simulation time of bigger inductors with Sonnet would be at least several days, if successfully done at all without computational failure on the available computer resources.

Figure 5.2 shows a three-dimensional drawing of a suspended flat spiral inductor used in the simulation. The flat 2-turn spiral inductor has 25  $\mu\text{m}$  wide and 20  $\mu\text{m}$  thick spiral conductors, 20  $\mu\text{m}$  spacing between turns, 50  $\mu\text{m}$  by 50  $\mu\text{m}$  short via, and 100  $\mu\text{m}$  by 100  $\mu\text{m}$  long via. The spiral conductor has 120  $\mu\text{m}$  inner diameter and 300  $\mu\text{m}$  outer diameter. The height of air-gap between the inductor's body and the silicon substrate is varied from no-gap to 400  $\mu\text{m}$ . The oxidized silicon substrate is 680  $\mu\text{m}$  thick with 1  $\Omega\text{-cm}$  resistivity. Due to limitation of available computer resources, the substrate spacer on the left is removed and replaced by a thin via as used in most planar microwave circuits. Instead of using physically thick spiral conductor, sheet resistivity of the spiral conductor is adjusted to obtain the spiral conductor with a virtual thickness of a 20  $\mu\text{m}$  and the self-capacitance of the inductor is neglected.

The simulated Q-factors of the 2-turn suspended spiral inductor with various air-gap heights are shown in Figure 5.3. It can be seen that Q-factors of this flat spiral inductor improves slightly from peak-Q of 23.45 at 6.5 GHz to 24.77 at 12.0 GHz when the air-gap height is in varied from zero to at least 30  $\mu\text{m}$ . The frequency range, for which Q-factors are approximately above 20, extends from 2 - 9 GHz for the non-suspended inductor case to 2 - 15 GHz for over 30  $\mu\text{m}$  air-gap suspended inductors. In addition, the self-resonant frequency extends from approximately 14 GHz to 21 GHz as seen clearly from the points where the Q-factors approach zero in Figure 5.3. Table 5.1 shows model parameters given by Sonnet EM simulations. Figure

5.4 shows equivalent circuit models of the flat suspended and non-suspended spiral inductors at their peak-Q frequencies.

From Figure 5.3, it is concluded that increasing the air-gap height from 30  $\mu\text{m}$  to 400  $\mu\text{m}$  does not significantly improve the inductor performance. Therefore, 30  $\mu\text{m}$  high air-gap will be used in the fabrication of the suspended dome-shape spiral inductor in this work.



**Figure 5.2: Drawing of a suspended flat spiral inductor used in Sonnet simulations.**



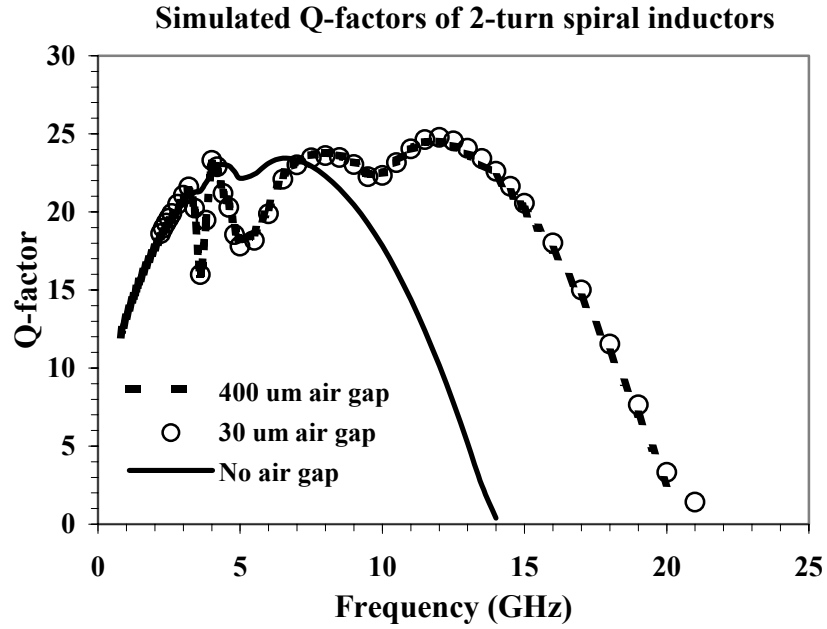


**Figure 5.3: Q-factors of 2-turns flat spiral inductors with various air-gap heights obtained from Sonnet simulation.**

**Table 5.1: Model parameters of 2-turn flat spiral inductors simulated by Sonnet EM.**

Air-gap	Peak Q	Peak-Q freq. (GHz)	$L_S$ (nH)	$R_S$ ( $\Omega$ )	$C_P$ (fF)	Self-resonant freq. (GHz)
None	23.45	6.5	1.725	1.795	67.65	14.0
30 $\mu\text{m}$	24.77	12.0	1.928	3.653	29.65	21.0
400 $\mu\text{m}$	24.77	12.0	1.928	3.661	29.47	21.0

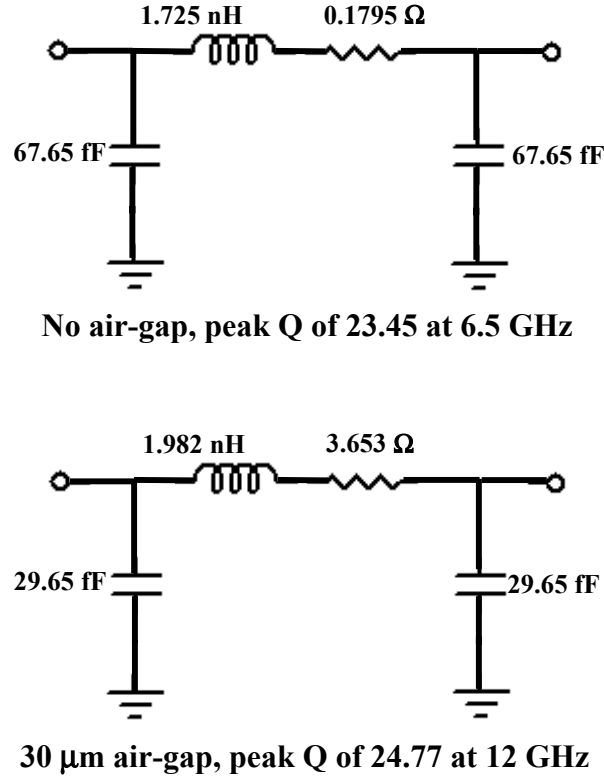


**Figure 5.4: Equivalent circuit models for a 2-turn flat spiral inductor with no air-gap and 30  $\mu$ m high air-gap at their peak-Q frequencies from Sonnet EM simulation.**

In designs of conventional planar on-chip square spiral inductors, the inductance values can be approximated by Greenhouse's formula [57]. Square spiral conductors are popular since their layout can be drawn easily in most layout and patterning tools. However, polygonal spiral conductors have been used to obtain better performance than square spiral conductors [59]. In this dissertation, a circular spiral conductor is used since it is to be fabricated on top of a spherical sacrificial photoresist dome.

Since Greenhouse's formula does not provide inductance estimation for polygonal or circular spiral inductors, other estimation methods must be used. Mohan *et al.* provided simple accurate expressions for planar polygonal spiral inductances using modified Wheeler formula,

current sheet approximation formula, and data-fitted monomial formula [59]. Current sheet approximation provides inductance value of a circular spiral inductor based on the magnetic permeability of conductor, number of spiral turns, average diameter, filling ratio, and empirical constants. The average diameter  $d_{avg}$  of a circular spiral inductor is given by

$$d_{avg} = \frac{d_{out} + d_{in}}{2} \quad (5.1)$$

where  $d_{out}$  and  $d_{in}$  are inner and outer diameters of a spiral inductor as shown in Figure 5.5. The filling ratio  $\xi$  of the spiral inductor is defined as

$$\xi = \frac{d_{out} - d_{in}}{d_{out} + d_{in}}. \quad (5.2)$$

With known average diameter  $d_{avg}$ , filling ratio  $\xi$ , copper permeability  $\mu = 4\pi \times 10^{-7}$  H/m, number of turn  $n$ , and empirical constants  $c_1$ ,  $c_2$ ,  $c_3$  and  $c_4$ , inductance value of the spiral inductor is given by

$$L = \frac{\mu n^2 d_{avg} c_1}{2} [\ln(c_2 / \xi) + c_3 \xi + c_4 \xi^2]. \quad (5.3)$$

For the 2-turn spiral inductor used in Sonnet simulations with 120  $\mu\text{m}$  inner diameter and 300  $\mu\text{m}$  outer diameter, the average diameter is 210  $\mu\text{m}$  and the filling ratio is 0.43. Using empirical constants for circular spiral conductors  $c_1 = 1.00$ ,  $c_2 = 2.46$ ,  $c_3 = 0.00$ , and  $c_4 = 0.20$ , Equation (5.3) gives the inductance of 0.94 nH, compared to 1.73 nH and 1.93 nH from Sonnet simulation of non-suspended and 30  $\mu\text{m}$  suspended 2-turn flat spiral inductors, respectively.

It can be seen that inductance value given by current sheet approximation is lower than the value given by electromagnetic field solving method used by Sonnet EM since current sheet approximation does not take into account conductor thickness and frequency.

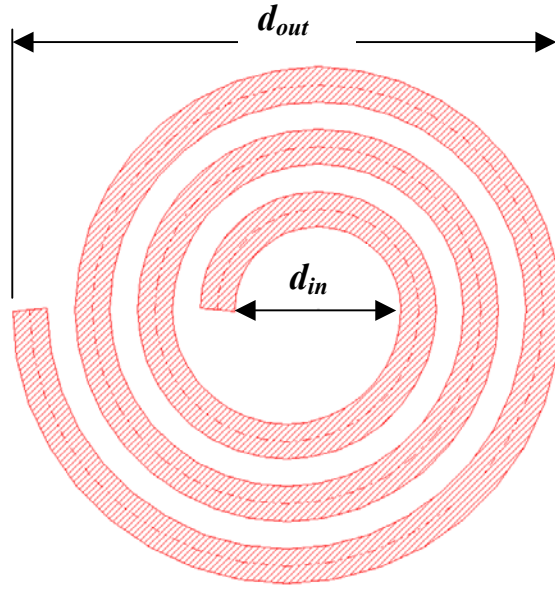


**Figure 5.5: Drawing of a 3-turn spiral conductor.**

For a 3-turn spiral inductor with 120  $\mu\text{m}$  inner diameter and 390  $\mu\text{m}$  outer diameter, the average diameter is 255  $\mu\text{m}$ , the filling ratio is 0.53, Equation (5.3) gives an inductance value 2.30 nH. With expected inductance value of a few nH, a 3-turn on-chip dome-shape spiral inductor is designed with photomask layout shown in Figure 5.6. The copper spiral conductor is 25  $\mu\text{m}$  wide. The spiral has a 120  $\mu\text{m}$  inner diameter and 390  $\mu\text{m}$  outer diameter. The spiral turns are separated by 20  $\mu\text{m}$ . The spiral conductor is fabricated on a sacrificial SJR5740 photoresist dome 800  $\mu\text{m}$  in base diameter and 70  $\mu\text{m}$  high. The short via at spiral center is 50  $\mu\text{m}$  by 50  $\mu\text{m}$  in cross-section and approximately 15  $\mu\text{m}$  high. The long via is 100  $\mu\text{m}$  by 100  $\mu\text{m}$  in cross-section and is approximately 85  $\mu\text{m}$  high. The base of photoresist dome is placed on top of the first SU-8 sacrificial mold layer for electroplating of 30  $\mu\text{m}$  high copper substrate spacer. Along with the inductor, two-port 100  $\mu\text{m}$  pitch G-S-G probe pads and signal ground plane are provided for on-wafer high frequency S-parameter measurement. The dummy probe pads and

ground plane without inductor are also provided for de-embedding of probe pads and ground plane parasitic effects.

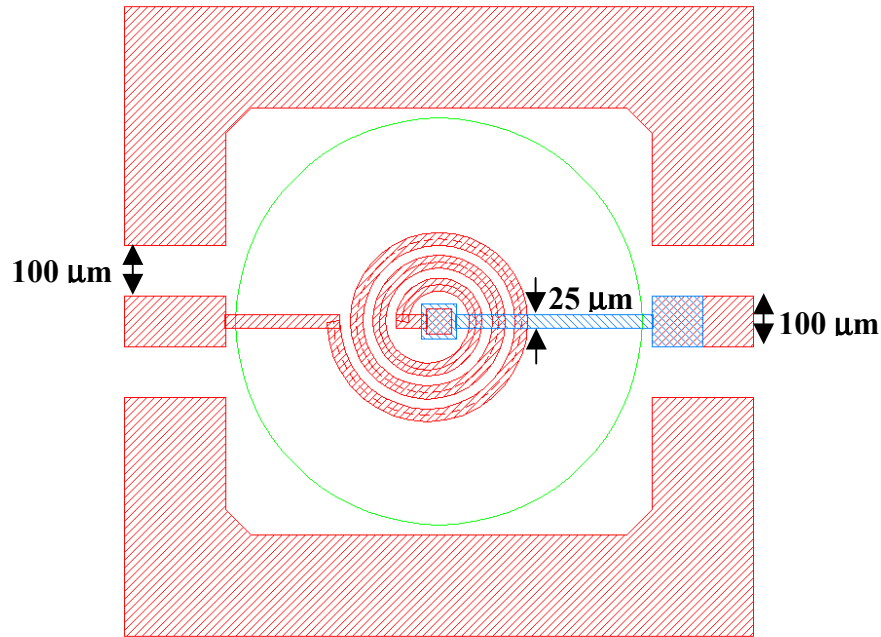


**Figure 5.6: Photomask layout of a 3-turn dome-shaped suspended spiral inductor.**

## 5.2 Fabrication

In order to fabricate the dome-shaped spiral inductor, several technologies are used including LIGA-like micromachining utilizing copper electroplating through thick photoresist mold, deformation of photoresist mesa to form a sacrificial photoresist dome, conformal photoresist deposition and patterning, and removal of polymeric sacrificial materials by plasma etching. Figure 5.7 illustrates fabrication sequences of a suspended dome-shaped spiral inductor. Fabrication starts with obtaining an insulating layer on the Si substrate. This is followed by deposition of electroplating base (10 nm Cr / 150 nm Cu / 10 nm Cr) by e-beam evaporation. A 44 μm thick SJR5740 photoresist layer is spin coated on the plating base. The sample is naturally cooled down outside the oven and is soft baked in an oven by ramping the temperature from 50

°C to 95 °C for one hour. After soft baking the sample is naturally cooled down outside the oven. Since SJR5740 photoresist has low photosensitivity, the sample was dipped in de-ionized (DI) water for one hour so that the photoresist can absorb some moisture. SJR5740 layer is exposed to UV light with a dose of  $380 \text{ mJ/cm}^2$  using circular patterns as a photomask. The UV exposed photoresist layer is developed in MF354 developer for approximately 30 minutes. In this step, the sample must be dipped in the developer immediately after UV exposure to prevent air bubble formation inside this thick photoresist film. Once the sample is placed in the developer, some air bubbles might form on top of the photoresist layer. These bubbles could be occasionally washed out before further development with flowing DI water. After development, cylindrical shape photoresist mesa is formed as shown in Figure 5.7 (a). The cylindrical photoresist mesa is converted into a dome-shape mound by thermal deformation. In this process the sample is placed in the acetone absorption apparatus described in section 2.2 of this thesis. The sample absorbs acetone vapor at 50 °C for 1 minute with a ratio of acetone  $1.66 \mu\text{l}$  per 1 ml of air so that the photoresist can reflow easily. The acetone vapor exposed photoresist mesa is then treated with multiple steps of thermal reflow on a hot plate at 95 °C for 5 minutes, at 130 °C for 4 hours, and finally at 150 °C for 15 minutes. After it is thermally reflowed, the cylindrical photoresist mesa turns into a dome shape. At this point, the photoresist dome is dried enough to be used as a sacrificial support layer for copper spiral conductor. The photoresist residue outside the dome area is cleaned by oxygen reactive ion etching for 5 minutes at 100 mTorr with RF power of 50 W.

In order to fabricate copper spiral conductor on the surface of the photoresist dome, a 100 nm thick Cu plating base is deposited on the sample by magnetron sputtering. A  $16 \mu\text{m}$  thick Eagle2100 layer is then conformally electrodeposited on the plating base along the surface of the

photoresist dome. The sample is cleaned in 10 % sulfuric acid prior to electrodeposition. Electrodeposition is done in an electroplating bath containing 333 ml DI water and 666 ml Eagle2100. The sample is connected to the cathode at 40 V DC constant voltage source while a stainless steel plate is connected to the anode. Both the sample and the stainless steel plate are dipped in electroplating bath approximately 15 cm apart. The solution is constantly stirred with a magnetic bar at 300 rpm. After a 40 V DC constant voltage is applied into the sample, photoresist micelles with positive charges are deposited on the sample. Electrodeposition is automatically stopped since the sample is insulated by the deposited photoresist micelles.

The sample is then mildly rinsed in DI water to wash out excessive photoresist micelles, and dried in air. It is further dried in vacuum at 100 mTorr for 4 hours instead of soft baking to prevent thermal reflow of unexposed Eagle2100 layer. Dried Eagle2100 film as depicted in Figure 5.7 (b) is exposed to UV light with a spiral conductor photomask pattern with a UV exposure dose of 208 mJ/cm<sup>2</sup>. To prevent mechanical damage to the photoresist dome, photomask is placed on top of the wafer without pressing it against the wafer. Using this UV exposure method, the photomask touches only the top of the photoresist dome, resulting in an air-gap approximately 70 µm high between the base of the dome and the photomask. This makes UV exposure at the dome base similar to proximity printing in which the minimum line width  $l_m$  that can be printed is roughly given by

$$l_m = \sqrt{\lambda g} \quad (5.4)$$

where  $\lambda$  is the wavelength of UV light and  $g$  is the gap between the photomask and the photoresist. With i-line 365 nm UV light and the gap height of 70 µm,  $l_m$  is approximately 5.05 µm. After UV exposure, the sample is then developed in a diluted Eagle2005 developer containing 1:24 Eagle2005:DI water at 38 °C. Adhesion failure of Eagle2100 film is avoided by

not stirring the solution nor shaking the sample. The sample with photoresist mold for spiral conductor is mildly rinsed in DI water and dried in air.

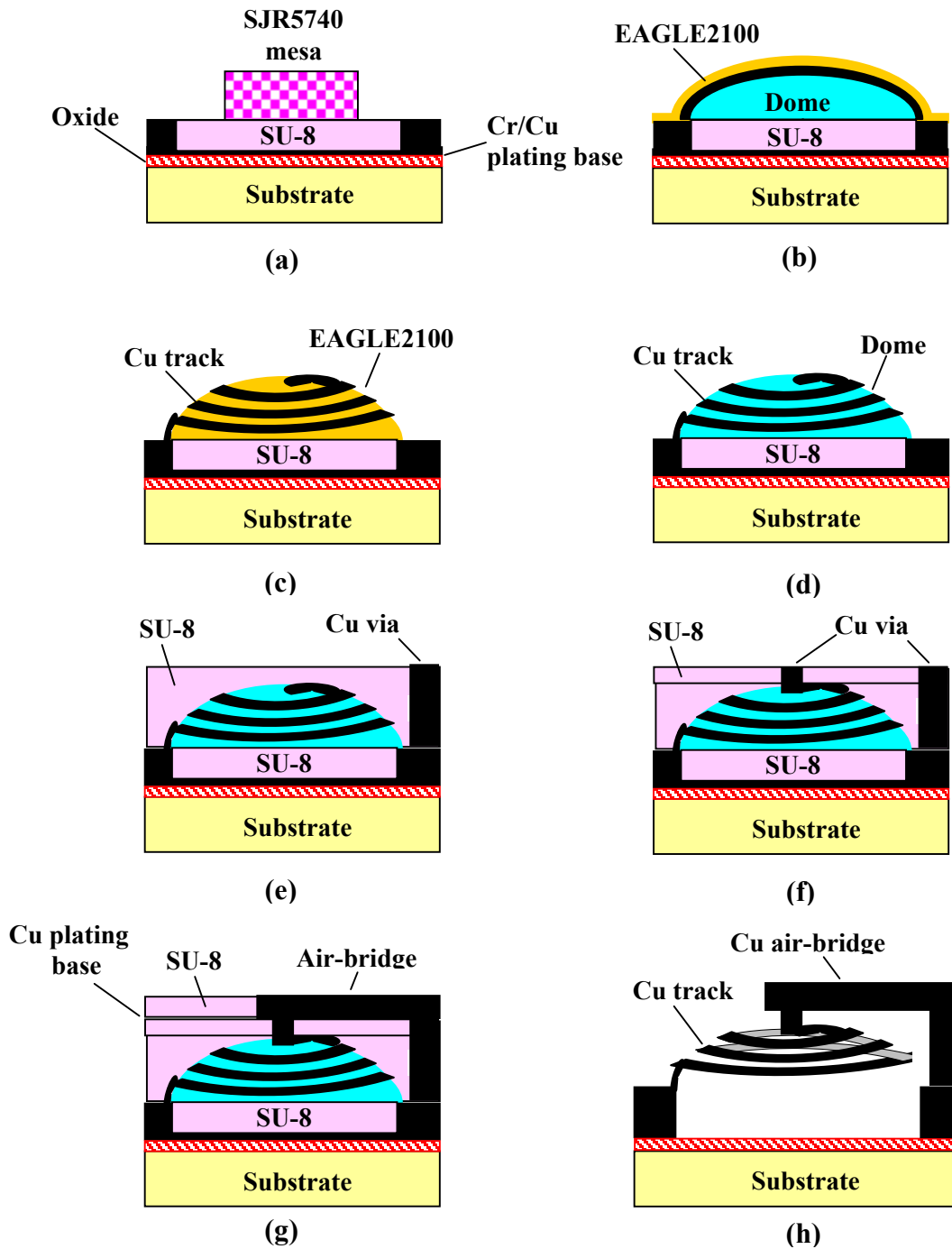


**Figure 5.7: Fabrication sequences for a suspended dome-shaped spiral inductor.**



Eagle2100 photoresist mold is cleaned by reactive ion etching in 100 % oxygen plasma with a pressure of 100 mTorr and RF power of 100 W for 20 minutes, followed by rinsing in 10 % sulfuric acid and DI water. The latter step is for cleaning of the Cu plating base layer. Photoresist mold of spiral conductor is then filled with electroplated copper up to the mold surface. The bath for copper plating is a solution of 250 g cupric sulfate ( $\text{CuSO}_4 \cdot 5\text{H}_2\text{O}$ ), 50 ml sulfuric acid ( $\text{H}_2\text{SO}_4$ ) and 1000 ml DI water. Figure 5.7 (c) shows Eagle2100 photoresist mold after spiral conductor copper electroplating.

Once the copper spiral conductor is formed, Eagle2100 photoresist mold is removed by RIE in a gas mixture of 10 % carbon tetrafluoride ( $\text{CF}_4$ ) and 90 % oxygen at a pressure of 200 mTorr and RF power of 150 W for three hours. Figure 5.7 (d) shows the spiral conductor after Eagle2100 conformal photoresist mold is removed. After removal of Eagle2100 photoresist layer, the old and dirty plating base is removed by a copper etchant containing 1:1:20  $\text{H}_2\text{SO}_4:\text{H}_2\text{O}_2:\text{H}_2\text{O}$  and a new 100 nm copper plating base is recoated by magnetron sputtering.

In order to link the center end of copper spiral conductor to a probe pad, a pair of copper vias and an air-bridge is formed using SU-8 thick photoresist and SJR5740 as electroplating molds respectively. Since the center end of copper spiral conductor and the probe pad are at different height, SU-8 photoresist is also used as a medium for surface planarization. For these purposes, SU-8 2002 is spin-coated on the sample at 3000 rpm to fill voids that might appear on the sample, then an 85  $\mu\text{m}$  thick layer of SU-8 2075 is spin-coated at 3000 rpm to cover the sample to a level slightly above the center end of copper spiral conductor. The sample is soft-baked in an oven at 65 °C for 6 minutes and at 95 °C for 18 minutes and is then exposed to UV light with 423  $\text{mJ}/\text{cm}^2$  dose, to pattern the long via hole to the probe pad. The UV exposed sample is baked at 65 °C for 2 minutes and at 95 °C for 14 minutes and is cooled down naturally

outside the oven. The long via pattern is developed in SU-8 developer for 7 minutes, washed in isopropanol, rinsed in DI water and dried in air. The long via hole is cleaned by reactive ion etching in 100% oxygen plasma with a pressure of 100 mTorr and RF power 100 W for 6 minutes, followed by rinsing in 10 % sulfuric acid and DI water. Copper is filled in the long via hole by electroplating up to the top surface of SU-8 mold as shown in Figure 5.7 (e). To form the short via, previous SU-8 mold was removed by reactive ion etching down to the center end of spiral conductor. A layer of 30  $\mu\text{m}$  thick SU-8 2025 is spin coated at 3000 rpm and soft baked in an oven at 65 °C for 2 minutes and at 95 °C for 6 minutes, and is exposed to UV light with 240  $\text{mJ}/\text{cm}^2$  dose to pattern the short via hole. The UV exposed sample is baked at 65 °C for 2 minutes and at 95 °C for 14 minutes and is cooled down naturally outside the oven. The short via pattern is developed in SU-8 developer for 1 minute and 30 seconds, washed in isopropanol, rinsed in DI water and dried in air. The short via hole is cleaned by RIE in 100 % oxygen plasma for 6 minutes at a pressure of 100 mTorr and RF power of 100 W, followed by rinsing in 10 % sulfuric acid and DI water. Copper is filled in the short via hole by electroplating from the center end of spiral conductor up to the top surface of SU-8 mold as shown in Figure 5.7 (f).

In order to form an air-bridge that connects both short and long vias together, 100 nm thick Cu plating base is coated on the sample by magnetron sputtering, followed by spin coating of 15  $\mu\text{m}$  thick SU-8 2005 photoresist at 750 rpm. The sample is soft-baked in an oven at 65 °C for 2 minutes and at 95 °C for 5 minutes and is exposed to UV light with 130  $\text{mJ}/\text{cm}^2$  dose to pattern the air-bridge. The UV exposed sample is baked at 65 °C for 2 minutes and at 95 °C for 4 minutes and is cooled down naturally outside the oven. The air-bridge pattern is developed in SU-8 developer for 45 seconds, washed in isopropanol, rinsed in DI water and dried in air. The air-bridge photoresist mold is cleaned by RIE in 100 % oxygen plasma with a pressure of 100

mTorr and RF power of 100 W for 6 minutes, followed by rinsing in 10 % sulfuric acid and DI water. Copper is filled in the air-bridge mold by electroplating as shown in Figure 5.7 (g).

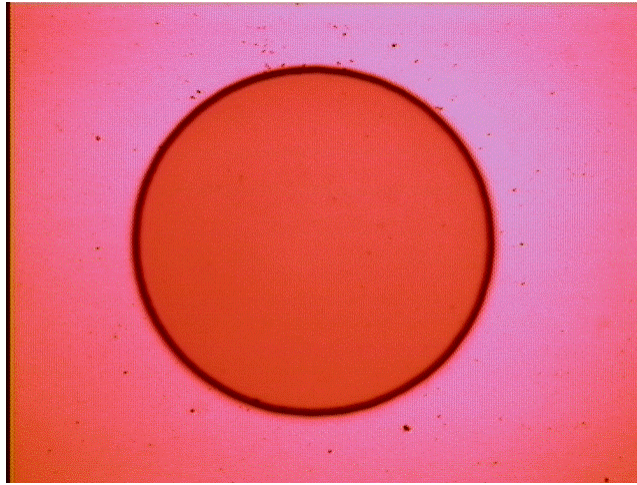
Once all layers are formed, SJR5740 photoresist mold is removed by washing in acetone. Copper plating-base layers are removed by copper wet etchant. SU-8 photoresist mold is removed by RIE using a gas mixture of 10 % carbon tetrafluoride ( $\text{CF}_4$ ) and 90 % oxygen at a pressure of 200 mTorr and RF power of 150 W. After the last plating base is removed, the photoresist dome is washed in acetone and removed by RIE using the same conditions as those for SU-8 removal. Figure 5.7 (h) shows a diagram of a dome-shaped inductor after all sacrificial materials are removed. Figures 5.8 and 5.9 show a 3-turn suspended dome-shape spiral inductor under fabrication. Figure 5.10 shows a SEM photomicrograph of the resulting 3-turn dome-shaped spiral inductor after all sacrificial materials have been removed. The spiral conductor is seen to sag. This might be due to its weight or due to residual stress in the conductors after the sacrificial support material has been removed. This causes the outer most turn to touch the substrate.

Although Sonnet simulation suggests that 30  $\mu\text{m}$  high air gap is enough to optimize substrate losses, future work should increase the height of the substrate spacers to raise the spiral conductor further so that it would not touch the substrate. This will improve the Q-factor and self-resonant frequency of the inductor. The close-up views of both sides of probe pads are shown in Figure 5.11.

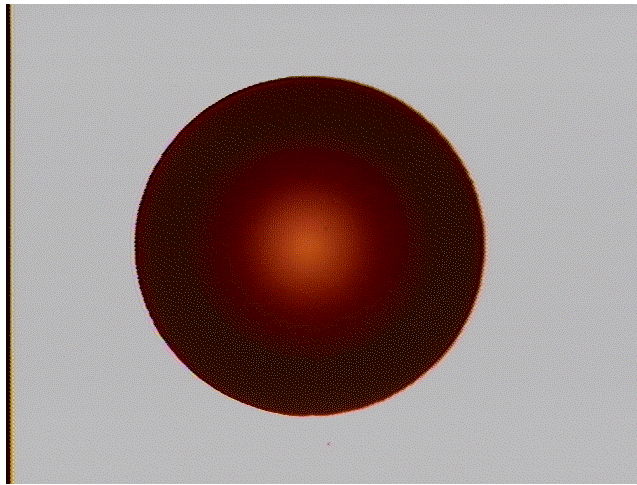
### **5.3 Measurements, Modeling Results, and Discussions**

High frequency measurement procedures described in chapter 3 are used to characterize the fabricated 3-turn dome-shape spiral inductor. Both inductor with probe pads and ground plane (DUT), and probe pads and ground plane only (PAD) are measured with an Agilent 8510C

automatic vector network analyzer from 500 MHz to 26 GHz using a pair of G-S-G type on-wafer 40A-GSG-200P microprobes. The setup is calibrated with a CS-5 standard impedance substrate using the open-short-load-thru procedure.

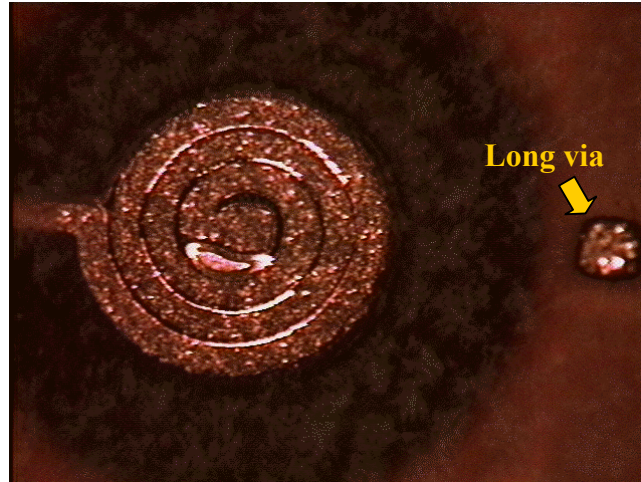


(a)

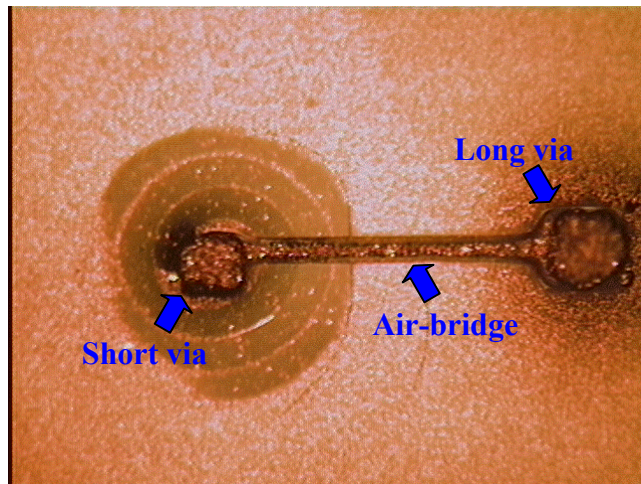


(b)

**Figure 5.8: Photomicrographs of a dome-shaped spiral inductor under fabrication:**  
**(a) a cylindrical photoresist mesa, (b) a photoresist dome converted from a photoresist mesa after reflow process.**



(a)



(b)

**Figure 5.9: Photomicrographs of a dome-shape spiral inductor under fabrication:**  
 (a) electrodeposited spiral conductor on the photoresist dome and electroplated long via, (b) fabricated short via, long via, and air-bridge.

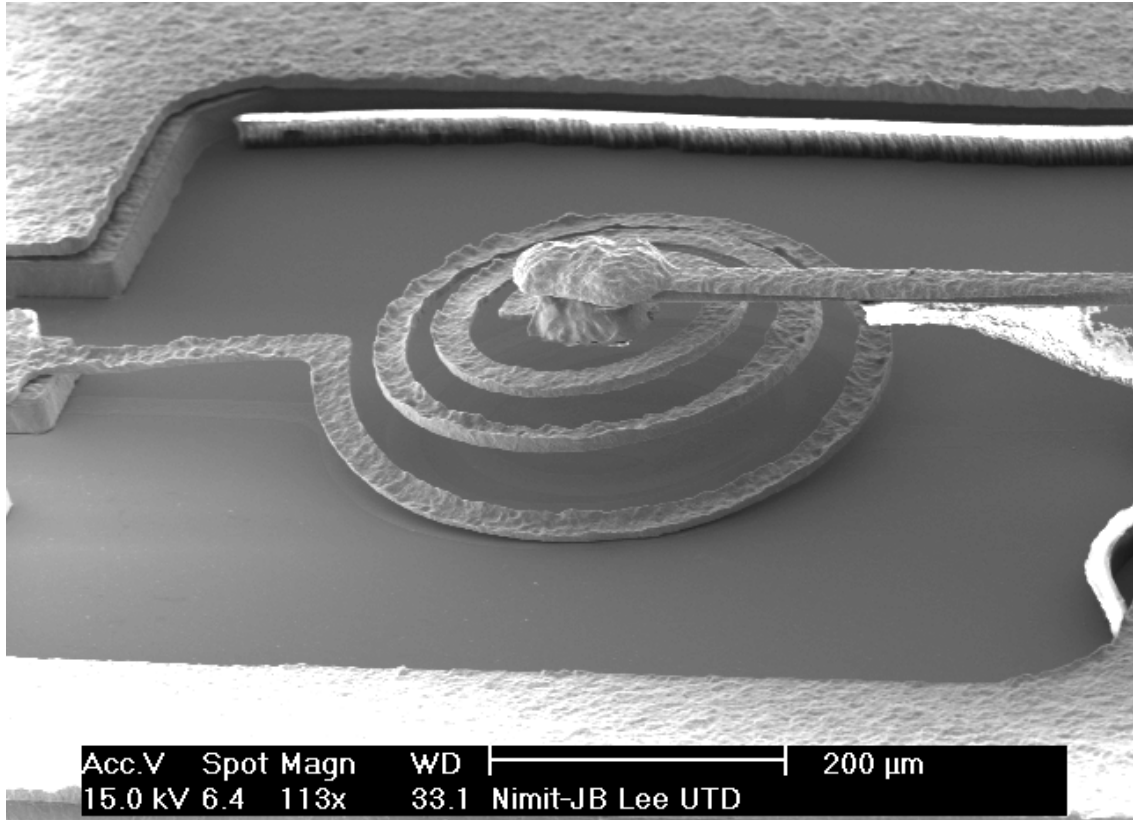
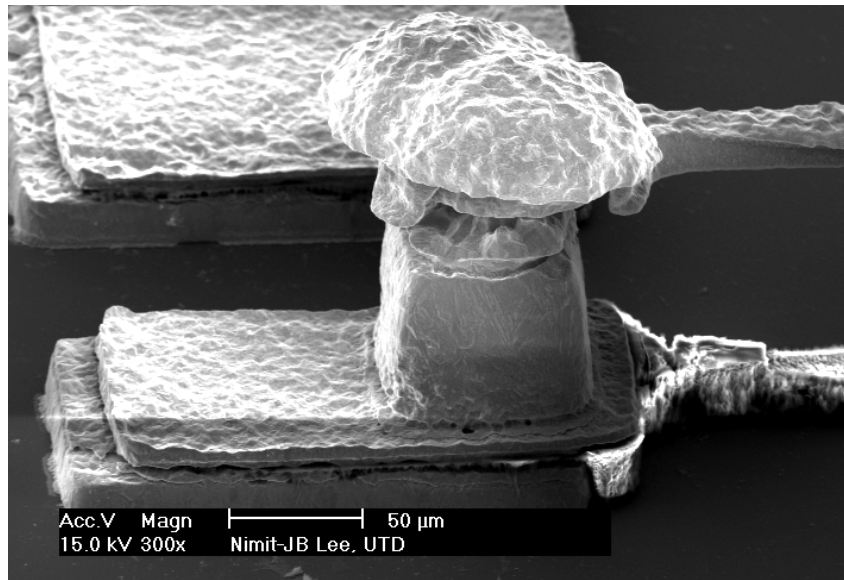
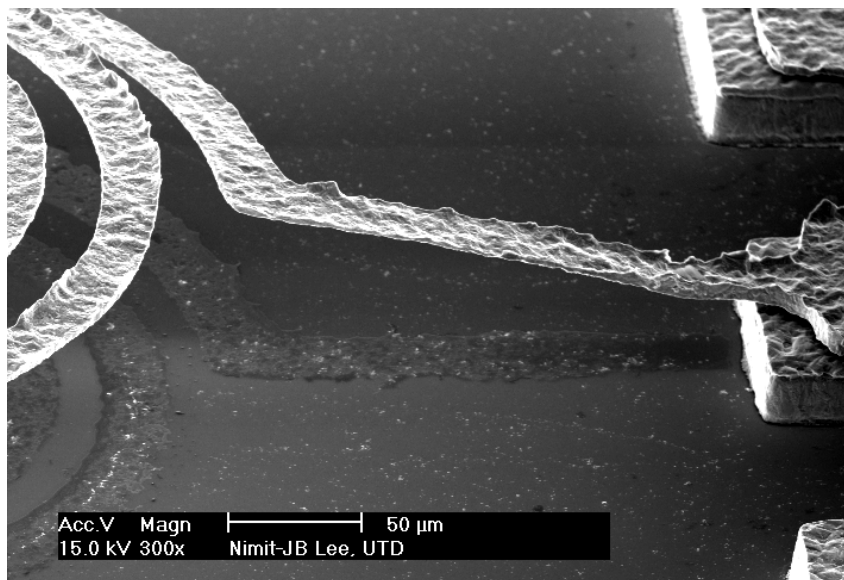


**Figure 5.10: SEM photomicrograph of a 3-turn dome-shaped spiral inductor.**



(a)



(b)

**Figure 5.11: SEM photomicrographs of a 3-turn dome-shape spiral inductor: (a) Probe pad with a long via and an air-bridge, (b) Probe pad with a spiral conductor.**

Figure 5.12 (a) and 5.12 (b) show Smith charts of measured two-port S-parameters of the DUT and the PAD from 500 MHz to 26 GHz. Figure 5.12 (a) indicates that the DUT has large parasitic effect of the probe pads and the ground plane. These parasitic effects can be de-embedded by converting S-parameters of both the DUT and the PAD into Y-parameters and then subtracting the Y-parameters of the PAD from those of the DUT. Figure 5.12 (c) shows Smith chart of the de-embedded S-parameters. Since the de-embedded  $S_{11}$  is almost identical to  $S_{22}$  and  $S_{21}$  is almost identical to  $S_{12}$ , it is found that the structural asymmetry of a dome-shaped spiral inductor does not affect reciprocity of two-port S-parameters.

In chapter 4, it has been shown that Q-factor values of an inductor obtained from the simplified physical modeling fit very well to those obtained from measurements. On the other hand, Q-factor values obtained from the traditional  $\pi$ -model and the physical modeling are obviously lower than those obtained from measurements. Therefore, only simplified physical model method is used in modeling of the dome-shape spiral inductor.

Simplified physical model method translates the two-port ABCD-parameters into a particular narrow band circuit representation with a  $\pi$ -network. It provides physical representation of the inductor without difficulties of curve-fitting. However, it might give negative series resistance at some frequencies at which model parameters values do not represent equivalent circuit correctly. This usually occurs at frequencies far beyond the peak-Q region.

Figure 5.13 shows simplified physical model parameters of a 3-turn dome-shape spiral inductor as a function of frequency. The model has inductance value in a range of 3 nH. The series resistance increases with frequency up to near 100  $\Omega$  at 26 GHz. The shunt capacitance value decreases exponentially with frequency and become less than 27 fF at frequencies above



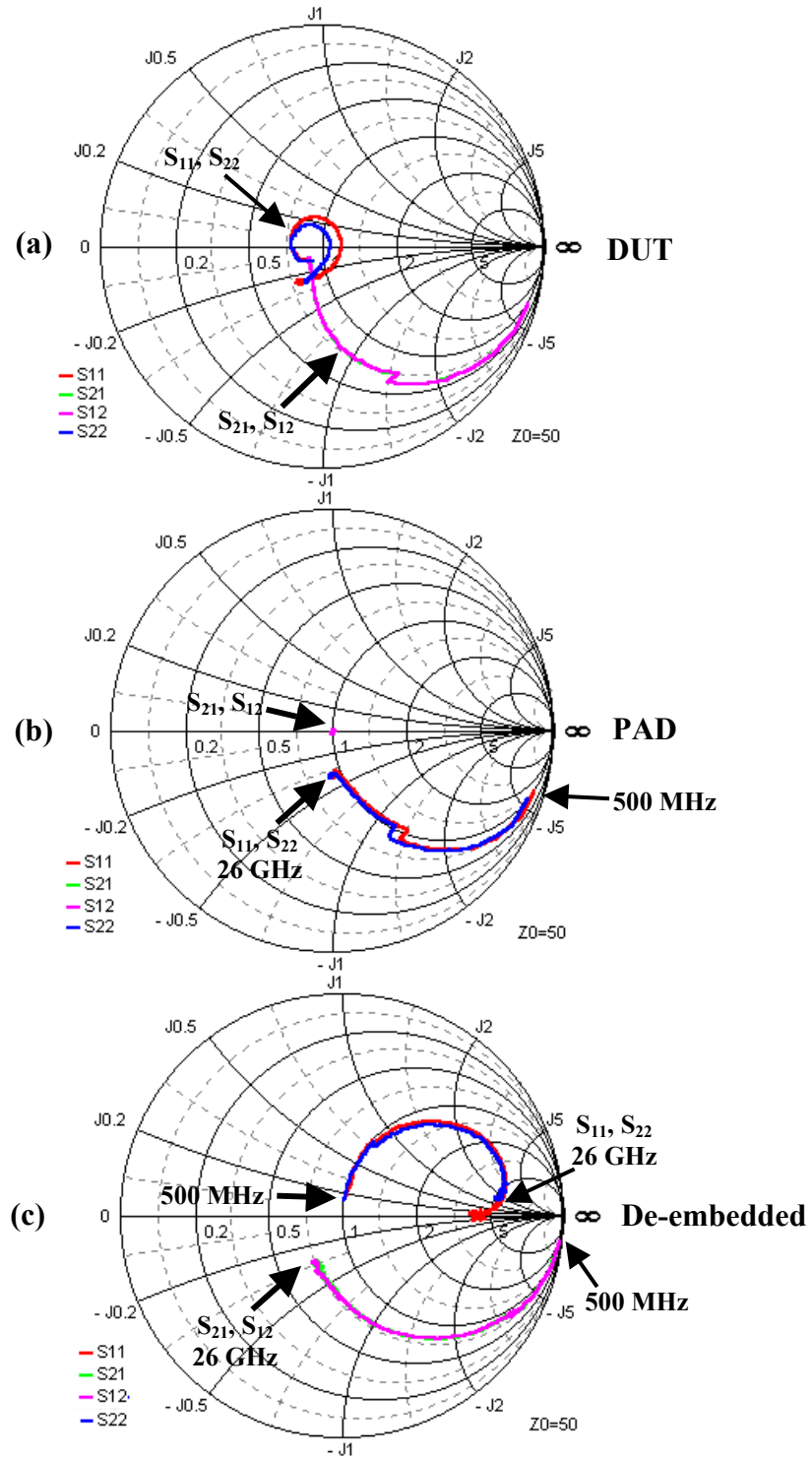


**Figure 5.12: Measured S-parameters of a 3-turn dome-shape spiral inductor: (a) DUT, (b) PAD, and (c) parasitic de-embedded.**

15 GHz while the shunt resistance value decreases exponentially from 3.5 k $\Omega$  to 0.3 k $\Omega$ . Since the series branch of the  $\pi$ -network does not have self-resonant frequency below 26 GHz, its measured value of self-resonant frequency and stray inter-turn capacitance  $C_S$  cannot be determined from the measurement data. The value of  $C_S$  is then determined from the guess value that gives the same Q-factor values as the measured Q-factor values as shown in Figure 5.14. Using  $C_S$  of 9.48 fF gives the best fit for Q-factor values for a 3-turn dome-shaped spiral inductor. For clarity, the Q-factor values obtained from the use of  $C_S$  of 9.47 fF is plot again in Figure 5.15 against the measured Q-factor values.

The resulting 3-turn dome-shape spiral inductor has the peak-Q factor value of 35.9 and the inductance value of 3.368 nH at 1.65 GHz. The self-resonant frequency of 17.84 GHz is obtained from Figure 5.15 at the point where Q-factor values approach zero. As discussed in section 3.2, Equation (3.61) of the model Q-factor consists of a product of three components namely  $\omega L_S/R_S$ , the substrate loss factor, and the self-resonance factor. If substrate loss and self-resonance factors could be eliminated, Q-factors of arch-like solenoid inductors can be represented only by  $\omega L_S/R_S$ . Figure 5.16 shows the substrate loss and self-resonance factors as a function of frequency. In contrast to the arch-like solenoid inductor case, the self-resonance factor is the major factor contributing to the Q-factor degradation since it drops rapidly as the frequency increases.

Figure 5.17 shows the Q-factor values calculated from the simplified physical model with and without the substrate loss and the self-resonance factors. Simplified physical model parameters at peak-Q frequencies are summarized in Table 5.2 and depicted in Figure 5.18. The self-resonance frequencies are approximated by the inductance  $L_S$  at low frequencies and capacitance  $C_P+C_S$  at high frequencies.

## 5.4 Conclusions

A novel suspended 3-turn dome-shaped spiral inductor has been designed, fabricated, and characterized. Sonnet EM microwave simulation software has been used to study effects of air-gap distance in which the inductor body is suspended above the substrate. Raising the inductor above the substrate by 30  $\mu\text{m}$  or greater can improve the Q-factor and the self-resonant frequency of a spiral inductor. Dome-shaped spiral inductor has been fabricated by electroplating of copper in thick photoresist and conformal photoresist molds and by utilizing a sacrificial photoresist dome.

The dome with the base diameter of 800  $\mu\text{m}$  and the height of 70  $\mu\text{m}$  is formed by deformation of a cylindrical photoresist mesa. A copper 3-turn dome-shaped spiral inductor has been demonstrated in this work. In this configuration, most parts of the spiral conductor are suspended in the air to reduce substrate losses. Fabrication of spiral conductor on top of a sacrificial photoresist dome helps reduce inter-turn fringing capacitance since the sidewalls of the spiral conductor turns do not fully overlap to each other. The fabricated inductor has been characterized using high frequency measurements and by modeling. On-wafer high frequency probes and automatic vector network analyzer measurement setup has been used to obtain two-port S-parameters of the inductor. Parasitic effects are removed from the measured S-parameters and converted to ABCD-parameters and translated into  $\pi$ -model equivalent circuits.

A simplified physical  $\pi$ -model has been obtained. It was found that the Q-factor values obtained from the simplified physical modeling technique are in very good agreement with the measured Q-factor values. A 3-turn dome-shape spiral inductor has inductance in the range of 2.58 - 4.01 nH, series resistance of 1  $\Omega$  or less up to 20 GHz, a peak Q-factor of 35.90 at 1.65 GHz, and self-resonant frequency at 17.84 GHz.

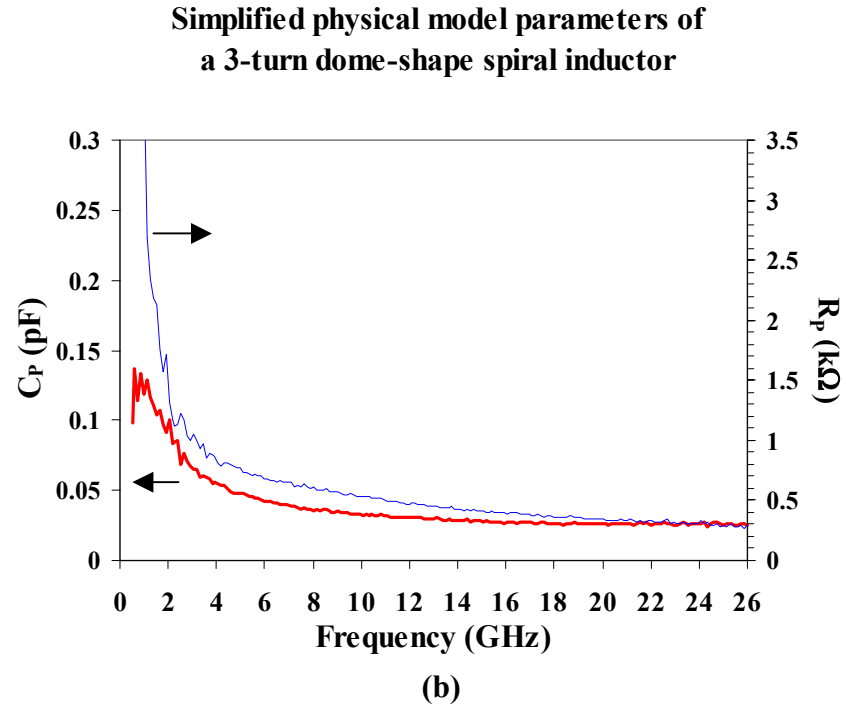
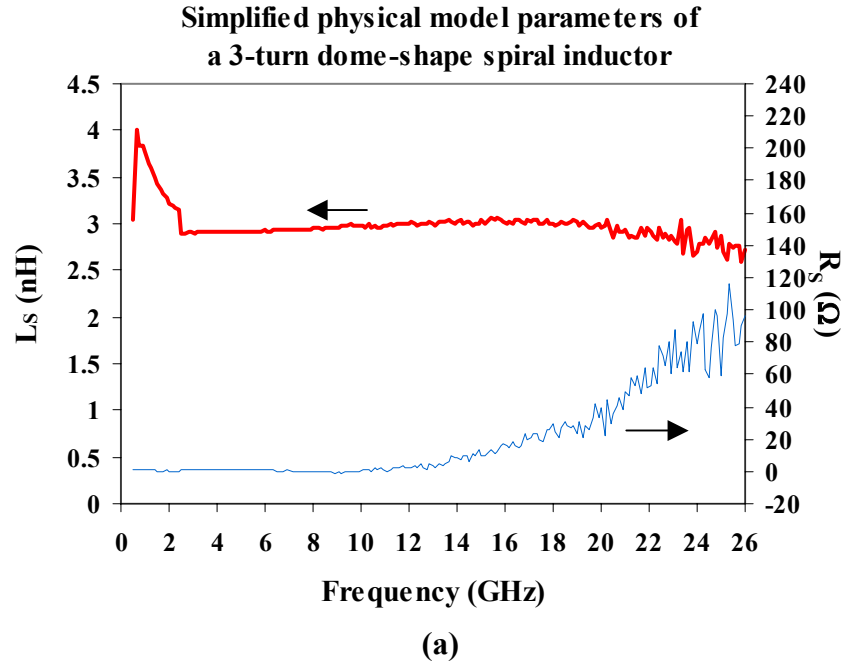


**Figure 5.13: Simplified physical  $\pi$ -model parameters of a 3-turn dome-shape spiral inductor: (a)  $L_s$  and  $R_s$ , and (b)  $C_p$  and  $R_p$ .**

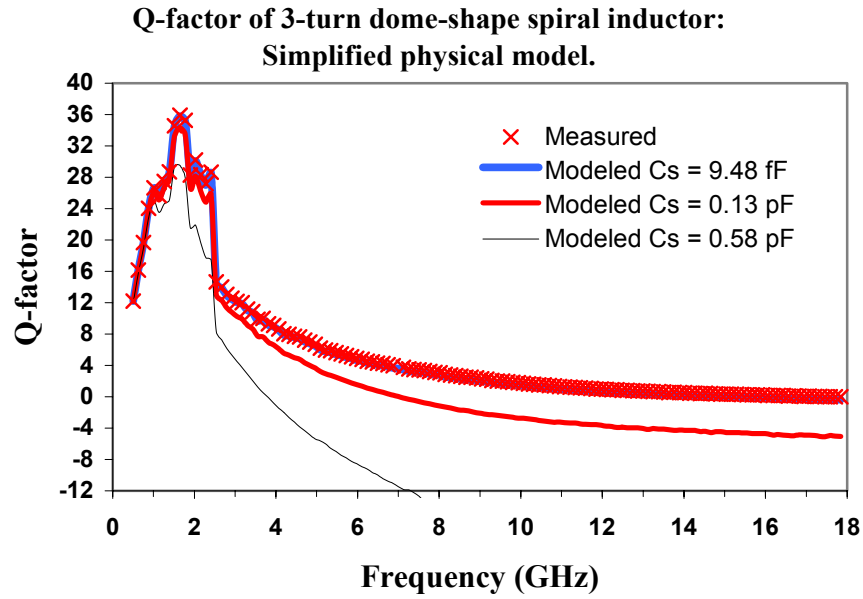


**Figure 5.14: Q-factor values of a 3-turn dome-shaped spiral inductor resulting from three different guess values used in the simplified physical  $\pi$ -model parameter  $C_S$ .**

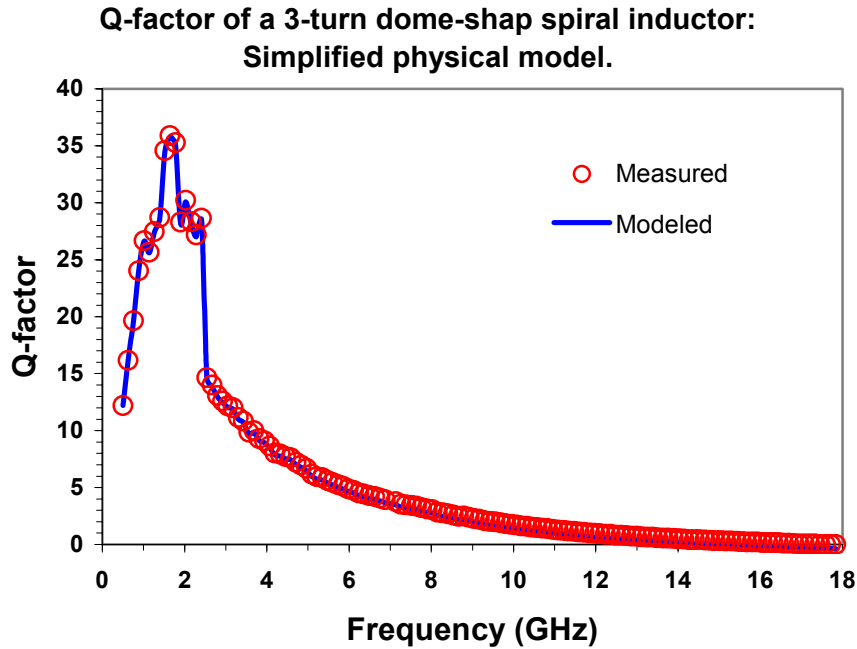


**Figure 5.15: Measured and simplified physical model Q-factor values of a 3-turn dome-shaped spiral inductor.**

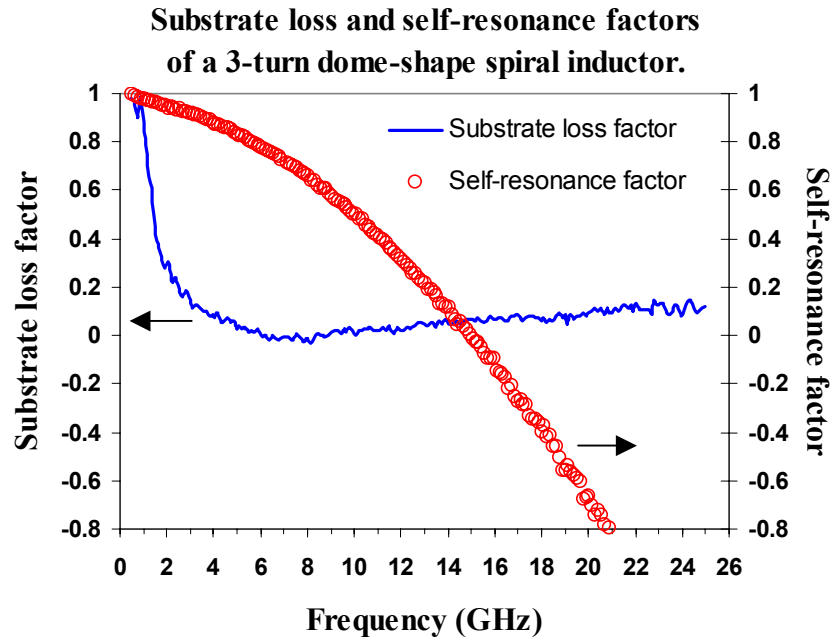


**Figure 5.16: Substrate loss and self-resonance factors of a 3-turn spiral inductor obtained from a simplified physical model.**

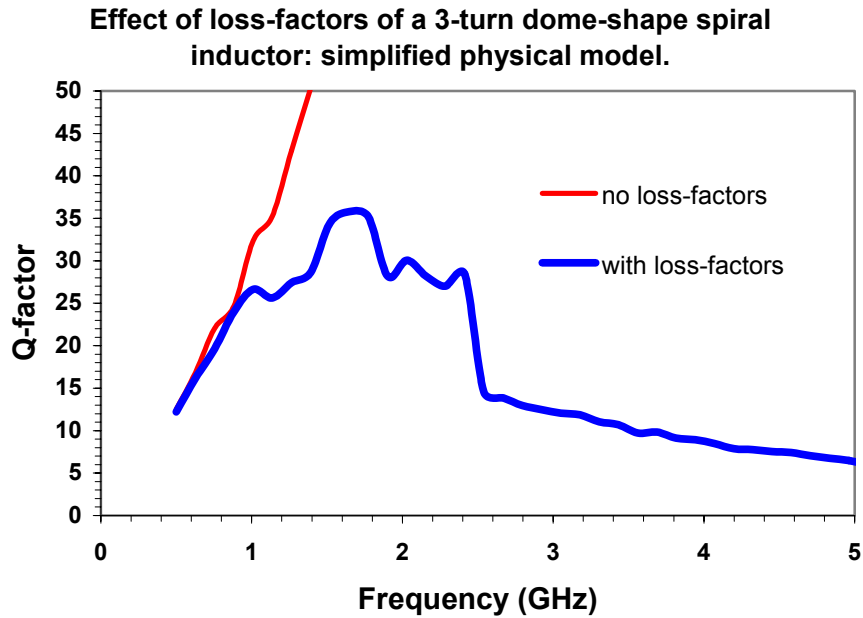


**Figure 5.17: Q-factor values of a 3-turn dome-shaped spiral inductor obtained from simplified physical model, with and without substrate loss and self-resonance factors.**

**Table 5.2: Parameters of a 3-turn dome-shaped spiral inductor with simplified physical  $\pi$ -models.**

Peak Q	$f_{Q\max}$	$L_S$	$R_S$	$C_S$	$C_P$	$R_P$	$f_{\text{Self-resonant}}$
35.9	1.65 GHz	3.368 nH	0.242 $\Omega$	9.48 fF	107 fF	1.76 k $\Omega$	17.84 GHz

**3-turn dome-shape spiral inductor at 1.65 GHz**

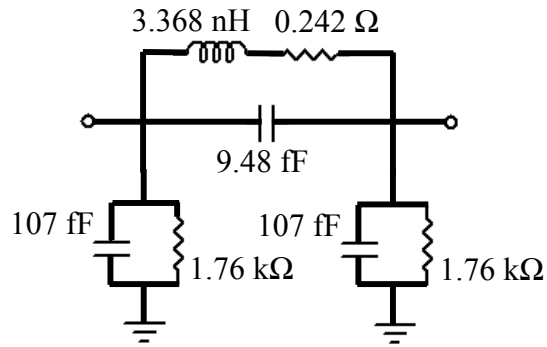


**Figure 5.18: Simplified physical  $\pi$ -model of a 3-turn inductor at peak-Q frequency.**

## CHAPTER 6

### CONCLUSIONS

#### 6.1 Summary

Monolithically integrated passive inductor with high Q-factor and high self-resonant frequency value are very desirable in high frequency circuits for wireless communication devices. At high frequencies, Q-factor and self-resonant frequency of an inductor are significantly degraded due to losses from series resistance of the conductor, magnetically induced eddy current in the substrate, and reduced self-resonant frequency due to capacitance coupling between the inductor's body and the substrate.

In this dissertation, MEMS-based post-CMOS fabrication techniques such as formation of metallic microstructure by electroplating in a thick photoresist mold, formation of arch-like and dome-shaped photoresist mounds as sacrificial three-dimensional structures, formation of three-dimensional metallic microstructures by electroplating in molds formed by conformal electrodeposition and patterning of photoresist, and removal of sacrificial polymeric materials by reactive ion etching, are used for the realization of three-dimensional high-Q and high self-resonant frequency inductors for high-frequency applications. Novel three-dimensional, arch-like solenoid and dome-shaped spiral, inductors have been designed, fabricated, and characterized.

Insertion of air-gap between the inductor's body and the substrate is used to improve inductor's performance as described above. Sonnet EM electromagnetic commercial microwave simulation tool is used to evaluate necessary air-gap height to



enhance high frequency performance of the inductor. According to Sonnet simulations, 30  $\mu\text{m}$  air-gap height is adequate for both solenoid and spiral inductors.

Suspended arch-like solenoid copper inductor has flat bottom directly connected to the arch-like top conductor with an air-core in between. With the arch-like top conductor design, the number of contact points between top and bottom conductors, which are major sources for series resistance of the inductor, reduces from 4 points per turn to 2 points per turn.

Suspended dome-shaped spiral copper inductor has spiral conductor with the outer end connected to one probe pad, and the inner end connected to another probe pad through vias and an air-bridge. The spiral conductor is fabricated on a sacrificial photoresist dome so that sidewalls of spiral turns overlap less with each other reducing inter-turn stray capacitances.

Fabricated inductors are characterized and modeled at high frequencies. An automatic vector network analyzer has been used to measure high frequency S-parameters of the on-chip inductors with the additional ground-signal-ground type transmission line probe pads. Parasitic effects of these additional probe pads and ground plane are de-embedded from the measured data in order to obtain accurate S-parameters. De-embedded S-parameters are converted to ABCD-parameters and directly translated into a  $\pi$ -model network. Three modeling method, traditional simple  $\pi$ -model, physical, and simplified physical  $\pi$ -models, are used to extract equivalent circuit model parameters. The simplified physical modeling method gives the best model parameters in good agreement with the measurement results.

The resulting 2-turn, 3-turn, and 5-turn arch-like suspended inductors have inductances between 0.62 to 0.79 nH and peak Q-factors between 15.42 to 17 at peak-Q frequencies between 4.7 GHz to 7.0 GHz. Self-resonant frequencies of these arch-like inductors are greater than 26 GHz, which is the maximum measurable frequency of our measurement setup. The self-resonant frequency values estimated from the simplified physical models for the arch-like inductors are between 47.6 GHz to 88.6 GHz. The 3-turn dome-shaped spiral inductor has an inductance value of 3.37 nH, peak Q-factor of 35.9 at 1.65 GHz, and self-resonant frequency at 18.74 GHz.

## **6.2 Suggestions for Future Work**

The arch-like solenoid inductors are suitable for applications that need small inductances and small chip area. In contrast, dome-shape spiral inductors occupy larger chip area but provide higher inductance values and higher Q-factor. In high frequency applications that need inductors with small chip area, large inductance, high Q-factors and high self-resonant frequencies, LIGA-like high aspect ratio fabrication techniques might be used to realize high aspect ratio suspended solenoid inductors that provide high inductance values per unit chip area.

Sonnet EM simulation tool can be used to approximate high frequency properties of high aspect ratio suspended solenoid inductor. Figure 6.1 shows three-dimensional drawing of a LIGA-like solenoid inductor used in Sonnet simulation. The simulation results of high aspect ratio suspended solenoid inductors show Q-factors over 40 and inductances between 0.6 nH to 1.2 nH while occupying small chip area as shown in Figure 6.2. Provided

techniques to form high aspect ratio via holes is successful, high Q-factor air core LIGA-like solenoid inductors are possible.

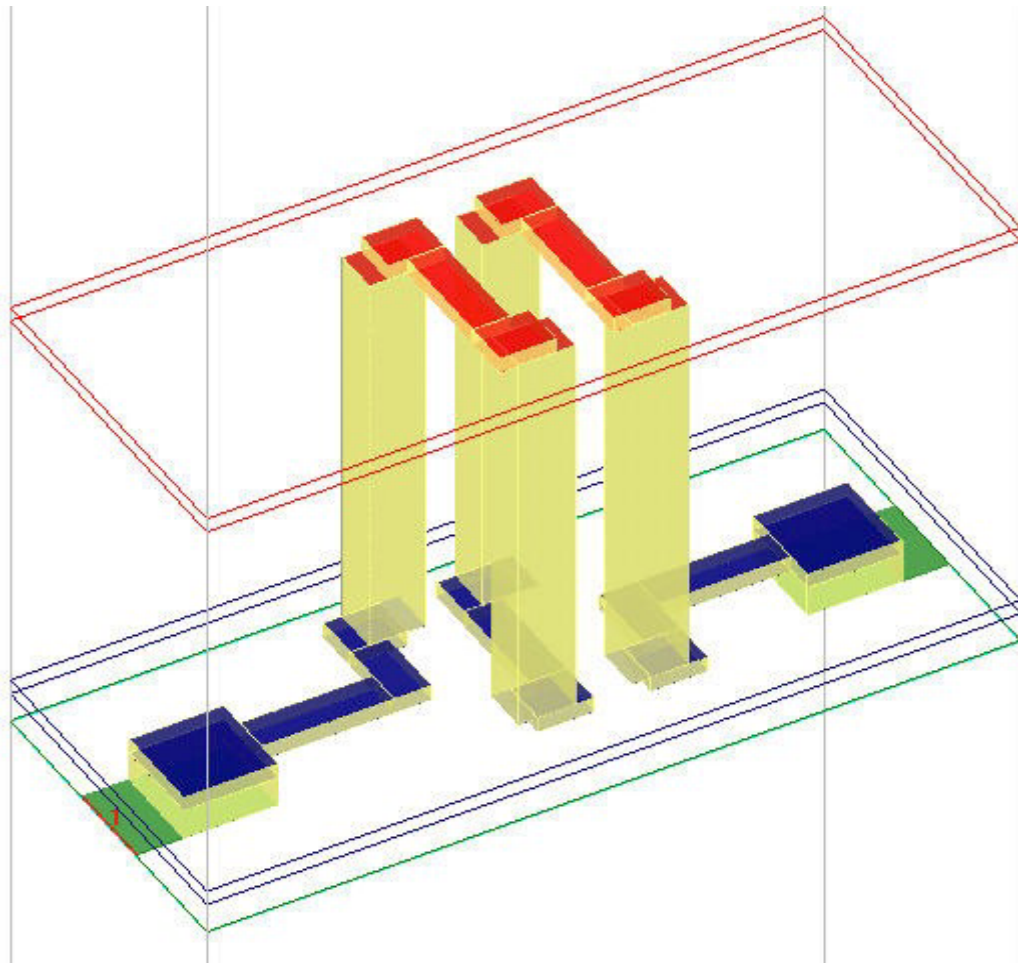


**Figure 6.1: A schematic diagram of high aspect ratio suspended solenoid inductor.**

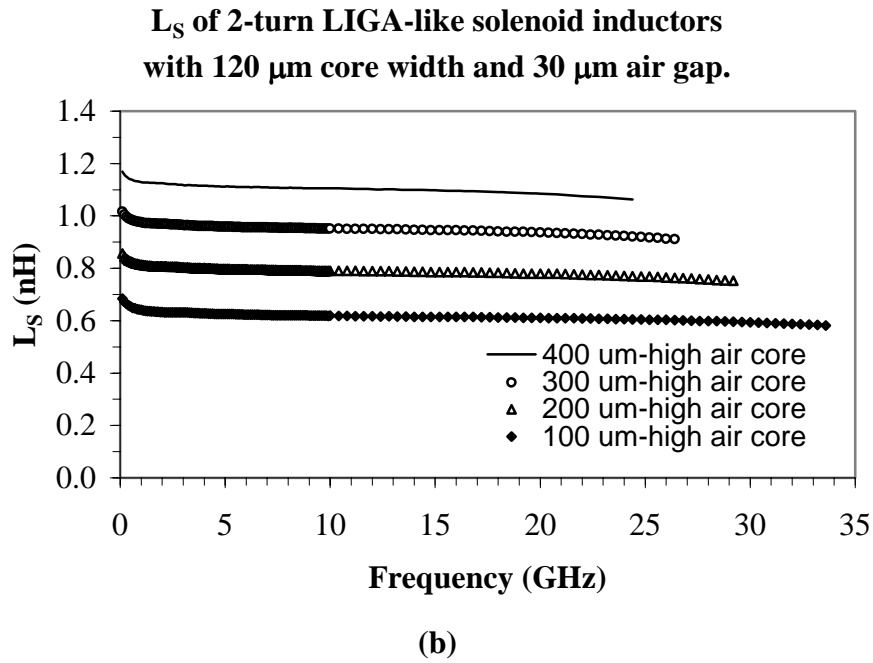
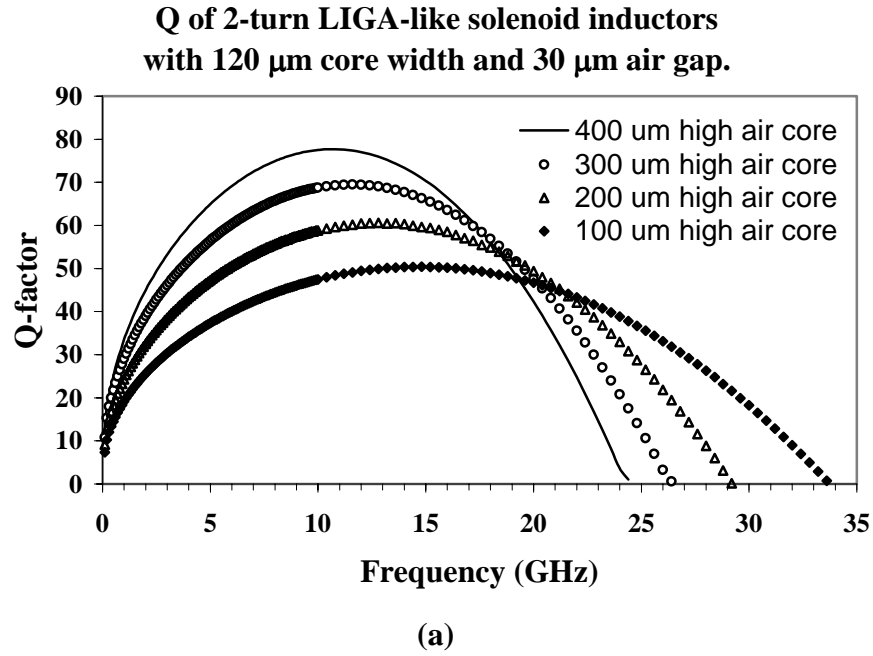


**Figure 6.2: Simulation results of high aspect ratio suspended LIGA-like solenoid inductors with air core heights from 100  $\mu\text{m}$  to 400  $\mu\text{m}$  : (a) Q-factors and (b) inductances.**

## REFERENCES

- [1] R. P. Feynman, "There's plenty of room at the bottom," presented at the American Physical Society Meeting in Pasadena, CA, December 26, 1959; reprinted in *J. Microelectromechanical Systems*, vol. 1, no. 1, pp. 60-66, 1992.
- [2] W. Bacher, W. Menz, and J. Mohr, "The LIGA technique and its potential for microsystems—a survey," *IEEE Trans. Industrial Electronics*, vol. 42, no. 5, pp. 431-441, 1995.
- [3] T. Lisec, M. Kreutzer, and B. Wagner, "Surface micromachined piezoresistive pressure sensors with step-type bent and flat membrane structures," *IEEE Trans. Electron Devices*, vol. 43, no. 9, pp. 1547-1552, 1996.
- [4] K. H. Chau, S. R. Lewis, Y. Zhao, R. T. Howe, S. F. Bart, and R. G. Marcheselli, "An integrated force-balance capacitive accelerometer for low-g applications," *Sensors and Actuators*, vol. A. 54, pp. 472-476, 1996.
- [5] R. A. Syms, "Surface tension powered self-assembly of 3D micro-optomechanical structures," *J. Microelectromechanical systems*, vol. 8, no. 4, pp. 448-455, 1999.
- [6] J. J. Yao, "RF MEMS from a device perspective," *J. Micromech. Microeng.*, vol. 10, pp. R9-38, 2000.
- [7] *International technology roadmap for semiconductors*, 2001 edition, Semiconductor Industry Association, 2001.
- [8] P. Alinikula, R. Kaunisto, and K. Stadius, "Integrating active resonators for wireless applications," *Microwave Journal*, pp. 106-113, January, 1995.
- [9] J. Craninckx and M. Steyaert, "Low-noise voltage-controlled oscillators using enhanced LC-tanks," *IEEE Trans. Circuits and Systems—II: Analog and Digital Signal Processing*, vol. 42, no. 12, pp. 794-804, 1995.
- [10] J. Craninckx and M. Steyaert, "A 1.8-GHz CMOS low-phase-noise voltage-controlled oscillators with prescaler," *IEEE J. Solid-state circuits*, vol. 30, no. 12, pp. 1471-1482, 1995.
- [11] E. R. Brown, "RF-MEMS switches for reconfigurable integrated circuits," *IEEE Trans. Microwave Theory and Techniques*, vol. 46, no. 11, pp. 1868-1880, 1998.
- [12] Y. Liu, A. Borgioli, A. S. Nagra, and R. A. York, "Distributed MEMS transmission lines for tunable filter applications," *Int. J. RF and Microwave CAE* 11, pp. 254-260, 2001.

- [13] D. J. Young, V. Malba, J. J. Ou, A. F. Bernhardt, and B. E. Boser, "A low-noise RF voltage-controlled oscillator using on-chip high-Q three-dimensional coil inductor and micromachined variable capacitor," *Solid-State Sensor and Actuator Workshop*, Hilton Head Island, CA, USA, pp. 128-131, 1998.
- [14] Z. Feng, H. Zhang, K. C. Gupta, W. Zhang, V. M. Bright, and Y. C. Lee, "MEMS-based series and shunt variable capacitors for microwave and millimeter-wave frequencies," *Sensors and Actuators*, vol. A. 91, pp. 256-265, 2001.
- [15] T. Morf, C. Biber, and W. Bachtold, "Systematic investigations on MESFETS and passive components transplanted by epitaxial lift off onto host materials with various resistivities," *IEEE MTT-S Int. Microwave Symposium*, pp. 1-4, 1997.
- [16] J. N. Burghartz, "Progress in RF inductors on silicon—understanding substrate losses," *Techn. Dig. IEDM*, pp. 523-526, 1998.
- [17] A. M. Niknejad, R. Gharpurey, and R. G. Meyer, "Numerically stable Green function for modeling and analysis of substrate coupling in integrated circuits," *IEEE Trans. Computer-aided Design of Integrated Circuits and Systems*, vol. 17, no. 4, pp. 305-315, 1998.
- [18] A. M. Niknejad and R. G. Meyer, "Analysis of Eddy-current losses over conductive substrates with applications to monolithic inductors and transformers," *IEEE Trans. Microwave Theory and Techniques*, vol. 49, no. 1, pp. 166-176, 2001.
- [19] S. Hara, T. Tokumitsu, T. Tanaka, and M. Aikawa, "Broad-band monolithic microwave active inductor and its application to miniaturized wide-band amplifiers," *IEEE Trans. Microwave Theory and Techniques*, vol. 36, no. 12, pp. 1920-1924, 1988.
- [21] G. F. Zhang, M. L. Villegas, and C. S. Ripoll, "New broadband tunable monolithic microwave floating active inductor," *Electron. Lett.*, vol. 28, no. 1, pp. 78-81, 1992.
- [22] R. Kaunisto, P. Alinikula, and K. Stadius, "Active inductors for GaAs and bipolar technologies," *Analog Integrated Circuits and Signal Processing*, vol. 7, pp. 35-48, 1995.
- [23] H. Hayashi, M. Muraguchi, Y. Umeda, and T. Enoki, "A high-q broad-band active inductor and its application to a low-loss analog phase shifter," *IEEE Trans. Microwave Theory and Techniques*, vol. 44, no. 12, pp. 2369-2374, 1996.
- [24] S. Stalf, "Printed inductors in RF consumer applications," *IEEE Trans. Consumer Electronics*, vol. 47, no. 3, pp. 426-, 2001.
- [25] N. M. Nguyen and R. G. Mayer, "Si IC-compatible inductors and LC passive filters," *IEEE J. Solid-State Circuits*, vol. 25, no. 4, pp. 1028-31, 1990.

- [26] J. N. Burghartz, D. C. Edelstein, K. A. Jenkins, C. Jahnes, C. Uzoh, E. J. O'Sullivan, K. K. Chan, M. Soyuer, P. Roper, and S. Cordes, "Monolithic spiral inductors fabricated using a VLSI Cu-damascene interconnect technology and low-loss substrates," *IEEE Techn. Dig. IEDM*, pp. 451-454, 1996.
- [27] C. M. Nam and Y. S. Kwon, "High-performance planar inductor on thick oxidized porous silicon (OPS) substrate," *IEEE Microwave and Guided Wave Letters*, vol. 7, no. 8, pp. 236-238, 1997.
- [28] J. N. Burghartz, M. Soyuer, and K. A. Jenkins, "Integrated RF and microwave components in BiCMOS technology," *IEEE Trans. Electron Devices*, vol. 43, no. 9, pp. 1559-70, 1996.
- [29] J. Y. C. Chang, A. A. Abidi, and M. Gaitan, "Large suspended inductors on silicon and their use in a 2- $\mu$ m CMOS RF amplifier," *IEEE Electron Device Letters*, vol. 14, no. 5, pp. 246-248, 1993.
- [30] A. Rofougaran, J. Y. C. Chang, M. rofougaran, and A. A. Abidi, "A 1 GHz CMOS RF front-end IC for a direct-conversion wireless receiver," *IEEE J. Solid-State Circuits*, vol. 31, no. 7, pp. 880-889, 1996.
- [31] R. P. Ribas, J. Lescot, J. L. Leclercq, N. bennouri, J. M. Karam, and B. Courtois, "Micromachined planar spiral inductor in standard GaAs HEMT MMIC technology," *IEEE Electron Device Letters*, vol. 19, no. 8, pp. 285-287, 1998.
- [32] J.-B. Yoon, C.-H. Han, E. Yoon, and C.-K. Kim, "Monolithic high-Q overhang inductors fabricated on silicon and glass substrates," *IEEE Techn. Dig. IEDM*, pp. 753-755, 1999.
- [33] J. Y. Hsu, H. C. Lin, H. D. Shen, and C. J. Chen, "High frequency multilayer chip inductors," *IEEE Trans. Magnetics*, vol. 33, no. 5, pp. 3325-3327, 1997.
- [34] Y.-J. Kim and M. G. Allen, "Surface micromachined solenoid inductors for high frequency applications," *IEEE Trans. Components, Packaging, and Manufacturing Technology, Part C*, vol. 21, no. 1, pp. 26-33, 1998.
- [35] J.-B Yoon, B.-K. Kim, C.-H. Han, E. Yoon, and C.-K. Kim, "Surface micromachined solenoid on-Si and on-glass inductors for RF applications," *IEEE Electron Device Letters*, vol. 20, no. 9, pp. 487-489, 1999.
- [36] H.-Y. Lee, Y.-G. Lee, S.-J. Kim, and S.-K. Yun, "Novel high-Q solenoid inductor using bondwires for GaAs monolithic microwave integrated circuits (MMICs)," *Jpn. J. Appl. Phys.*, vol. 38, pp. L1523-L1524, 1999.
- [37] B. Loechel, "Thick-layer resists for surface micromachining," *J. Micromech. Microeng.*, vol. 10, pp. 108-115, 2000.

- [38] H. Lorenz, M. Despont, N. Fahrmi, N. LaBianca, P. Renaud, and P. Vettiger, "SU-8: a low-cost negative resist for MEMS," *J. Micromech. Microeng.*, vol. 7, pp. 121-124, 1997.
- [39] L. Dellmann, S. Roth, C. Beuret, G. A. Racine, H. Lorenz, M. Despont, P. Renaud, P. Vettiger, and N. F. de Rooij, "Fabrication process of high aspect ratio elastic and SU-8 structures for piezoelectric motor applications," *Sensors and Actuators*, vol. A 70, pp. 42-47, 1998.
- [40] D. A. Fletcher, K. B. Crozier, K. W. Guarini, S. C. Minne, G. S. Kino, C. F. Quate, and K. E. Goodson, "Microfabricated silicon solid immersion lens," *J. Microelectromechanical Systems*, vol. 10, no. 3, pp. 450-459, 2001.
- [41] Y. S. Lin, C. T. Pan, K. L. Lin, S. C. Chen, J. J. Yang, and J. P. Yang, "Polyimide as the pedestal of batch fabricated micro-ball lens and micro-mushroom array category: micro opto electro mechanical systems," *IEEE Micro Electro Mechanical Systems Conference Tech. Dig.*, pp. 337-340, 2001.
- [42] P. Rangsten, H. Bjorkman, and K. Hjort, "Microfluidic components in diamond," *The 10<sup>th</sup> International Conference on Solid-state Sensors and Actuators, Transducer'99 digest of Technical Papers*, vol. 1, pp. 190-193, 1999.
- [43] S. Linder, "*Chip stacks for memory applications*," Doctoral dissertation, Swiss Federal institute of Technology Zurich, 1996.
- [44] P. Kersten, S. Bouwstra, and J. W. Peterson, "Photolithography on micromachined 3D surfaces using electrodeposited photoresist," *Sensors and Actuators*, vol. A 51, pp. 51-54, 1995.
- [45] M. Heschel, and S. Bouwstra, "Conformal coating by photoresist of sharp corners of anisotropically etched through-holes in silicon," *Sensors and Actuators*, vol. A 70, pp. 75-80, 1998.
- [46] S. Linder, "*S-parameter techniques for faster, more accurate network design*," HP application note 95-1, Hewlett Packard, 1996.
- [47] P. Arcioni, R. Castello, G. D. Astis, E. Sacchi, and F. Svelto, "Measurement and modeling of Si integrated inductors," *IEEE Trans. Instrumentation and Measurement*, vol. 47, no. 5, pp. 1372-1378, 1998.
- [48] P. J. van Wijnen, H. R. Claessen, and E. A. Wolsheimer, "A new straightforward calibration and correction procedure for on wafer high frequency S-parameters measurements (45 MHz – 18 GHz)," *IEEE Bipolar/BiCMOS Circuits and Technology Meeting Proc.*, pp. 70-73, 1987.



- [49] A. . Niknejad, and R. G. Meyer, "Analysis, design, and optimization of spiral inductors and transformers for Si RF IC's," *IEEE J. Solid-State Circuits*, vol. 33, no. 10, pp. 1470-1481, 1998.
- [50] D. Thorson, "A review of ABCD parameters," *Applied Microwave and Wireless*, May, pp. 55-58, 1999.
- [51] C. P. Yue, and S. S. Wong, "On-chip spiral inductors with patterned ground shields for Si-based RF IC's," *IEEE Journal of Solid-State Circuits*, vol. 33, no. 5, 1998, pp. 743-752.
- [52] C. P. Yue, and S. S. Wong, "Physical modeling of spiral inductors on silicon," *IEEE Trans. Electron Devices*, vol. 47, no. 3, pp. 560-568, 1998.
- [53] K. B. Ashby, I. A. Koullias, W. C. Finley, J. J. Bastek, and S. Moinian, "High Q inductors for wireless applications in a complementary silicon bipolar process," *IEEE Journal of Solid-State Circuits*, vol. 31, no. 1, pp. 4-9, 1996.
- [54] Avant corporation, "*Star-HSPICE manual*," Chapter 11, Release 1997.2, pp. 11.1-11.42, 1997.
- [55] A. R. Kral, "A 2.4 GHz frequency synthesizer in 0.6 $\mu$ m CMOS," M.S. thesis, University of California Los Angeles, 1998.
- [56] F. Langford-Smith (ed), "Radiotron designer's handbook," 4<sup>th</sup> edition, The Wireless Press, Sydney, Australia, 1952.
- [57] H. M. Greenhouse, "Design of planar rectangular microelectronic inductors," *IEEE Tran. Parts, Hybrids, and Packaging*, vol. PHP-10, no. 2, pp. 101-109, 1974.
- [58] Quadtech Inc., "*Multi-terminal impedance measurements, or... why do those bridges use so many connections?*," Application Note, November, 2000.
- [59] S. S. Mohan, M. M. Hershenson, S. P. Boyd, and T. H. Lee, "Simple accurate expressions for planar spiral inductances," *IEEE J. Solid-State Circuits*, vol. 34, no. 10, pp. 1419-1424, 1999.

## APPENDIX A

### PROCESS SEQUENCES OF SUSPENDED ON-CHIP ARCH-LIKE SOLENOID INDUCTOR

This appendix contains the detailed process sequences used in fabrication of the suspended on-chip arch-like solenoid inductor in chapter 4.

1. Clean Si wafer with TCE, acetone, methanol, and DI water.
2. Oxidize Si wafer to obtain 500 nm thick SiO<sub>2</sub> layer.
3. Deposit 10 nm Cr / 150 nm Cu / 10 nm Cr plating base.
4. Spin-coat a layer of 30  $\mu$ m thick SU-8 2025 at 3000 rpm for 30 seconds, remove the edge bead manually.
5. Soft-bake the wafer in an oven at 65 °C for 2 minutes and at 95 °C for 6 minutes, and cooled down naturally on an insulator.
6. Expose UV light on SU-8 layer with 236 mJ/cm<sup>2</sup> dose through mask no. 1 for substrate spacers.
7. Post-exposure bake the sample the same conditions as in step 5.
8. Develop the substrate spacer patterns in Nano SU-8 developer for 1.5 minutes, wash the sample in isopropanol, rinse in DI water and naturally dry in air.
9. Clean the SU-8 molds by RIE in 100 % O<sub>2</sub> plasma at 100 mTorr and 100 W RF power for 6 minutes.
10. Remove topmost Cr layer of the plating base in a solution of 20g : 20g : 100 ml of NaOH : K<sub>3</sub>Fe(CN)<sub>6</sub> : H<sub>2</sub>O and electroplate copper to fill up the molds.
11. Deposit a new Cu plating base as in step 3.

12. Fabricate another layer of SU-8 as in step 4-10 with mask no. 2 for bottom conductor.
13. Spin-coat a layer of 30  $\mu\text{m}$  thick SJR5740 at 750 rpm for 30 seconds.
14. Soft-bake SJR5740 layer in an oven by ramping the temperature from 50  $^{\circ}\text{C}$  to 95  $^{\circ}\text{C}$ , bake at 95  $^{\circ}\text{C}$  for one hour and naturally cool the sample down on an insulator outside the oven.
15. Expose UV light on SJR5740 layer with 322  $\text{mJ}/\text{cm}^2$  dose through mask no. 3 for photoresist mesa.
16. Develop the photoresist mesa patterns in MF354 developer for 28 minutes, rinse the sample in DI water, and dry naturally in air.
17. Expose the sample to acetone vapor with acetone concentration 1.66  $\mu\text{l}$  per 1 ml of air in a closed container on a hot plate at 50  $^{\circ}\text{C}$  for 1 minute.
18. Reflow the photoresist mesa on a hot plate at 95  $^{\circ}\text{C}$  for 5 minutes.
19. Hard-bake the photoresist mesa on a hot plate at 120  $^{\circ}\text{C}$  for 4 hours.
20. Hard-bake the photoresist mesa on a hot plate at 150  $^{\circ}\text{C}$  for 15 minutes and naturally cool down the sample.
21. Deposit 10 nm Cr / 300 nm Cu plating base on the photoresist mounds.
22. Electroplate a 16  $\mu\text{m}$  thick EAGLE2100 photoresist in an electroplating bath containing 666 ml Eagle2100 and 333 ml DI water at room temperature with 300 rpm stirring by biasing the sample with 40 VDC (anode to electrode plate and cathode to the sample).
23. Gently rinse the sample in DI water and naturally dry it in air.
24. Dry EAGLE2100 layer in vacuum below 100 mTorr for 4 hours.
25. Expose UV light on EAGLE2100 layer with 208  $\text{mJ}/\text{cm}^2$  dose through mask no. 4 for top conductor.
26. Without post-exposure baking, gently develop top conductor patterns in a 1:24 diluted

solution of EAGLE2005 developer and DI water at 38 °C for 2 minutes 30 seconds, gently rinsed in DI water, and naturally dry in air.

27. Clean EAGLE2100 photoresist mold by reactive ion etching in oxygen for at least 20 minutes at 200 W RF power and 200 mTorr pressure.
28. Clean copper plating base with 10 % sulfuric acid and electroplate copper to fill up the molds.
29. Wash out Eagle2100 molds by acetone and methanol.
30. Remove Eagle2100 mold residue by RIE with 10% CF<sub>4</sub> in O<sub>2</sub> at 200 mTorr and 350 W RF power for 15 minutes.
31. Remove top conductor Cu plating base layer in a solution of 1:1:20 H<sub>2</sub>SO<sub>4</sub>:H<sub>2</sub>O<sub>2</sub>:H<sub>2</sub>O.
32. Remove Cr layer in a solution of 20g : 20g : 100 ml of NaOH : K<sub>3</sub>Fe(CN)<sub>6</sub> : H<sub>2</sub>O.
33. Wash out SJR5740 sacrificial core by acetone and methanol, rinse in DI water and naturally dry in air.
34. Remove SJR5740 sacrificial core residue by RIE with 10% CF<sub>4</sub> in O<sub>2</sub> at 200 mTorr and 350 W RF power for 30 minutes.
35. Remove Cr layer with the same etchant as in step no. 32.
36. Remove bottom conductor Cu plating base as in step no. 31.
37. Etch SU-8 molds by RIE with 10% CF<sub>4</sub> in O<sub>2</sub> at 200 mTorr and 350 W RF power.
38. Remove the last Cu plating base as in step no. 31.
39. Perform high frequency measurements and modeling.

## APPENDIX B

### PROCESS SEQUENCES OF SUSPENDED ON-CHIP DOME-SHAPED SPIRAL INDUCTOR

This appendix contains the detailed process sequences used in fabrication of the suspended on-chip dome-shaped spiral inductor in chapter 5.

1. Clean Si wafer with TCE, acetone, methanol, and DI water.
2. Oxidize Si wafer to obtain 500 nm thick SiO<sub>2</sub> layer.
3. Deposit 10 nm Cr / 150 nm Cu / 10 nm Cr plating base.
4. Spin-coat a layer of 30  $\mu$ m thick SU-8 2025 at 3000 rpm for 30 seconds, remove the edge bead manually.
5. Soft-bake the wafer in an oven at 65 °C for 2 minutes and at 95 °C for 6 minutes, and cooled down naturally on an insulator.
6. Expose UV light on SU-8 layer with 236 mJ/cm<sup>2</sup> dose through mask no. 1 for substrate spacers.
7. Post-exposure bake the sample the same conditions as in step 5.
8. Develop the substrate spacer patterns in Nano SU-8 developer for 1.5 minutes, wash the sample in isopropanol, rinse in DI water and naturally dry in air.
9. Clean the SU-8 molds by RIE in 100 % O<sub>2</sub> plasma at 100 mTorr and 100 W RF power for 6 minutes.
10. Remove topmost Cr layer of the plating base in a solution of 20g : 20g : 100 ml of NaOH : K<sub>3</sub>Fe(CN)<sub>6</sub> : H<sub>2</sub>O and electroplate copper to fill up the molds.
11. Spin-coat a layer of 36  $\mu$ m thick SJR5740 at 500 rpm for 30 seconds.

12. Soft-bake SJR5740 layer in an oven by ramping the temperature from 50 °C to 95 °C, bake at 95 °C for one hour and naturally cool the sample down on an insulator outside the oven.
13. Expose UV light on SJR5740 layer with 498 mJ/cm<sup>2</sup> dose through mask no. 2 for photoresist mesa.
14. Develop the photoresist mesa patterns in MF354 developer for 32 minutes, rinse the sample in DI water, and dry naturally in air.
15. Expose the sample to acetone vapor with acetone concentration 1.66 µl per 1 ml of air in a closed container on a hot plate at 50 °C for 1 minute.
16. Reflow the photoresist mesa on a hot plate at 95 °C for 5 minutes.
17. Hard-bake the photoresist mesa on a hot plate at 120 °C for 4 hours.
18. Hard-bake the photoresist mesa on a hot plate at 150 °C for 15 minutes and naturally cool down the sample.
19. Deposit 10 nm Cr / 300 nm Cu plating base on the photoresist mounds.
20. Electroplate a 16 µm thick EAGLE2100 photoresist in an electroplating bath containing 666 ml Eagle2100 and 333 ml DI water at room temperature with 300 rpm stirring by biasing the sample with 40 VDC (anode to electrode plate and cathode to the sample).
21. Gently rinse the sample in DI water and naturally dry it in air.
22. Dry EAGLE2100 layer in vacuum below 100 mTorr for 4 hours.
23. Expose UV light on EAGLE2100 layer with 208 mJ/cm<sup>2</sup> dose through mask no. 3 for spiral conductor.
24. Without post-exposure baking, gently develop top conductor patterns in a 1:24 diluted solution of EAGLE2005 developer and DI water at 38 °C for 2 minutes 30 seconds, gently rinsed in DI water, and naturally dry in air.

25. Clean EAGLE2100 photoresist mold by reactive ion etching in oxygen for at least 20 minutes at 200 W RF power and 200 mTorr pressure.
26. Clean copper plating base with 10% sulfuric acid and electroplate copper to fill up the molds.
27. Remove Eagle2100 mold residue by RIE with 10%  $\text{CF}_4$  in  $\text{O}_2$  at 200 mTorr and 150 W RF power for three hours.
28. Remove the old Cu plating base layer in a solution of 1:1:20  $\text{H}_2\text{SO}_4$ : $\text{H}_2\text{O}_2$ : $\text{H}_2\text{O}$ , and deposit the new one as in step 3.
29. Spin-coat a layer of 85  $\mu\text{m}$  thick SU-8 2075 at 3000 rpm for 30 seconds, remove the edge bead manually.
30. Soft-bake the wafer in an oven at 65 °C for 6 minutes and at 95 °C for 18 minutes, and cooled down naturally on an insulator.
31. Expose UV light on SU-8 layer with 423  $\text{mJ}/\text{cm}^2$  dose through mask no. 4 for long via.
32. Post-exposure bake the wafer in an oven at 65 °C for 2 minutes and at 95 °C for 14 minutes, and cooled down naturally on an insulator.
33. Develop the substrate spacer patterns in Nano SU-8 developer for 7 minutes, wash the sample in isopropanol, rinse in DI water and naturally dry in air.
34. Clean the SU-8 molds by RIE in 100%  $\text{O}_2$  plasma at 100 mTorr and 100 W RF power for 6 minutes.
35. Remove topmost Cr layer of the plating base in a solution of 20g : 20g : 100 ml of  $\text{NaOH} : \text{K}_3\text{Fe}(\text{CN})_6 : \text{H}_2\text{O}$  and electroplate copper to fill up the molds.
36. Deposit 500 nm Al layer, spin-on coat a 1.5  $\mu\text{m}$  thick SU-8 2002 at 3000 rpm for 30 seconds.
37. Soft-bake the wafer in an oven at 65 °C for 1 minute and at 95 °C for 2 minutes, and cooled down naturally on an insulator.

38. Expose UV light on SU-8 layer with  $95 \text{ mJ/cm}^2$  dose through mask no. 5 for short via.
39. Post-exposure bake the wafer in an oven at  $65^\circ\text{C}$  for 1 minute and at  $95^\circ\text{C}$  for 2 minutes, and cooled down naturally on an insulator.
40. Develop the substrate short via pattern in Nano SU-8 developer for 30 seconds, wash the sample in isopropanol, rinse in DI water and naturally dry in air.
41. Clean the SU-8 window opening by RIE in 100%  $\text{O}_2$  plasma at 100 mTorr and 100 W RF power for 6 minutes and etch Al layer through SU-8 window opening.
42. Form a short via hole by reactive ion etching through the patterned Al mask in 10%  $\text{CF}_4$  and 90%  $\text{O}_2$  with 365 W RF power until the hole reaches the center of spiral conductor.
43. Remove topmost Cr layer of the plating base in a solution of 20g : 20g : 100 ml of  $\text{NaOH} : \text{K}_3\text{Fe}(\text{CN})_6 : \text{H}_2\text{O}$  and electroplate copper to fill up short via hole.
44. Form the air bridge by repeating step 3-10 using mask no. 5.
45. Remove all photoresist structures by RIE with 10%  $\text{CF}_4$  in  $\text{O}_2$  at 200 mTorr and 350 W RF power and remove all Cr layers of the plating base in a solution of 20g : 20g : 100 ml of  $\text{NaOH} : \text{K}_3\text{Fe}(\text{CN})_6 : \text{H}_2\text{O}$  and all Cu layers in a solution of 1:1:20  $\text{H}_2\text{SO}_4:\text{H}_2\text{O}_2:\text{H}_2\text{O}$ .
46. Perform high frequency measurements and modeling.



## APPENDIX C

### MODELING MATLAB SOURCE CODES

This appendix contains the Matlab source codes used in modeling of inductors by the modeling methods described in chapter 3.

```
% #####  
% # Matlab program indmodel.m reads S-parameter files in  
% # CITIFILE format generated by Agilent 8510C vector network analyzer.  
% #  
% # It performs the following functions:  
% # - Converts S-parameters files of inductor with pads (DUT) and of pads  
% # only (PAD) on-wafer devices into Touchstone real-imaginary files  
% # *.s1p or *.s2p.  
% # - Converts S-parameters of DUT and of PAD into Y-parameters, subtracts  
% # Y-parameters of PAD out of that of DUT (parasitic de-embedding).  
% # - Converts de-embedded Y-parameters into de-embedded S-parameters and  
% # save in *.s1p or *.s2p.  
% # - For 2-port devices: the de-embedded Y-parameter data are used to  
% # extract RLC values of its 2-port equivalent lump circuit pi-network  
% # model and save the results to an output file *.mod.  
% #  
% # Written by Nimit Chomnawang, April 13, 2002.  
% #####  
% indmodel.m
```

```
global fhz;
```

```
warning off
```

```
% Show fuchtions of this program to screen.  
s1=sprintf('#####');  
s2=sprintf('# Matlab program indmodel.m reads 1-port or 2-port');  
s3=sprintf('# S-parameter files in CITIFILE format generated by Agilent');  
s4=sprintf('# 8510C vector network analyzer.\n#');  
s5=sprintf('# It performs the following functions:');  
s6=sprintf('# - Converts S-parameters files of inductor with pads (DUT));  
s7=sprintf('# and of pads only (PAD) on-wafer devices into Touchstone');  
s8=sprintf('# real-imaginary files *.s1p or *.s2p.');
```

```

s9=sprintf('# , subtracts Y-parameters of PAD out of that of DUT');
s10=sprintf('# (parasitic de-embedding).');
s11=sprintf('# - Converts de-embedded Y-parameters into de-embedded');
s12=sprintf('# S-parameters and save in *.s1p or *.s2p. ');
s13=sprintf('# - For 2-port devices: de-embedded Y-parameter data are');
s14=sprintf('# used to extract RLC values of its 2-port equivalent');
s15=sprintf('# lump circuit pi-network model and save the results to');
s16=sprintf('# an output file *.mod.\n#');
s17=sprintf('# Written by Nimit Chomnawang, April 17, 2002. ');
s18=sprintf('#####\n');
disp(s1);disp(s2);disp(s3);disp(s4);disp(s5);disp(s6);disp(s7);disp(s8);
disp(s9);disp(s10);disp(s11);disp(s12);disp(s13);disp(s14);disp(s15);
disp(s16);disp(s17);disp(s18);

```

```

% Get input filename from keyboard
dutfileprefix = ...
input('Enter the filename of DUT CITIFILE input (no extension): ','s');
padfileprefix = ...
input('Enter the filename of PAD CITIFILE input (no extension): ','s');
dmbfileprefix = ...
input('Enter the filename of output (no extension): ','s');

```

```

% Read input S-parameters in CITIFILE format and convert to Touchstone
% real-imaginary format. This applies to both DUT and PAD. The results
% are stored in dutmatrix and padmatrix.
dutmatrix = citi2touches(dutfileprefix);
padmatrix = citi2touches(padfileprefix);

```

```

% Check if data obtained are valid.
if (size(dutmatrix,2)>3) % check number of ports
    portnum = 2;
else
    portnum = 1;
    if (size(dutmatrix)~=size(padmatrix))% Check if DUT and PAD are matched.
        disp('Number of data points in the DUT and PAD are is not equal!');
        return;
    end % if
end; % if size

```

```

% Set plot size of graphs.
pc = input('Enter plot size of graphs (in % of full screen, default=50):');
if (isempty(pc)) % if return key was pressed so that pc = empty matrix
    pc = 50;

```

```

end %if pc

% Set plot size of Smith Charts
pcs = input('Enter plot size of Smith charts (in % of full screen, default=30):');
if (isempty(pcs)) % if return key was pressed so that pcs = empty matrix
    pcs = 30;
end %if pcs

% Determine frequency matrix and number of data points.
f = dutmatrix(:,1); % All data in column 1 are f
% vectorize frequency matrix and make frequency unit in Hz.
fhz = f(:).*(1E+9);
% Number of data points is number of elements of matrix f
pointnum=size(f);

% Perform de_embedding, save de-embedded S-parameters to files store
% de-embedded S and Y parameters in matrix s and y.
[dmbs,dmby] = de_embed(dutmatrix,padmatrix,dmbfileprefix);

% Find coefficients of the equation that fit the curve of measured
% S-parameters.

% Read initial guess values, lower limits and upper limits values
% of model parameters from two-port configuration file twoportconfig.m.
% Modify this file to your own values.
cfg = fopen('twoportconfig.m','r'); % open two-port configuration file.

% Ignore first twelve lines
ig=fgetl(cfg);ig=fgetl(cfg);ig=fgetl(cfg);
ig=fgetl(cfg);ig=fgetl(cfg);ig=fgetl(cfg);
ig=fgetl(cfg);ig=fgetl(cfg);ig=fgetl(cfg);
ig=fgetl(cfg);ig=fgetl(cfg);ig=fgetl(cfg);

% Read lower limit.
s = fgetl(cfg);
P = sscanf(s,'%s %f %f %f %f %f %f %f %f %f %f %f %s');
lb = [P(2) P(3) P(4) P(5) P(6) P(7) P(8) P(9) P(10) P(11) P(12)];
s = fgetl(cfg);
P = sscanf(s,'%s %f %f %f %f %f %f %f %f %f %f %f %s');
guess = [P(2) P(3) P(4) P(5) P(6) P(7) P(8) P(9) P(10) P(11) P(12)];
s = fgetl(cfg);
P = sscanf(s,'%s %f %f %f %f %f %f %f %f %f %f %f %s');
ub = [P(2) P(3) P(4) P(5) P(6) P(7) P(8) P(9) P(10) P(11) P(12)];

```

```

fclose(cfg);

% Call curve fitting for two-port
dp = sprintf("\nOptimizing two-port model parameters, please wait ...\n");
disp(dp);
[ysmea,ysfit,y1mea,y1fit,y2mea,y2fit,smea,sfit,zinmea,zinfit,rsfit] = ...
    twoportfit(dmbs,guess,lb,ub,dmbfileprefix);

% Plot charts of Ys, Yp, S11,S21 and Q
twoportplot(ysmea,ysfit,y1mea,y1fit,y2mea,y2fit,smea,sfit,zinmea,zinfit,rsfit,f,dmbfileprefix,pc);

dutfilename=strcat(dutfileprefix,'.s2p');
padfilename=strcat(padfileprefix,'.s2p');
dmbfilename=strcat(dmbfileprefix,'.s2p');
fitfilename=strcat(dmbfileprefix,'fit.s2p');

% Plot Smith charts of em-bedded S-paramters.
smithplot(portnum,dutfilename,'n',pcs,1,'DUT S-parameters');
smithplot(portnum,padfilename,'n',pcs,2,'PAD S-parameters');

% Plot de-embedded S-parameters in Smith chart.
smithplot(portnum,dmbfilename,'n',pcs,3,'De-embedded S-parameters');

% Plot measured and modeled S-parameters in Smith chart.
c = 'Measured and Modeled S-parameters';
smithplot(portnum,dmbfilename,fitfilename,pcs,4,c);

return;

```

```

% #####
% # Matlab function citi2touches.m reads a file in CITIFILE format generated
% # by Agilent 8510C vector network analyzer, converts it into a Touchstone
% # file in real-imaginary format, save the results in *.s1p or *.s2p file
% # and return S-parameter matrix back to to calling program.
% #
% # Written by Nimit Chomnawang, April 17, 2002.
% #####
% citi2touches.m

function sparam = citi2touches(fileprefix)

filename = strcat(fileprefix, '.txt'); % Input file extension is .txt
s=sprintf('\nReading CITIFILE S-parameters from file %s ...',filename);
disp(s);
citifile = fopen(filename, 'r'); % open input citifile file.

% Ignore first five lines
ignore = fgetl(citifile); ignore = fgetl(citifile); ignore = fgetl(citifile);
ignore = fgetl(citifile); ignore = fgetl(citifile);

% Ignore next line
ignore = fgetl(citifile);

% Read next line
s = fgetl(citifile);
if (s=='DATA S[2,1] RI')
    portnum=2;
    filename = strcat(fileprefix, '.s2p');
    % Skip next three lines
    ignore = fgetl(citifile); ignore = fgetl(citifile);
    ignore = fgetl(citifile);
else
    portnum=1;
    filename = strcat(fileprefix, '.s1p');
end; % s==

% Read next line
s = fgetl(citifile);
P = sscanf(s, '%s %f %f %f');
fstart = P(4)/1E+9; % f in GHz
fstop = P(5)/1E+9;
pointnum = P(6);

```

```

% Ignore next four lines
ignore = fgetl(citifile);ignore = fgetl(citifile);
ignore = fgetl(citifile);ignore = fgetl(citifile);

fstep = (fstop-fstart) ./ (pointnum-1);
f = fstart:fstep:fstop;

% Read S11;
for i=1:pointnum;
    % Read real-imaginary data line by line.
    s = fgetl(citifile);
    P = sscanf(s,'%f,%f');
    re11(i) = P(1);
    im11(i) = P(2);
end;

% Open output file
outfile = fopen(filename,'w'); % Open output TouchStone file.

% Write output file header
fprintf(outfile,'# GHz S RI R 50\n');

% If 1-port, write data to Touchstone file.
if (portnum==1)
    sparam = [f' re11' im11'];
    s=sprintf('Writing Touchstone S-parameters to file %s...',filename);
    disp(s);
    fprintf(outfile,'%f %f %f\n',sparam);
end; % end portnum==1

% If 2-port, read S21 S12 S22
if (portnum==2)

    % Ignore next two lines
    ignore = fgetl(citifile);ignore = fgetl(citifile);

    % Read S21;
    for i=1:pointnum;
        % Read real-imaginary data line by line.
        s = fgetl(citifile);
        P = sscanf(s,'%f,%f');
        re21(i) = P(1);

```

```

        im21(i) = P(2);
    end; % for i

    % Ignore next two lines
    ignore = fgetl(citifile);ignore = fgetl(citifile);

    % Read S12;
    for i=1:pointnum;
        % Read real-imaginary data line by line.
        s = fgetl(citifile);
        P = sscanf(s,'%f,%f');
        re12(i) = P(1);
        im12(i) = P(2);
    end; % for i

    % Ignore next two lines
    ignore = fgetl(citifile);ignore = fgetl(citifile);

    % Read S22;
    for i=1:pointnum;
        % Read real-imaginary data line by line.
        s = fgetl(citifile);
        P = sscanf(s,'%f,%f');
        re22(i) = P(1);
        im22(i) = P(2);
    end; % for i

    sparam = [f' re11' im11' re21' im21' re12' im12' re22' im22'];

    % Print data to Touchstone file.
    s=sprintf('Writing TouchStone S-parameters to file %s ...',filename);
    disp(s);
    fprintf(outfile,'%f %f %f %f %f %f %f %f %f %f\n',sparam');

end; % if portnum==2

% Close files
fclose(outfile);
fclose(citifile);

return;

```

```

% #####
% # Matlab function de-embed.m converts S-paramters of DUT and PAD to
% # Y-parameters. Subtract Y of PAD from Y of DUT and store de-embedded
% # Y-parameters in dmby. De-embedded Y-parameters are converted back to
% # S-parameters. De-embedded S-parameters are stored in dmbs and saved to
% # an S-parameter file outfile.s1p or *.s2p.
% #####
% de_embed.m

function [dmbs,dmby] = de_embed(dut,pad,dmbfileprefix)

% Determine frequency matrix and number of data points.
f = dut(:,1); % All data in column 1 are f
% Number of data points is number of elements of matrix f
pointnum=size(f);

% Determin number of ports
if (size(dut,2)>3) % check number of ports
    portnum = 2;
else
    portnum = 1;
end;

% Define S11
duts11 = dut(:,2) + sqrt(-1).*dut(:,3);
pads11 = pad(:,2) + sqrt(-1).*pad(:,3);

if (portnum==1)

    % Convert S to Y and find Yin1P
    %  $Y_{in} = [1/Z_0] * [(1-S_{11}) / (1+S_{11})]$ 
    yindut = ((1-duts11)./(1+duts11))./50; %  $Z_0 = 50 \text{ Ohm}$ .
    yinpad = ((1-pads11)./(1+pads11))./50; %  $Z_0 = 50 \text{ Ohm}$ .
    yin1p = yindut - yinpad;

    % Convert Yin1P back to S11
    %  $S_{11} = (1-Y*Z_0) / (1+Y*Z_0)$ 
    yin1p = yin1p.*50;
    s111p = (1-yin1p)./(1+yin1p); %  $Z_0 = 50 \text{ Ohm}$ .

```



```

% Write de-embedded S-parameter to output file.
filename = strcat(dmbfileprefix,'s1p');
outfile = fopen(filename,'w');
s = ...
sprintf('Writing de-embedded one-port S-parameter to %s ...',filename);
disp(s);
fprintf(outfile,'# GHz S RI R 50\n');
dmbsin = [f real(s11p) imag(s11p)];
fprintf(outfile,'%f %f %f\n',dmbsin);
fclose(outfile);

% Write de-embedded S-parameter to output file to be used by HSPICE.
filename = strcat(dmbfileprefix,'hspice.s1p');
o = fopen(filename,'w');
s = ...
sprintf('Writing de-embedded two-port S-parameter to %s ...',filename);
disp(s);
fprintf(o,'# Hz S MA R 50\n');
mgs11 = abs(s11p);
angs11 = 180.*angle(s11p)/pi;

dmbs = [f.*1E+9 mgs11 angs11];
fprintf(o,'%6.4e %6.4e %6.4e\n',dmbs);
fclose(o);

% Creat de-embedded S and Y parameter matrices
dmbs = [s11p];
dmby = [yin1p];

end; % if portnum==1

if (portnum==2)

% Define S21, S12, S22.
duts21 = dut(:,4) + sqrt(-1).*dut(:,5);
duts12 = dut(:,6) + sqrt(-1).*dut(:,7);
duts22 = dut(:,8) + sqrt(-1).*dut(:,9);

pads21 = pad(:,4) + sqrt(-1).*pad(:,5);

```

```

pads12 = pad(:,6) + sqrt(-1).*pad(:,7);
pads22 = pad(:,8) + sqrt(-1).*pad(:,9);

% Convert S of dut to Y
delta = ((1+duts11).*(1+duts22))-(duts12.*duts21);

duty11 = (((1-duts11).*(1+duts22)) + (duts12.*duts21))./delta./50; % Z0 = 50.
duty21 = ((-2.*duts21)./delta)./50; % Z0 = 50.
duty12 = ((-2.*duts12)./delta)./50; % Z0 = 50.
duty22 = (((1+duts11).*(1-duts22)) + (duts12.*duts21))./delta./50; % Z0 = 50.

% Convert S of pad to Y
delta = ((1+pads11).*(1+pads22))-(pads12.*pads21);

pady11 = (((1-pads11).*(1+pads22)) + (pads12.*pads21))./delta./50; % Z0 = 50.
pady21 = ((-2.*pads21)./delta)./50; % Z0 = 50.
pady12 = ((-2.*pads12)./delta)./50; % Z0 = 50.
pady22 = (((1+pads11).*(1-pads22)) + (pads12.*pads21))./delta./50; % Z0 = 50.

% De-embedding.
dmby11 = duty11 - pady11;
dmby21 = duty21 - pady21;
dmby12 = duty12 - pady12;
dmby22 = duty22 - pady22;

% Convert Y back to S.
y11 = dmby11 .* 50; % Normalize Y
y21 = dmby21 .* 50;
y12 = dmby12 .* 50;
y22 = dmby22 .* 50;

delta = ((1+y11).*(1+y22)) - (y12.*y21);

s11 = (((1-y11).*(1+y22)) + (y12.*y21))./delta;
s21 = (-2.*y21)./delta;
s12 = (-2.*y12)./delta;
s22 = (((1+y11).*(1-y22)) + (y12.*y21))./delta;

```

```

% Write de-embedded S-parameter to output file.
filename = strcat(dmbfileprefix, '.s2p');
outfile = fopen(filename, 'w');
s = ...
sprintf('Writing de-embedded two-port S-parameter to %s ...', filename);
disp(s);
fprintf(outfile, '# GHz S RI R 50\n');
dmbs2p = [f real(s11) imag(s11) real(s21) imag(s21) ...
          real(s12) imag(s12) real(s22) imag(s22)];
fprintf(outfile, '%f %f %f %f %f %f %f %f %f\n', dmbs2p);
fclose(outfile);

% Write de-embedded S-parameter to output file to be used by HSPICE.
filename = strcat(dmbfileprefix, 'hspice.s2p');
o = fopen(filename, 'w');
s = ...
sprintf('Writing de-embedded two-port S-parameter to %s ...', filename);
disp(s);
fprintf(o, '# Hz S MA R 50\n');
mgs11 = abs(s11);
mgs21 = abs(s21);
mgs12 = abs(s12);
mgs22 = abs(s22);
angs11 = 180.*angle(s11)./pi;
angs21 = 180.*angle(s21)./pi;
angs12 = 180.*angle(s12)./pi;
angs22 = 180.*angle(s22)./pi;

dmbs = [f.*1E+9 mgs11 angs11 mgs21 angs21 mgs12 angs12 mgs22 angs22];
fprintf(o, '%6.4e %6.4e %6.4e %6.4e %6.4e %6.4e %6.4e %6.4e %6.4e\n', dmbs);
fclose(o);

% Creat de-embedded S and Y parameter matrices
dmbs = [s11 s21 s12 s22];
dmby = [y11 y21 y12 y22];

end; % if portnum==2

return;

```

```

% #####
% # Matlab function smithplot.m reads a space de-limited S-parameters
% # from a real-imaginary Touchstone format file *.s1p or *.s2p and
% # plot S-parameters on a Smith chart.
% # -Input: One or two ports S-parameter (*.s1p or *.s2p) in
% #       real-imaginary Touchstone format
% # -Output: Smith chart on the Matlab screen.
% #
% # Synopsis:
% # smithplot(portnum,file1,file2,chartsize,fignum,figname)
% # where chartsize is 0-100.
% # ex: smithplot(2,'dummy.s2p','no',50,1,'S-parameters') is to plot
% # Smith chart from file dummy.s2p with no second input file, chart size
% # 50% of full screen, figure number 1 and figure name "S-parameters".
% #
% # Written by Nimit Chomnawang, April 17, 2002.
% #####
% smithplot.m

function out = smithplot(portnum,file1,file2,scsize,fignum,figname)

if (nargin ~= 6)
s1=sprintf('\nSynopsis:\n');
s2=sprintf('smithplot(portnum,file1,file2,chartsize,fignum,figname)');
s3=sprintf('where chartsize is 0-100. For example:');
s4=sprintf('smithplot(2,"dummy.s2p","no",50,1,"S-parameters")');
s5=sprintf('is to plot Smith chart from file dummy.s2p with chart size');
s6=sprintf('50%% of full screen, with figure number 1 and with figure');
s7=sprintf('name "S-parameters"');
disp(s1);disp(s2);disp(s3);disp(s4);disp(s5);disp(s6);disp(s7);
out = 0;
    return;
end; % if nargin

no = 'n';

pc = scsize; % Passing screen size to pc and check for valid chart size
if (pc<0 | pc >100)
s=sprintf('Invalid chart size!');

```

```

out = 0;
return;
end; % if pc

% Read f S RI from input file
sri1 = fopen(file1,'r'); % Open input file
firstline = fgetl(sri1); % Ignore the first line

if (portnum==1)
% Read 3 columns and any rows to matrix
A = fscanf(sri1,'%g %g %g\n',[3,inf]);
else
% Read 9 columns and any rows to matrix A
A = fscanf(sri1,'%g %g %g %g %g %g %g %g %g\n',[9,inf]);
end % if portnum==1

fclose(sri1);
A = A'; % Do transpose of A to put data in matrix row, column format

% Assign each column of matrix A to frequency and S-parameters
f = A(:,1); % Frequency
pointnum=size(f);

res11 = A(:,2); % Real of S11
ims11 = A(:,3); % Imaginary of S11
if (portnum==2)
res21 = A(:,4); % Real of S21
ims21 = A(:,5); % Imaginary of S21
res12 = A(:,6); % Real of S12
ims12 = A(:,7); % Imaginary of S12
res22 = A(:,8); % Real of S22
ims22 = A(:,9); % Imaginary of S22
end % if portnum==2

% Vectorize matrices
res11 = res11(:);
ims11 = ims11(:);

% Set chart size

```

```

scrsz = get(0,'ScreenSize');
figure(fignum);
set(fignum,'name',figname,'Position', ...
[10 10 scrsz(3).*pc./100 scrsz(4).*pc./100],'color',[1 1 1]);

% Define X and R circles
X=[0.2 0.5 1 2 5]; % Major scale grid
R=[0.2 0.5 1 2 5]; % Major scale grid

% To plot smooth circles with 101 points
theta=2*pi*(0:0.01:1);

% Draw a circle
patch(cos(theta),sin(theta),'-','edgecolor',[1 0.5 0],'facecolor','w');
hold on;
plot([-1 1],[0 0],'-','color',[1 0.5 0]);

% Plot major scale grids
for rr=R
xc=rr./(1+rr); % x position of the center
rd=1./(1+rr); % radius of the circle
% plot circles
plot(xc+rd*cos(theta),rd*sin(theta),'-','color',[1 0.5 0]);
end; % for rr

for xx=X
xc=1; % x position of the center
yc=1./xx; % y position of the center
rd=1./xx; % radius of the circle
theta_xx= 2*atan(xx)*(0:0.01:1);
plot(xc-rd*sin(theta_xx),yc-rd*cos(theta_xx),'-','color',[1 0.5 0]);
plot(xc-rd*sin(theta_xx),-yc+rd*cos(theta_xx),'-','color',[1 0.5 0]);
end; % for xx

% Annotate smith chart
for rr=R
xc=rr./(1+rr); % x position of the center
rd=1./(1+rr); % radius of the circle
text(xc-rd,-0.1,num2str(rr,'% .1f'), ...

```

```

'horizontalalignment','left','VerticalAlignment','bottom', ...
'Rotation',90,'color','k','fontsize',10);
end; % for rr
for xx=X
theta_xx= 2*atan(1./xx);
text(1.1*cos(theta_xx),1.1*sin(theta_xx),num2str(xx,'+J%.1f'), ...
'horizontalalignment','center','VerticalAlignment','middle','color', ...
'k','fontsize',10);
text(1.1*cos(theta_xx),-1.1*sin(theta_xx),num2str(xx,'-J%.1f'), ...
'horizontalalignment','center','VerticalAlignment','middle','color', ...
'k','fontsize',10);
end; % for xx
text(-1.1,0,'O','horizontalalignment','center','VerticalAlignment', ...
'middle','color','k','fontsize',10);
text(1.1,0,'\infty','horizontalalignment','center', ...
'VerticalAlignment','middle','color','k','fontsize',16);
axis image;
axis off;
text(0.99,-1.1,'Zo = 50 \Omega','horizontalalignment','center', ...
'VerticalAlignment','middle','color','k','fontsize',10);
hold off;

if (portnum==1)

if (~(strcmp(file2,no)))
% Read f S RI from input file
sri2 = fopen(file2,'r'); % Open input file
firstline = fgetl(sri2); % Ignore the first line

% Read 3 columns and any rows to matrix
A = fscanf(sri2,'%g %g %g\n',[3,inf]);
fclose(sri2);
A = A'; % Do transpose of A to put data in matrix row, column format

% Assign each column of matrix A to frequency and S-parameters
f = A(:,1); % Frequency
pointnum=size(f);

res11fit = A(:,2); % Real of S11

```

```

ims11fit = A(:,3); % Imaginary of S11

% Vectorize matrices
res11fit = res11fit(:);
ims11fit = ims11fit(:);

% Plot S11 of input file1
hold on;
j=1;
for i=1:3:pointnum
x(j)=res11(i);
y(j)=ims11(i);
j = j+1;
end; % for i

h=plot(x,y,res11fit,ims11fit);
legend(h,'Measured S11','Modeled S11');
set(h,{'LineStyle'},{'o','-'},'LineWidth',2 ...
    ,{'Color'},{'r','b'},'MarkerSize',5);
legend('boxoff');
hold off;
else
% Plot S11 of input file1
hold on;
j=1;
for i=1:3:pointnum
x(j)=res11(i);
y(j)=ims11(i);
j = j+1;
end; % for i
h=plot(x,y,'ob','markersize',4);
legend(h,'Measured S11');
legend('boxoff');
hold off;

end % if file2

end; % end if portnum==1

```



```

if (portnum==2)

if (~(strcmp(file2,no)))
% Read f S RI from input file
sri2 = fopen(file2,'r'); % Open input file
firstline = fgetl(sri2); % Ignore the first line

% Read 9 columns and any rows to matrix A
A = fscanf(sri2,'%g %g %g %g %g %g %g %g %g\n',[9,inf]);
fclose(sri2);

A = A'; % Perform transpose of A to put data in matrix row, column format

% Assign each column of matrix A to frequency and S-parameters
f = A(:,1); % Frequency
pointnum=size(f);

res11fit = A(:,2); % Real of S11
ims11fit = A(:,3); % Imaginary of S11
res21fit = A(:,4); % Real of S21
ims21fit = A(:,5); % Imaginary of S21
res12fit = A(:,6); % Real of S12
ims12fit = A(:,7); % Imaginary of S12
res22fit = A(:,8); % Real of S22
ims22fit = A(:,9); % Imaginary of S22

j=1;
for i=1:7:pointnum
x11(j)=res11(i);
y11(j)=ims11(i);
x21(j)=res21(i);
y21(j)=ims21(i);
x12(j)=res12(i);
y12(j)=ims12(i);
x22(j)=res22(i);
y22(j)=ims22(i);
j = j+1;
end % for i

```

```

% Plot Modeled S11 S22 S21 S12
hold on;
h=plot(x11,y11,x21,y21,x12,y12,x22,y22,res11fit,ims11fit, ...
      res21fit,ims21fit,res12fit,ims12fit,res22fit,ims22fit);
legend(h,'Measured S11','Measured S21','Measured S12','Measured S22', ...
      'Modeled S11','Modeled S21','Modeled S12','Modeled S22');
legend('boxoff');
set(h,{'LineStyle'},{'o';'s';'^';>';'h';'v';'x';'<'},'LineWidth', ...
     2,{'Color'},{'r';'b';'g';'k';'r';'b';'g';'k'},'MarkerSize',5);
hold off;
else
    % Plot Measured S11 S21 S12 S22
    j=1;
    for i=1:3:pointnum
        x11(j)=res11(i);
        y11(j)=ims11(i);
        x21(j)=res21(i);
        y21(j)=ims21(i);
        x12(j)=res12(i);
        y12(j)=ims12(i);
        x22(j)=res22(i);
        y22(j)=ims22(i);
        j = j+1;
    end % for i
    hold on;
    h=plot(x11,y11,'ob',x21,y21,'*k',x12,y12,'dm',x22,y22,'sr');
    legend(h,'Measured S11','Measured S21','Measured S12','Measured S22');
    legend('boxoff');
    hold off;

end % if file2

end; % end if portnum==2

out = 1;
return;

```

```

% #####
% # Matlab function twoportfit.m perform curve fitting to the magnitude
% # and angle of one-port S-parameter to extract one-port lump RLC
% # parameters of equivalent circuit of the inductor. The results are
% # saved to output file *.mod. The magnitude and angle of measured and
% # fitted S-parameter and impedance are passed out to the calling
% # program in order to plot data for comparisons.
% # Written by Nimit Chomnawang, April 17, 2002.
% #####
% twoportfit.m

function [ys,ysfit,yp1,y1fit,yp2,y2fit,smea,sfit,zinmea,zinfit,rsfit]= ...
    twoportfit(s,guess,lb,ub,dmbfileprefix)

global fhz;

% Obtain S and Y from input matrices
s11mea = s(:,1);
s21mea = s(:,2);
s12mea = s(:,3);
s22mea = s(:,4);
smea = [s11mea s21mea s12mea s22mea];

% Convert S to ABCD
Amea = (((1+s11mea).*(1-s22mea))+(s12mea.*s21mea))./(2.*s21mea);
Bmea = 50.*(((1+s11mea).*(1+s22mea))-(s12mea.*s21mea))./(2.*s21mea);
Cmea = (((1+s11mea).*(1+s22mea))-(s12mea.*s21mea))./(2.*s21mea)./50;
Dmea = (((1-s11mea).*(1+s22mea))+(s12mea.*s21mea))./(2.*s21mea);

filename = strcat(dmbfileprefix,'.abcd');
mdout = fopen(filename,'w');
s = sprintf('Writing ABCD matrix %s ...',filename);
disp(s);
fprintf(mdout,'# Hz reA imA reB imB reC imC reD imD\n');
md = [fhz real(Amea) imag(Amea) real(Bmea) imag(Bmea) ...
    real(Cmea) imag(Cmea) real(Dmea) imag(Dmea)];
fprintf(mdout,'%6.4e %6.4e %6.4e %6.4e %6.4e %6.4e %6.4e %6.4e %6.4e\n',md);
fclose(mdout);

% Find propagation constant Gamma and characteristic impedance Z0

```

```

tmp = (Amea+Dmea)./2;
gammal = acosh(tmp);
z0 = Bmea./sinh(gammal);
zp = (2.*z0)./gammal;
yp=1./zp;
zs = gammal.*z0;
ys = 1./zs;
y = yp+ys;
z = 1./y;
q = imag(z)./real(z);
zinmea = [z z];
yp1 = yp;
yp2 = yp;

rs = real(zs);
ls = imag(zs)./(2.*pi.*fhz);
rp = 1./real(yp);
cp = imag(yp)./(2.*pi.*fhz);

filename = strcat(dmbfileprefix,'.pip');
mdout = fopen(filename,'w');
s = sprintf('Writing pip to %s ...',filename);
disp(s);
fprintf(mdout,'Simple parallel Rp|Cp model\n');
fprintf(mdout,'# GHz Mag(Zin) Mag(Zs) Re(Zs) Im(Zs) Re(Yp) Im(Yp) Rs Ls Rp Cp
Q\n');
md = [fhz./1E+9 abs(z) abs(zs) real(zs) imag(zs) real(yp) imag(yp) rs ls rp cp q];
fprintf(mdout,'%6.4e %6.4e %6.4e %6.4e %6.4e %6.4e %6.4e %6.4e %6.4e %6.4e
%f\n',md');
fclose(mdout);

reysmea = real(ys);
reypmea = real(yp);
imysmea = imag(ys);
imypmea = imag(yp);

% Calculate simple frequency dependent model with series Rp|Cp
rs = real(zs);
ls = imag(zs)./(2.*pi.*fhz);

```

```

rp = real(zp);
cp = -1./(2.*pi.*fhz.*imag(zp));

filename = strcat(dmbfileprefix,'.pis');
mdout = fopen(filename,'w');
s = sprintf('Writing pis to %s ...',filename);
disp(s);
fprintf(mdout,'Simple serial Rp|Cp model\n');
fprintf(mdout,'# GHz Mag(Zin) Mag(Zs) Re(Zs) Im(Zs) Re(Zp) Im(Zp) Rs Ls Rp Cp Q\n');
md = [fhz./1E+9 abs(z) abs(zs) real(zs) imag(zs) real(zp) imag(zp) rs ls rp cp q];
fprintf(mdout,'%6.4e %6.4e %6.4e %6.4e %6.4e %6.4e %6.4e %6.4e %6.4e %6.4e %6.4e\n',md);
fclose(mdout);

% Interpolate frequency into equi-spacing data in log-scale
% Thanks B-G Kim for this idea.
fmea = log10(fhz);
fmeamin = min(fmea);
fmeamax = max(fmea);
fnew = fmeamin:0.01:fmeamax;
reys = interp1(fmea,reysmea,fnew);
imys = interp1(fmea,imysmea,fnew);
rey1 = interp1(fmea,reypmea,fnew);
imy1 = interp1(fmea,imypmea,fnew);
rey2 = interp1(fmea,reypmea,fnew);
imy2 = interp1(fmea,imypmea,fnew);

gs = guess;

%options=optimset('MaxFunEvals',10e9,'MaxIter',10e9,'TolFun',1e-10);
options = optimset('LargeScale','on');

lbs = [lb(7) lb(8) lb(9) lb(10) lb(11)];
ysguess = [gs(7) gs(8) gs(9) gs(10) gs(11)];
ubs = [ub(7) ub(8) ub(9) ub(10) ub(11)];

for i = 1:20;

```

```

func=@ysrefunc; % Imaginary function to be fit is ysrefunc.m
% Call lsqcurvefit for real part fitting;
[refit,eresnorm,eresidual,reexitflag,reoutput] = ...
    lsqcurvefit(func,ysguess,fnew,reys,lbs,ubs,options);

func=@ysimfunc; % Imaginary function to be fit is ysimfunc.m
% Call lsqcurvefit for imaginary part fitting;
[ysguess,imresnorm,imresidual,imexitflag,imoutput] = ...
    lsqcurvefit(func,refit,fnew,imys,lbs,ubs,options);
end % for i

% fit=[R0,lambda,beta,Cf,Leff]
s1=sprintf('\n##### Initial Ys real guess #####\n');
s2=sprintf('Lower limit [%6.3f %6.3f %6.3f %6.3f %6.3f]\n',lbs);
s3=sprintf('Guess [%6.3f %6.3f %6.3f %6.3f %6.3f]\n',ysguess);
s4=sprintf('Upper limit [%6.3f %6.3f %6.3f %6.3f %6.3f]\n',ubs);
disp(s1);disp(s2);disp(s3);disp(s4);

s1 = sprintf('\n#####\n');
s2 = sprintf('Ys real optimization output:');
s3 = sprintf('\n#####\n');
s4 = sprintf('Resnorm = %f\n',eresnorm);
s5 = sprintf('Exitflag = %f\n',reexitflag);
s6 = sprintf('Output = ');
disp(s1);disp(s2);disp(s3);disp(s4);disp(s5);disp(s6);disp(reoutput);

% fit=[R0,lambda,beta,Cf,Leff]
s1=sprintf('\n##### Initial Ys imaginary guess #####\n');
s2=sprintf('Lower limit [%6.3f %6.3f %6.3f %6.3f %6.3f]\n',lbs);
s3=sprintf('Guess [%6.3f %6.3f %6.3f %6.3f %6.3f]\n',refit);
s4=sprintf('Upper limit [%6.3f %6.3f %6.3f %6.3f %6.3f]\n',ubs);
disp(s1);disp(s2);disp(s3);disp(s4);

s1 = sprintf('\n#####\n');
s2 = sprintf('Ys imaginary optimization output:');
s3 = sprintf('\n#####\n');
s4 = sprintf('Resnorm = %f\n',imresnorm);
s5 = sprintf('Exitflag = %f\n',imexitflag);
s6 = sprintf('Output = ');

```

```

disp(s1);disp(s2);disp(s3);disp(s4);disp(s5);disp(s6);disp(imoutput);

c = ysguess;

lbp = [lb(1) lb(2) lb(3)];
ypguess = [gs(1) gs(2) gs(3)];
ubp = [ub(1) ub(2) ub(3)];

for i = 1:20;

func=@yprefunc; % Imaginary function to be fit is yprefunc.m
% Call lsqcurvefit for real part fitting;
[refit,eresnorm,eresidual,reexitflag,reoutput] = ...
    lsqcurvefit(func,ypguess,fnew,rey1,lbp,ubp,options);

func=@ypimfunc; % Imaginary function to be fit is ypimfunc.m
% Call lsqcurvefit for imaginary part fitting;
[ypguess,imresnorm,imresidual,imexitflag,imoutput] = ...
    lsqcurvefit(func,refit,fnew,imy1,lbp,ubp,options);

end % for i

% fit=[Cis1,Csub1,Rsub1]
s1=sprintf('\n##### Initial Y1 real guess #####\n');
s2=sprintf('Lower limit [%6.3f %6.3f %6.3f]\n',lbp);
s3=sprintf('Guess [%6.3f %6.3f %6.3f]\n',ypguess);
s4=sprintf('Upper limit [%6.3f %6.3f %6.3f]\n',ubp);
disp(s1);disp(s2);disp(s3);disp(s4);

s1 = sprintf('\n#####\n');
s2 = sprintf('Y1 real optimization output:');
s3 = sprintf('\n#####\n');
s4 = sprintf('Resnorm = %f\n',eresnorm);
s5 = sprintf('Exitflag = %f\n',reexitflag);
s6 = sprintf('Output = ');
disp(s1);disp(s2);disp(s3);disp(s4);disp(s5);disp(s6);disp(reoutput);

% fit=[Cis1,Csub1,Rsub1]
s1=sprintf('\n##### Initial Y1 imaginary guess #####\n');

```

```

s2=sprintf('Lower limit [%6.3f %6.3f %6.3f]\n',lbp);
s3=sprintf('Guess [%6.3f %6.3f %6.3f]\n',refit);
s4=sprintf('Upper limit [%6.3f %6.3f %6.3f]\n',ubp);
disp(s1);disp(s2);disp(s3);disp(s4);

s1 = sprintf('\n#####\n');
s2 = sprintf('Y1 imaginary optimization output:');
s3 = sprintf('\n#####\n');
s4 = sprintf('Resnorm = %f\n',imresnorm);
s5 = sprintf('Exitflag = %f\n',imexitflag);
s6 = sprintf('Output = ');
disp(s1);disp(s2);disp(s3);disp(s4);disp(s5);disp(s6);disp(imoutput);

a = ypguess;

lbp = [lb(4) lb(5) lb(6)];
ypguess = [gs(4) gs(5) gs(6)];
ubp = [ub(4) ub(5) ub(6)];

for i = 1:20;

func=@yprefunc; % Imaginary function to be fit is yprefunc.m
% Call lsqcurvefit for real part fitting;
[refit,eresnorm,eresidual,rexistflag,reoutput] = ...
    lsqcurvefit(func,ypguess,fnew,rey2,lbp,ubp,options);

func=@ypimfunc; % Imaginary function to be fit is ypimfunc.m
% Call lsqcurvefit for imaginary part fitting;
[ypguess,imresnorm,imresidual,imexitflag,imoutput] = ...
    lsqcurvefit(func,refit,fnew,imy2,lbp,ubp,options);
end % for i

% fit=[Cis2,Csub2,Rsub2]
s1=sprintf('\n##### Initial Y2 real guess #####\n');
s2=sprintf('Lower limit [%6.3f %6.3f %6.3f]\n',lbp);
s3=sprintf('Guess [%6.3f %6.3f %6.3f]\n',ypguess);
s4=sprintf('Upper limit [%6.3f %6.3f %6.3f]\n',ubp);
disp(s1);disp(s2);disp(s3);disp(s4);

```



```

s1 = sprintf('\n#####\n');
s2 = sprintf('Y2 real optimization output:');
s3 = sprintf('\n#####\n');
s4 = sprintf('Resnorm = %f\n',reresnorm);
s5 = sprintf('Exitflag = %f\n',reexitflag);
s6 = sprintf('Output = ');
disp(s1);disp(s2);disp(s3);disp(s4);disp(s5);disp(s6);disp(reoutput);

```

```

% fit=[Cp2,Csub2,Rsub2]
s1=sprintf('\n##### Initial Y2 imaginary guess #####\n');
s2=sprintf('Lower limit [%6.3f %6.3f %6.3f]\n',lbp);
s3=sprintf('Guess [%6.3f %6.3f %6.3f]\n',refit);
s4=sprintf('Upper limit [%6.3f %6.3f %6.3f]\n',ubp);
disp(s1);disp(s2);disp(s3);disp(s4);

```

```

s1 = sprintf('\n#####\n');
s2 = sprintf('Y2 imaginary optimization output:');
s3 = sprintf('\n#####\n');
s4 = sprintf('Resnorm = %f\n',imresnorm);
s5 = sprintf('Exitflag = %f\n',imexitflag);
s6 = sprintf('Output = ');
disp(s1);disp(s2);disp(s3);disp(s4);disp(s5);disp(s6);disp(imoutput);

```

```

b = ypguess;

```

```

fit = [a(1) a(2) a(3) b(1) b(2) b(3) c(1) c(2) c(3) c(4) c(5)];

```

```

% Reconstruct the equation buy plugging in the fitted parameters.
[ysfit,y1fit,y2fit,sfit,zinfit,rsfit] = compute2port(fit);

```

```

% Write modeled S-parameters to file.
s11fit = sfit(:,1);
s21fit = sfit(:,2);
s12fit = sfit(:,3);
s22fit = sfit(:,4);
filename = strcat(dmbfileprefix,'fit.s2p');
out = fopen(filename,'w');
s = ...
sprintf('Writing modeled two-port S-parameter to %s ...',filename);

```

```

disp(s);
fprintf(out,'# GHz S RI R 50\n');
dmbs2p = [fhz./1E+9 real(s11fit) imag(s11fit) real(s21fit) imag(s21fit) ...
          real(s12fit) imag(s12fit) real(s22fit) imag(s22fit)];
fprintf(out,'%f %f %f %f %f %f %f %f %f\n',dmbs2p);
fclose(out);

fit = exp(fit.*log(10));

% fit=[Cis1,Csub1,Rsub1,Cis2,Csub2,Rsub2,R0,Lambda,Beta,Cf,Ls]
s1=sprintf('\n##### Initial guess #####\n');
s2=sprintf(...
'LB[%6.3f %6.3f %6.3f %6.3f %6.3f %6.3f %6.3f %6.3f %6.3f %6.3f %6.3f]\n',lb);
s3=sprintf(...
'Guess[%6.3f %6.3f %6.3f %6.3f %6.3f %6.3f %6.3f %6.3f %6.3f %6.3f %6.3f]\n',gs);
s4=sprintf(...
'UB[%6.3f %6.3f %6.3f %6.3f %6.3f %6.3f %6.3f %6.3f %6.3f %6.3f %6.3f]\n',ub);
disp(s1);disp(s2);disp(s3);disp(s4);

% Display fitted model parameters
s1 = sprintf('\n##### Two-port inductor model #####\n');
s2 = sprintf('Cis1 = %6.4e\n',fit(1));
s3 = sprintf('Csub1 = %6.4e\n',fit(2));
s4 = sprintf('Rsub1 = %6.4e\n',fit(3));
s5 = sprintf('Cis2 = %6.4e\n',fit(4));
s6 = sprintf('Csub2 = %6.4e\n',fit(5));
s7 = sprintf('Rsub2 = %6.4e\n',fit(6));
s8 = sprintf('R0 = %6.4e\n',fit(7));
s9 = sprintf('Lambda = %6.4e\n',fit(8));
s10 = sprintf('Beta = %6.4e\n',fit(9));
s11 = sprintf('Cf = %6.4e\n',fit(10));
s12 = sprintf('Ls = %6.4e\n',fit(11));
s13 = sprintf('Rs = R0[1+Lambda*(f^Beta)] = %f[1+%f*(f^%f)]\n', ...
fit(7),fit(8),fit(9));
disp(s1);disp(s2);disp(s3);disp(s4);disp(s5);disp(s6);disp(s7);
disp(s8);disp(s9);disp(s10);disp(s11);disp(s12);disp(s13);

% Write data to output file *.mod
filename = strcat(dmbfileprefix,'.mod');

```

164

```

% #####
% # Function ysrefunc(guess,f,reys) define the function
% # to be curve fitted to extract RLC parameters of
% # two-port S-parameter of a two-port on-chip inductor.
% # Written by Nimit Chomnawang. April 17, 2002.
% #####
% ysrefunc.m

function reysfit = ysrefunc(guess,f,reys)

% Pass parameters to r0,lambda,cf and ls.
%  $\ln(\text{param}) = \ln(10^{\text{guess}}) = \text{guess} * \ln(10)$ ;  $\text{param} = \exp(\text{guess} * \ln(10))$ .
param = exp(guess.*log(10));
r0 = param(1);
lambda = param(2);
beta = param(3);
cf = param(4);
ls = param(5);

% Calculate complex Ys.
%  $R(f) = R_0[1 + \lambda * (f^{\beta})]$ 
fhz = exp(f.*log(10));
rs = r0.*(1+(lambda.*(fhz.^beta)));

omega = 2.*pi.*fhz;

% Calculate Re(Ys).
reysfit = real((1./(rs+(sqrt(-1)).*ls.*omega))) + (sqrt(-1).*cf.*omega));

return;

```

```

% #####
% # Function ysimfunc(guess,f,imys) define the function
% # to be curve fitted to extract RLC parameters of
% # two-port S-parameter of a two-port on-chip inductor.
% # Written by Nimit Chomnawang. April 17, 2002.
% #####
% ysimfunc.m

function imysfit = ysimfunc(guess,f,imys)

% Pass parameters to r0,lambda,cf and ls.
%  $\ln(\text{param}) = \ln(10^{\text{guess}}) = \text{guess} * \ln(10)$ ;  $\text{param} = \exp(\text{guess} * \ln(10))$ .
param = exp(guess.*log(10));
r0 = param(1);
lambda = param(2);
beta = param(3);
cf = param(4);
ls = param(5);

% Calculate complex Ys.
%  $R(f) = R0[1 + \lambda * (f^{\beta})]$ 
fhz = exp(f.*log(10));
rs = r0.*(1+(lambda.*(fhz.^beta)));

omega = 2.*pi.*fhz;

% Calculate Im(Ys).
imysfit = imag((1./(rs+(sqrt(-1).*ls.*omega))) + (sqrt(-1).*cf.*omega));

return;

```

```

% #####
% # Function yprefunc(guess,f,reyp) define the function
% # to be curve fitted to extract RLC parameters of
% # two-port S-parameter of a two-port on-chip inductor.
% # Written by Nimit Chomnawang. April 17, 2002.
% #####
% yprefunc.m

function reypfit = yprefunc(guess,f,reyp)

% Pass initial parameters to cp, csub and rsub.
%  $\ln(\text{param}) = \ln(10^{\text{guess}}) = \text{guess} * \ln(10)$ ;  $\text{param} = \exp(\text{guess} * \ln(10))$ .
param = exp(guess.*log(10));
cis = param(1);
csub = param(2);
rsub = param(3);

fhz = exp(f.*log(10));
omega = 2.*pi.*fhz;

% Calculate Re(Yp).
reypfit = real(1./((1./((sqrt(-1).*csub.*omega)+(1./rsub)))+(1./((sqrt(-1).*cis.*omega)))));

return;

```

```

% #####
% # Function ypimfunc(guess,f,imyp) define the function
% # to be curve fitted to extract RLC parameters of
% # two-port S-parameter of a two-port on-chip inductor.
% # Written by Nimit Chomnawang. April 17, 2002.
% #####
% ypimfunc.m

function imypfit = yprefunc(guess,f,imyp)

% Pass initial parameters to cp, csub and rsub.
%  $\ln(\text{param}) = \ln(10^{\text{guess}}) = \text{guess} * \ln(10)$ ;  $\text{param} = \exp(\text{guess} * \ln(10))$ .
param = exp(guess.*log(10));
cis = param(1);
csub = param(2);
rsub = param(3);

fhz = exp(f.*log(10));
omega = 2.*pi.*fhz;

% Calculate Im(Yp).
imypfit = imag(1./((1./((sqrt(-1).*csub.*omega)+(1./rsub)))+(1./((sqrt(-1).*cis.*omega)) ) ));

return;

```

```

% #####
% # Matlab function compute2port(fit) calculate magnitude and
% # angle of calculated two-port S-parameter from the
% # fitted coefficients parameters.
% # Written by Nimit Chomnawang. April 17, 2002.
% #####
% compute2port.m

function [ysfit,y1fit,y2fit,sfit,zinfit,rsfit] = compute2port(fit)

global fhz;

% Pass parameters to cp1,csb1,rsub1,cp2,csb2,rsub2,r0,lambda,beta,cf and ls.
%  $\ln(\text{param}) = \ln(10^{\text{fit}}) = \text{fit} \cdot \ln(10)$ ;  $\text{param} = \exp(\text{fit} \cdot \ln(10))$ .
param = exp(fit.*log(10));
cp1 = param(1);
csb1 = param(2);
rsub1 = param(3);
cp2 = param(4);
csb2 = param(5);
rsub2 = param(6);
r0 = param(7);
lambda = param(8);
beta = param(9);
cf = param(10);
leff = param(11);

% Calculate complex Ys.
%  $R(f) = R_0[1 + \lambda \cdot (f^{0.5})]$ 
rsfit = r0.*(1+(lambda.*(fhz.^beta)));

omega = 2.*pi.*fhz;

% Calculate Ys,y21 and y12.
ysfit = (1./(rsfit + (sqrt(-1).*leff.*omega))) + (sqrt(-1).*cf.*omega);
%  $Y_s = 1/B = -1/y_{21}$ ; then  $y_{21} = -Y_s = y_{12}$ 
y21 = -ysfit;
y12 = y21;

```



```

% Calculate Y1 and Y2.
y1fit = 1./((1./((1./rsub1)+(sqrt(-1).*csub1.*omega)))+(1./((sqrt(-1).*cp1.*omega))));
% Y1 = (D-1)/B; BY1+1= D =-y11/y21; y11= -y21(BY1+1)= -y21[(-Y1/y21)+1]=Y1-y21.
y11 = y1fit-y21;
y2fit = 1./((1./((1./rsub2)+(sqrt(-1).*csub2.*omega)))+(1./((sqrt(-1).*cp2.*omega))));
% Y2 = (A-1)/B; BY2+1= A =-y22/y21; y22= -y21(BY2+1)= -y21[(-Y2/y21)+1]=Y2-y21.
y22 = y2fit-y21;

% Normalize Y.
y11 = y11.*50;
y21 = y21.*50;
y12 = y12.*50;
y22 = y22.*50;

% Calculate S from y.
d = ((1+y11).*(1+y22))-(y12.*y21);
s11 = (((1-y11).*(1+y22))+(y12.*y21))./d;
s21 = (-2.*y21)./d;
s12 = (-2.*y12)./d;
s22 = (((1+y11).*(1-y22))+(y12.*y21))./d;

% Calculate input impedances.
yin1fit = y1fit+ysfit; % port 2 grounded.
zin1fit = 1./yin1fit;
yin2fit = y2fit+ysfit; % port 1 grounded.
zin2fit = 1./yin2fit;

sfit = [s11 s21 s12 s22];
zinfit = [zin1fit zin2fit];
return;

```

```

% #####
% # MATLAB function twoportplot.m plot measured and fitted
% # ys,yp,S, Zin and Q of twoe-port inductor. It saves measured
% # and fitted MAG[S] and ANG[S] to file *.s,and Q to file *.q.
% #
% # Written by Nimit Chomnawang. April 17,2002.
% #####
% twoportplot.m

function twoportplot(ysm,ysf,y1m,y1f,y2m,y2f,sm,sf,zm,zf,rs,f,dmbfileprefix,pc)

s11mea = sm(:,1);
s21mea = sm(:,2);
s12mea = sm(:,3);
s22mea = sm(:,4);
s11fit = sf(:,1);
s21fit = sf(:,2);
s12fit = sf(:,3);
s22fit = sf(:,4);
ysmea = ysm;
ysfit = ysf;
y1mea = y1m;
y1fit = y1f;
y2mea = y2m;
y2fit = y2f;
zin1mea = zm;
zin2mea = zm;
zin1fit = zf(:,1);
zin2fit = zf(:,2);
rsfit = rs;

magzin1meadb = 20.*log10(abs(zin1mea));
magzin2meadb = 20.*log10(abs(zin2mea));
magzin1fitdb = 20.*log10(abs(zin1fit));
magzin2fitdb = 20.*log10(abs(zin2fit));
angzin1meadeg = 180.*angle(zin1mea)./pi;
angzin2meadeg = 180.*angle(zin2mea)./pi;
angzin1fitdeg = 180.*angle(zin1fit)./pi;
angzin2fitdeg = 180.*angle(zin2fit)./pi;

```

```
% MAG(smea) is in dB.
mags11meadb = 20.*log10(abs(s11mea));
mags21meadb = 20.*log10(abs(s21mea));
mags12meadb = 20.*log10(abs(s12mea));
mags22meadb = 20.*log10(abs(s22mea));
mags11fitdb = 20.*log10(abs(s11fit));
mags21fitdb = 20.*log10(abs(s21fit));
mags12fitdb = 20.*log10(abs(s12fit));
mags22fitdb = 20.*log10(abs(s22fit));
```

```
% ANG(S11) is in degree.
angs11meadeg = 180.*angle(s11mea)./pi;
angs21meadeg = 180.*angle(s21mea)./pi;
angs12meadeg = 180.*angle(s12mea)./pi;
angs22meadeg = 180.*angle(s22mea)./pi;
```

```
angs11fitdeg = 180.*angle(s11fit)./pi;
angs21fitdeg = 180.*angle(s21fit)./pi;
angs12fitdeg = 180.*angle(s12fit)./pi;
angs22fitdeg = 180.*angle(s22fit)./pi;
```

```
reysmea = real(ysmea);
reysfit = real(ysfit);
rey1mea = real(y1mea);
rey1fit = real(y1fit);
rey2mea = real(y2mea);
rey2fit = real(y2fit);
imysmea = imag(ysmea);
imysfit = imag(ysfit);
imy1mea = imag(y1mea);
imy1fit = imag(y1fit);
imy2mea = imag(y2mea);
imy2fit = imag(y2fit);
```

```
q1mea = abs(imag(zin1mea)./real(zin1mea));
q1fit = abs(imag(zin1fit)./real(zin1fit));
q2mea = abs(imag(zin2mea)./real(zin2mea));
q2fit = abs(imag(zin2fit)./real(zin2fit));
```

```

% Write data to output file *.smp
A = [f mags11meadb mags11fitdb angs11meadeg angs11fitdeg ...
      mags21meadb mags21fitdb angs21meadeg angs21fitdeg ...
      mags12meadb mags12fitdb angs12meadeg angs12fitdeg ...
      mags22meadb mags22fitdb angs22meadeg angs22fitdeg ];
A = A';
filename = strcat(dmbfileprefix, '.smp');
s = fopen(filename, 'w');
fprintf(s, 'GHz Mag(S11mea) Mag(S11fit) Ang(S11mea) Ang(S11fit) ');
fprintf(s, 'Mag(S21mea) Mag(S21fit) Ang(S21mea) Ang(S21fit) ');
fprintf(s, 'Mag(S12mea) Mag(S12fit) Ang(S12mea) Ang(S12fit) ');
fprintf(s, 'Mag(S22mea) Mag(S22fit) Ang(S22mea) Ang(S22fit)\n');
fprintf(s, '%f %f %f %f %f %f %f %f %f %f %f %f %f %f %f %f %f %f\n', A);
fclose(s);

% Write data to output file *.sri
A = [f real(s11mea) imag(s11mea) real(s21mea) imag(s21mea) ...
      real(s12mea) imag(s12mea) real(s22mea) imag(s22mea) ...
      real(s11fit) imag(s11fit) real(s21fit) imag(s21fit) ...
      real(s12fit) imag(s12fit) real(s22fit) imag(s22fit) ];
A = A';
filename = strcat(dmbfileprefix, '.sri');
s = fopen(filename, 'w');
fprintf(s, 'GHz Re(S11mea) Im(S11mea) Re(S21mea) Im(S21mea) ');
fprintf(s, 'Re(S12mea) Im(S12mea) Re(S22mea) Im(S22mea) ');
fprintf(s, 'Re(S11mod) Im(S11mod) Re(S21mod) Im(S21mod) ');
fprintf(s, 'Re(S12mod) Im(S12mod) Re(S22mod) Im(S22mod)\n');
fprintf(s, '%f %f %f %f %f %f %f %f %f %f %f %f %f %f %f %f %f %f\n', A);
fclose(s);

% Write data to output file *.q
A = [f q1mea q2mea q1fit q2fit];
A = A';
filename = strcat(dmbfileprefix, '.q');
q = fopen(filename, 'w');
fprintf(q, 'GHz Measured Q Modeled Q\n');
fprintf(q, '%f %f %f %f %f\n', A);
fclose(q);

```

```

% Write data to output file *.zin
A = [f magzin1meadb magzin1fitdb angzin1meadeg angzin1fitdeg ...
      magzin2meadb magzin2fitdb angzin2meadeg angzin2fitdeg ];
A = A';
filename = strcat(dmbfileprefix,'.smp');
s = fopen(filename,'w');
fprintf(s,'GHz Mag(Zin1mea) Mag(Zin1fit) Ang(Zin1mea) Ang(Zin1fit) ');
fprintf(s,'Mag(Zin2mea) Mag(Zin2fit) Ang(Zin2mea) Ang(Zin2fit)\n');
fprintf(s,'%f %f %f %f %f %f %f %f\n',A);
fclose(s);

% Plot Ys.
figname='Re(Ys)';
% Set chart size
scrsz = get(0,'ScreenSize');
figure(5);
set(5,'name',figname,'Position', ...
      [100 100 scrsz(3)*pc/100 scrsz(4)*pc/100],'color',[1 1 1]);
semilogx(f,reysmea,'ro',f,reysfit,'b-','LineWidth',2);
xlabel('Frequency (GHz)','FontWeight','b');
legend('Measured','Modeled');
ylabel('Re[Ys] (S)','FontWeight','b');
grid;

figname='Im(Ys)';
% Set chart size
scrsz = get(0,'ScreenSize');
figure(6);
set(6,'name',figname,'Position', ...
      [100 100 scrsz(3)*pc/100 scrsz(4)*pc/100],'color',[1 1 1]);
semilogx(f,imysmea,'ro',f,imysfit,'b-','LineWidth',2);
xlabel('Frequency (GHz)','FontWeight','b');
legend('Measured','Modeled');
ylabel('Im[Ys] (S)','FontWeight','b');
grid;

% Plot Y1.
figname='Re(Y1)';
% Set chart size

```

```

scrsz = get(0,'ScreenSize');
figure(7);
set(7,'name',figname,'Position', ...
    [100 100 scrsz(3)*pc/100 scrsz(4)*pc/100],'color',[1 1 1]);
semilogx(f,rey1mea,'ro',f,rey1fit,'b-','LineWidth',2);
xlabel('Frequency (GHz)','FontWeight','b');
legend('Measured','Modeled');
ylabel('Re[Y1] (S)','FontWeight','b');
grid;

```

```

figname='Im(Y1)';
% Set chart size
scrsz = get(0,'ScreenSize');
figure(8);
set(8,'name',figname,'Position', ...
    [100 100 scrsz(3)*pc/100 scrsz(4)*pc/100],'color',[1 1 1]);
semilogx(f,imy1mea,'ro',f,imy1fit,'b-','LineWidth',2);
xlabel('Frequency (GHz)','FontWeight','b');
legend('Measured','Modeled');
ylabel('Im[Y1] (S)','FontWeight','b');
grid;

```

```

% Plot Y2.
figname='Re(Y2)';
% Set chart size
scrsz = get(0,'ScreenSize');
figure(9);
set(9,'name',figname,'Position', ...
    [100 100 scrsz(3)*pc/100 scrsz(4)*pc/100],'color',[1 1 1]);
semilogx(f,rey2mea,'ro',f,rey2fit,'b-','LineWidth',2);
xlabel('Frequency (GHz)','FontWeight','b');
legend('Measured','Modeled');
ylabel('Re[Y2] (S)','FontWeight','b');
grid;

```

```

figname='Im(Y2)';
% Set chart size
scrsz = get(0,'ScreenSize');
figure(10);

```

```

set(10,'name',figname,'Position', ...
    [100 100 scrsz(3)*pc/100 scrsz(4)*pc/100], 'color',[1 1 1]);
semilogx(f,imy2mea,'ro',f,imy2fit,'b-','LineWidth',2);
xlabel('Frequency (GHz)','FontWeight','b');
legend('Measured','Modeled');
ylabel('Im[Y2] (S)','FontWeight','b');
grid;

% Plot S-parameters.
figname='MAG(S11)';
% Set chart size
scrsz = get(0,'ScreenSize');
figure(11);
set(11,'name',figname,'Position', ...
    [100 100 scrsz(3)*pc/100 scrsz(4)*pc/100], 'color',[1 1 1]);
semilogx(f,mags11meadb,'ro',f,mags11fitdb,'b-','LineWidth',2);
xlabel('Frequency (GHz)','FontWeight','b');
legend('Measured','Modeled');
ylabel('MAG[S11] (dB)','FontWeight','b');
grid;

figname='ANG(S11)';
% Set chart size
scrsz = get(0,'ScreenSize');
figure(12);
set(12,'name',figname,'Position', ...
    [100 100 scrsz(3)*pc/100 scrsz(4)*pc/100], 'color',[1 1 1]);
semilogx(f,angs11meadeg,'ro',f,angs11fitdeg,'b-','LineWidth',2);
xlabel('Frequency (GHz)','FontWeight','b');
legend('Measured','Modeled');
ylabel('ANG[S11] (degree)','FontWeight','b');
grid;

figname='MAG(S21)';
% Set chart size
scrsz = get(0,'ScreenSize');
figure(13);
set(13,'name',figname,'Position', ...
    [100 100 scrsz(3)*pc/100 scrsz(4)*pc/100], 'color',[1 1 1]);

```

```

semilogx(f,mags21meadb,'ro',f,mags21fitdb,'b-','LineWidth',2);
xlabel('Frequency (GHz)','FontWeight','b');
legend('Measured','Modeled');
ylabel('MAG[S21] (dB)','FontWeight','b');
grid;

figname='ANG(S21)';
% Set chart size
scrsz = get(0,'ScreenSize');
figure(14);
set(14,'name',figname,'Position', ...
    [100 100 scrsz(3)*pc/100 scrsz(4)*pc/100],'color',[1 1 1]);
semilogx(f,angs21meadeg,'ro',f,angs21fitdeg,'b-','LineWidth',2);
xlabel('Frequency (GHz)','FontWeight','b');
legend('Measured','Modeled');
ylabel('ANG[S21] (degree)','FontWeight','b');
grid;

figname='MAG(S12)';
% Set chart size
scrsz = get(0,'ScreenSize');
figure(15);
set(15,'name',figname,'Position', ...
    [100 100 scrsz(3)*pc/100 scrsz(4)*pc/100],'color',[1 1 1]);
semilogx(f,mags12meadb,'ro',f,mags12fitdb,'b-','LineWidth',2);
xlabel('Frequency (GHz)','FontWeight','b');
legend('Measured','Modeled');
ylabel('MAG[S12] (dB)','FontWeight','b');
grid;

figname='ANG(S12)';
% Set chart size
scrsz = get(0,'ScreenSize');
figure(16);
set(16,'name',figname,'Position', ...
    [100 100 scrsz(3)*pc/100 scrsz(4)*pc/100],'color',[1 1 1]);
semilogx(f,angs12meadeg,'ro',f,angs12fitdeg,'b-','LineWidth',2);
xlabel('Frequency (GHz)','FontWeight','b');
legend('Measured','Modeled');

```



```

ylabel('ANG[S12] (degree)','FontWeight','b');
grid;

figname='MAG(S22)';
% Set chart size
scrsz = get(0,'ScreenSize');
figure(17);
set(17,'name',figname,'Position', ...
    [100 100 scrsz(3)*pc/100 scrsz(4)*pc/100],'color',[1 1 1]);
semilogx(f,mags22meadb,'ro',f,mags22fitdb,'b-','LineWidth',2);
xlabel('Frequency (GHz)','FontWeight','b');
legend('Measured','Modeled');
ylabel('MAG[S22] (dB)','FontWeight','b');
grid;

figname='ANG(S22)';
% Set chart size
scrsz = get(0,'ScreenSize');
figure(18);
set(18,'name',figname,'Position', ...
    [100 100 scrsz(3)*pc/100 scrsz(4)*pc/100],'color',[1 1 1]);
semilogx(f,angs22meadeg,'ro',f,angs22fitdeg,'b-','LineWidth',2);
xlabel('Frequency (GHz)','FontWeight','b');
legend('Measured','Modeled');
ylabel('ANG[S22] (degree)','FontWeight','b');
grid;

% Plot Q1.
figname='Q1 port 2 grounded';
% Set chart size
scrsz = get(0,'ScreenSize');
figure(19);
set(19,'name',figname,'Position', ...
    [100 100 scrsz(3)*pc/100 scrsz(4)*pc/100],'color',[1 1 1]);
semilogx(f,q1mea,'ro',f,q1fit,'b-','LineWidth',2);
xlabel('Frequency (GHz)','FontWeight','b');
ylabel('Q-Factor','FontWeight','b');
legend('Measured','Modeled');
grid;

```

```

% Plot Q2.
figname ='Q2 port 1 grounded';
% Set chart size
scrsz = get(0,'ScreenSize');
figure(20);
set(20,'name',figname,'Position', ...
    [100 100 scrsz(3)*pc/100 scrsz(4)*pc/100],'color',[1 1 1]);
semilogx(f,q2mea,'ro',f,q2fit,'b-','LineWidth',2);
xlabel('Frequency (GHz)','FontWeight','b');
ylabel('Q-Factor','FontWeight','b');
legend('Measured','Modeled');
grid;

% Plot series resistance.
figname ='Rs';
% Set chart size
scrsz = get(0,'ScreenSize');
figure(21);
set(21,'name',figname,'Position', ...
    [100 100 scrsz(3)*pc/100 scrsz(4)*pc/100],'color',[1 1 1]);
semilogx(f,rsfit,'b-','LineWidth',2);
xlabel('Frequency (GHz)','FontWeight','b');
ylabel('R_S (\Omega)','FontWeight','b');
legend('Modeled R_S');
grid;

return;

```

```

% Initial model parameters file twoportconfig.m used by indmodel.m
% First line is lower limit parameter values. Second line is guess of
% parameters. Third line is upper limit parameter values. The unit of
% parameters are as shown below:
% [1=Cis1:F,2=Csub1:F,3=Rsub1:Ohm,4=Cis2:F,5=Csub2:F,6=Rsub2:Ohm,
% 7=R0:Ohm,8=Lambda,9=Beta,10=Cf:F,11=Ls:H]
% where Lambda,Beta are constants. The number are exponential of 10. :2==>10^2
% [ -15 -17 1 -16 -17 1 -4 -4 -1 -28 -11 ] % Lower limit.
% [ -14 -14 1 -14 -14 1 -3 -2 0 -20 -9 ] % Guess values
% [ -10 -12 3 -10 -12 3 -1 -1 1 -15 -8 ] % Upper limit.
% Nimit Chomnawang April 17, 2002.
% Do not delete anything from this line above!
[ -15 -17 1 -16 -17 1 -4 -4 -1 -28 -11 ]
[ -14 -14 1 -14 -14 1 -3 -2 0 -20 -9 ]
[ -10 -12 3 -10 -12 3 -1 -1 1 -15 -8 ]

```

## VITA

Nimit Chomnawang was born on December 29, 1971, in Khon Kaen, Thailand, and is a Thai citizen. He received his bachelor degree in Instrumentation Engineering from the King Mongkut's Institute of Technology Ladkrabang (KMITL), Bangkok, Thailand, in 1993. With financial support from the Foundation for Computer Education of Thailand, he subsequently attended graduate program in Electronics Engineering at the same institution. In 1996, he received a scholarship from the government of Thailand to study in the United States. He attended graduate program at the Virginia Commonwealth University in Richmond, Virginia, and received a Master of Science degree in biomedical engineering in 1999. He then joined the Electrical Engineering Graduate Program at the Department of Electrical and Computer Engineering, Louisiana State University. He received a Master of Science degree in electrical engineering in 2001. He is currently a candidate for the degree of Doctor of Philosophy, which will be conferred at the Fall 2002 commencement. After his graduation, he will join the School of Electrical Engineering, Suranaree University of Technology, in Thailand as an instructor.